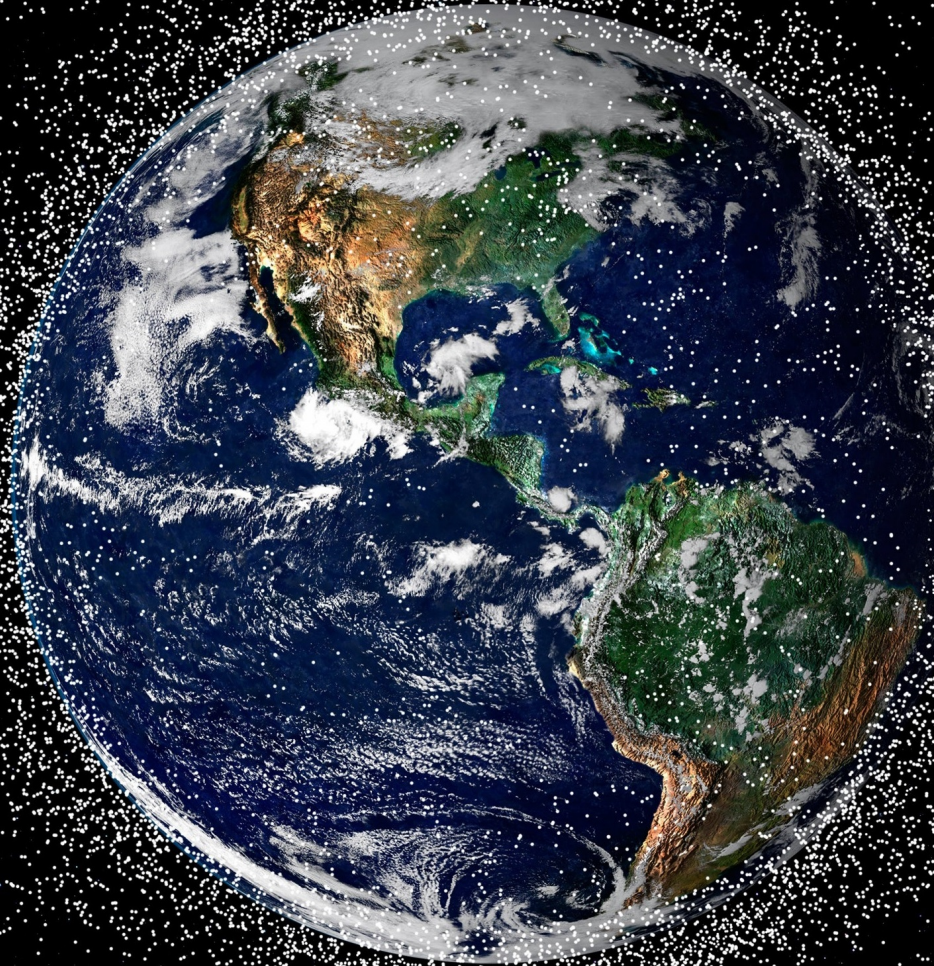


Orbit determination of small space debris in the Geostationary ring

Master Thesis

Jasper Vrijenhoek

Delft University of Technology



Orbit determination of small space debris in the Geostationary ring

by

Jasper Vrijenhoek

Student Number: 4656318
Supervisor: Dr.ir. E. Mooij
Institution: Delft University of Technology
Place: Faculty of Aerospace Engineering, Delft
Project Duration: April , 2022 - January, 2023

Cover Image: Space Debris orbiting the Earth (GETTY IMAGES)

Preface

With this document, I present the research I have done to obtain the degree of Master of Science in Aerospace Engineering. The work that I have done for the better part of this year could not have been achieved without the help of others, whom I like to thank.

First of all, I would like to thank my supervisor Dr. ir. Erwin Mooij. Through his guidance and questions during our weekly meetings, if I did not oversleep or miss the train, he made me think more critical about my research and made me a better engineer. Additionally, his friendliness and sense of humour made it very enjoyable to work with him.

Finally, as my time as a student now comes to an end, I would like to thank my friends, family and roommate who made this time so much more enjoyable.

*Jasper Vrijenhoek
Delft, January 2023*

Summary

Since the start of space flight the amount of space debris orbiting the Earth has steadily increased. Because these space debris objects have a very high velocity even very small pieces, 1 cm, could cause the total failure of an operational satellite. To minimise the chance of this happening and to ensure that space flight will be possible in the future, it is necessary to be able to avoid and one day hopefully remove these space debris objects. To do this, it is important to have an accurate estimation of the orbits of these objects. Due to the non-cooperative nature and small size of space debris, precise orbit determination is difficult to achieve. This is especially the case for smaller space debris objects in GEO, at the moment there is no method which can be used to detect and therefore perform orbit determinations for these objects. One possible solution is by using space based optical sensors, this research aims to answer the following question: *"To what extent can a constellation of satellites with optical sensors increase the surveillance of 1 to 10 cm sized space debris in GEO?"*

To answer this question a simulator was created which simulated optical observations of space debris objects made by satellites and used these observations to determine the orbit of those objects. Using this simulator a constellation design was optimised using five different design variables, the semi-major axis, the number of satellites per group, the total number of satellites in the constellation, the focal length and finally the inclination difference between satellites in a group. These design variables were optimised for two different performance metrics, the accuracy of the orbit determination and the number of successful orbit determinations, while also taking into account the mission cost. The performance of the resulting optimal design was evaluated to answer the main research question.

The average position accuracy of the orbit determinations for the optimal design was 198 meters. This accuracy is high enough for the system to maintain custody and thus provide regular estimated orbit updates for objects that can be frequently observed. The optimal design is able to provide successful orbit determinations for only 17% of all space debris objects, if only one group of 3 satellites is used. This percentage can be increased significantly by using more satellite groups, but even when using as much as 30 total satellites, the system is still only able to provide orbit determinations for 35% of all space debris objects. This poor performance is mainly caused by objects smaller than 4 centimeter and objects with high inclinations.

It was found that the system is capable of providing regular accurate orbit estimations and maintaining custody for newer space debris objects with a size larger than 4 centimetres using only a limited amount of satellites and perhaps even slightly older objects if the satellite position and measurement errors can be reduced. The system will also be able to sporadically observe and provide an accurate orbit estimation for older space debris objects with a higher inclination. However, the system will not be capable of doing so regularly even when using a large number of satellites, thus making maintaining custody very difficult for these objects. At this moment no orbit determinations can be done for objects in the GEO region smaller than 10 centimetres, they can not even be observed. A system such as this can thus increase the space situational awareness for the GEO region significantly. Space debris objects smaller than 2 centimetres are still not detectable by this kind of system, unless a very non-optimal constellation design is used.

Nomenclature

Abbreviations

Abbreviation	Definition
CCD	Charged Couple device
ECI	Earth centered inertial frame
EKF	Extended Kalman filter
ESA	European space agency
FOV	Field of view
GEO	Geostationary orbit
GSSAP	Geosynchronous Space Situational Awareness Program
GTO	Geostationary transfer orbit
IOD	Initial orbit determination
LEO	Low Earth orbit
MEO	Medium Earth orbit
NASA	National Aeronautics and Space Administration
OD	Orbit determination
RK4	Runge-Kutta 4
RSW	Radian, along-track and cross-track
SBSS	Space Bases Space Surveillance
SNR	Signal to noise ratio
TLE	Two line element
UKF	Unscented Kalman filter

Symbols

Symbol	Definition	Unit
A	area	[m ²]
a	acceleration	[m/s ²]
a	semi-major axis	[m]
d	diameter	[m]
d	distance	[m]
E	eccentric anomaly	[rad]
e	eccentricity	[m]
G	gravitational constant	[m ³ / kg s ²]
g	versor	[-]
h	height	[m]
i	inclination	[rad]
J	Cost value	[-]
M	mean anomaly	[rad]
M	mass	[kg]
m	visual magnitude	[-]
m	order of spherical harmonic gravity field	[-]
n	degree of spherical harmonic gravity field	[-]
n	mean orbital angular velocity	[rad/s ²]
n	line of sight unit vector	[-]
P	solar radiation pressure	[N/m ²]

Symbol	Definition	Unit
P	Covariance matrix	[-]
\mathbf{p}	Relative position vector	[-]
R	radius	[m]
R	Measurement covariance matrix	[-]
\mathbf{r}	position vector	[m]
U	gravitational potential energy	[J]
Q	Process noise matrix	[-]
QE	Quantum efficiency	[-]
w	width	[m]
\mathbf{x}	state vector	[-]
ϵ	error	[-]
Θ	true anomaly	[rad]
Θ	FOV angle	[rad]
Θ	geographic longitude	[rad]
μ	gravitational parameter	[m ³ /s ²]
ρ	range	[m]
ρ	albedo	[-]
σ	noise	[-]
τ	optical transmittance	[-]
ϕ	geocentric latitude	[rad]
ϕ	solar phase angle	[rad]
Ω	longitude of the ascending node	[rad]
ω	argument of periapsis	[rad]
ω	perigee longitude	[rad]

Contents

Preface	ii
Summary	iv
Nomenclature	vi
1 Introduction	1
1.1 Heritage	1
1.1.1 Ground-based orbit estimation	2
1.1.2 Space-based orbit determination	2
1.2 Research questions	3
2 Optical observations	5
2.1 Observation	5
2.2 Error	6
2.3 Signal to Noise ratio	8
3 Orbit propagation	11
3.1 Space debris objects vs satellites	11
3.2 Reference frames	12
3.2.1 Earth centered inertial reference frame	13
3.2.2 Body Fixed frame	13
3.2.3 Local Vertical Local Horizon	13
3.3 Transformations	13
3.4 State variables	14
3.4.1 Cartesian coordinates	14
3.4.2 Kepler elements	14
3.4.3 Modified Equinoctial Elements	15
3.5 Force and environment models	16
3.5.1 Point mass gravity	16
3.5.2 Earth's gravitational model	16
3.5.3 Third body perturbation	17
3.5.4 Solar radiation pressure	17
3.5.5 Ephemerides model	17
3.6 Equations of motion	17
3.6.1 Modified equinoctial elements	17
3.6.2 Kepler orbit	18
4 Estimation methods	19
4.1 Simplex Fusion	19
4.2 Unscented Kalman filter	22
5 Numerical methods	25
5.1 Integrator	25
5.2 Pseudo Random number generator	25
5.3 Simplex Nelder-Mead optimisation	26
6 Software	29
6.1 External Software	29
6.1.1 Tudat	29
6.1.2 NumPy and SciPy	29
6.2 Architectural Design	30
6.2.1 Initial state	31

6.2.2	Orbital Propagation	31
6.2.3	Observation	31
6.2.4	Orbit Determination	33
6.3	Verification and validation	34
6.3.1	Initial state	34
6.3.2	Orbit propagation	35
6.3.3	Observations	35
6.3.4	Orbit determination	36
7	Design space	43
7.1	Design variables	43
7.2	Design space exploration	46
7.3	UKF tuning	49
8	Design optimisation & analysis	51
8.1	Taguchi method	51
8.1.1	S/N results	52
8.1.2	Successful orbit determinations	53
8.1.3	Average position accuracy	57
8.2	Limited factorial design	59
8.3	Optimal design performance	64
8.3.1	Number of total satellites	66
8.3.2	Maintain custody	68
8.4	Sensitivity	70
8.4.1	Design sensitivity	70
8.4.2	Performance sensitivity	72
8.5	Robustness	74
8.5.1	Space debris near GPS-satellites	75
8.5.2	Geostationary transfer orbit	75
9	Conclusions & Recommendations	77
9.1	Conclusions	77
9.2	Recommendations	79
	References	81
A	Heritage tables	85
B	Taguchi table	87

1

Introduction

Many critical systems that play a large part in the world's economy and governments are heavily reliant on the continuous operation of satellites. This dependency is expected to only increase in the following decades. One of the major threats to the operation and safety of current and future space based systems is space debris. Space debris is "any human-made object in orbit about the Earth that no longer serves a useful function. Such debris includes nonfunctional spacecraft, abandoned launch vehicle stages, mission-related debris, and fragmentation debris" according to the definition of NASA. It has been estimated that there have been more than 640 break-up events¹, which have increased the number of space debris objects in space. The largest break-up event was the anti-satellite test performed by China in 2007 which added approximately 3500 new space debris objects (Johnson, 2010), however, with every new space mission more space debris is added. Due to the high velocities at which these space debris objects travel, the consequences of a collision between an operational satellite and a piece of space debris can be massive. A collision with an object as small as 1 cm can lead to the complete failure of a mission (Chen, 2011). The estimated number of space debris objects larger than 1 cm is around one million¹ and is expected to keep growing.

There are two ways to deal with the problems occurring due to the ever increasing amount of space debris, either a space mission needs to perform a manoeuvre to avoid a collision or the space debris objects need to be removed from space or put into a non harmful orbit. For both these methods, an approximate orbit of the space debris objects needs to be known. For satellites this is most commonly done by using radar measurements from ground-stations to the satellites. By determining the travel time of the radar signal between the satellite and the ground-station, the pseudorange can be determined, this pseudorange is then used in either batch or sequential estimation methods in order to determine the orbit of the satellite. Other methods to obtain the pseudorange that are commonly used for orbit determination are laser ranging and Doppler measurements (Schutz et al., 2004). These methods are also used for the orbit determination of space debris objects. However, the orbit determination of space debris comes with extra challenges. Space debris is so called non-cooperative, these objects do not have (operational) receivers, antenna's or reflectors which can be used to accurately determine the orbit. Additionally, most of these objects are very small and it is thus harder to detect and track them. Due to these extra challenges optical methods are also commonly used for the orbit determination of space debris objects. Ground-based telescopes make angular measurements of the position of the object, using these measurements, so-called angles-only orbit determination methods are used to estimate the orbit of the space debris objects (Fadrique et al., 2012).

1.1. Heritage

In the first 30 years of space flight no efforts were made to detect and determine the orbit of space debris. In the 1980's, as the number of possibly harmful objects and the possibility of catastrophic collisions increased, space agencies and other experts in the field started to recognise the need for orbit determination of space debris and multiple offices were set up for this purpose (ESA, 2017a)

¹ https://www.esa.int/Safety_Security/Space_Debris/Space_debris_by_the_numbers: date accessed:12/1/2023

(Reynolds and Potter, 1989). Two different orbit determination methods can be identified, ground-based and space based.

1.1.1. Ground-based orbit estimation

The past and current ground-based methods for the orbit determination of space debris can also be split up into two different methods, optical orbit determination and orbit determination based on radar measurements. In Appendix A two tables can be found where the main systems for both optical and radar based orbit determination are described.

Currently ground-based optical orbit determination methods are being used for the detection of relatively large space debris objects for all altitudes from Low Earth Orbits (LEO) to Geostationary Orbits (GEO) (Silha, 2020). At LEO the optical ground-based systems are able to detect objects as small as 1 cm (NASA, 2007), while at GEO the minimum size is 10 cm (Garcia-Talavera et al., 2002). There is also a clear motion toward using satellite laser ranging which provides superior orbit determination accuracy and increases the operational window of the systems (Zhang et al., 2012)(Kirchner et al., 2013)(Lejba et al., 2018)(Steindorfer et al., 2020).

Radar based methods are currently only being used for the orbit determination of space debris located in the 400-2500 km altitude range. Compared to the ground-based optical methods it can detect far smaller objects, space debris as small as 3 mm can be detected (Czerwinski M.G., 2014). There are also two different antenna types being used, a dish antenna and a phased array. The majority of the older systems uses a single large parabolic antenna. But the newer and proposed systems are mostly by-static and phased arrays, which give improved performance compared to the older systems (Muntoni et al., 2021) (Saillant, 2016) (Baskakov et al., 2017). However, even these newer radar systems will not be able to detect space debris in GEO and beyond.

1.1.2. Space-based orbit determination

As can be concluded from the previous section, ground-based methods can only detect particles >4 mm in LEO and around 10 cm in GEO, space-based methods can detect particles that are a lot smaller. There are two different methods one could employ to determine the orbits of space debris in space, impact sampling and remote sensing. Impact sampling can be done either passively or actively, passively by bringing exposed surfaces of satellites back to Earth and analysing the impacts of space debris on these surfaces (Clark et al., 1984). Active sampling can be done by using different sensors (optical/radar) (Committee on Space Debris, 1995). At this point only two missions using space-based active sampling have been flown, while numerous impact sampling missions have taken place. Firstly, the impact sampling missions will be discussed.

The first instance of impact sampling was done by looking at the returned exposed surfaces of manned mission to space, like the Apollo, Mercury, Space Shuttle, Hubble space telescope missions, where the windows or other exposed surfaces of these spacecraft were inspected and analysed for impact of small debris (Reynolds and Potter, 1989)(Committee on Space Debris, 1995). Impact sampling could thus be seen as the first instance of orbit determination of space debris. However, there are some severe limitations on the orbit determination capabilities of the impact sampling technique. First of all, it can only detect space debris that directly hit the exposed surfaces, thus there is a big change that the impact sampling gives a wrong estimation of the number and size of particles that actually orbit in that particular altitude regime. Secondly, it is very difficult to determine the orbital parameters of the space debris by just looking at the impacts (Committee on Space Debris, 1995). However, the added benefit of impact sampling is the fact that it is able to detect sub-millimetre sized particles, something that ground-based methods are not able to do yet. As mentioned before, almost all spacecraft that are returned to Earth are analysed for the impact of space debris. There have also been missions/instruments that had as primary or secondary mission to determine the space debris flux in certain altitude regions, like the Debris in-Orbit Evaluator (Kuitunen et al., 2001), Long Duration Exposure Facility (1984)(Clark et al., 1984), Geostationary Orbit Impact Detector (1996)(Drolshagen et al., 1999). These were all able to provide very rough orbit determinations of the space debris objects that hit the sensors.

As mentioned before, there have only been two mission that had as main mission the remote sensing of space debris, the Space Based Space Surveillance (SBSS) and the Canadian Space Surveillance System; Sapphire. The SBSS is a constellation of satellites that will perform OD for both LEO and GEO based space debris using optical sensors. At this moment the SBSS consists of only five

satellites. The first satellite, SBSS-1, was launched in 2010 and consisted of a 30 cm telescope which flew in a Sun-synchronous orbit at an altitude of 630 km (ESA, 2017b). The other four satellites are all Geosynchronous Space Situational Awareness Program (GSSAP) satellites, which all fly in GEO and are also used for OD of space debris in GEO, the first pair were launched in 2014 and the second pair in 2016, a third pair is scheduled to be launched in 2021 (ESA, 2019). The Sapphire mission is a single satellite orbiting at an altitude of 750 km and was launched in 2013. It also uses an optical telescope to detect space debris between 6,000 and 40,000 km altitude (Maskell and Oram, 2008). There have been multiple studies into the use of a constellation of satellites equipped with optical sensors for the use of orbit determination of space debris in LEO, which showed promising results (Du et al., 2019) (Felicetti and Emami, 2016). Additionally, there have been some studies that looked at the use of a space based radar system, however, the power requirements and dish size would severely limit any mission design (Carl et al., 1993).

1.2. Research questions

As could be read in the previous subsections the orbit determination of space debris is already being done for all the meaningful orbits (LEO-MEO-GEO). However, there is a difference in the amount and size of space debris that have been tracked and catalogued between the three orbit regimes. In LEO both radar and optical, either passive or active, are being used to detect objects down to 10 mm. While for MEO and GEO most of the orbit determination is done using optical methods either ground-based or space-based, and the minimum detection size is around 10 cm for the current systems. As mentioned in the introduction, space debris down to a size of 1 cm can cause significant harm to spacecraft. These objects in LEO are already being detected and using improved radar techniques, active optical systems and space-based optical systems, the accuracy of orbit determination for these objects should, in the near future be enough to ensure the safe operation of satellites and perhaps removal of space debris. The space debris of size <10 cm in GEO can, however, still cause harm to satellites. These objects can not be observed by any ground-based system, radar or optical, and a space-based radar system would result in a non-feasible design. Additionally, it has been shown that a constellation of satellites using optical telescopes can be used for the orbit determination of space debris in LEO. The main research question for this thesis is therefore:

1. To what extent can a constellation of satellites with optical sensors increase the surveillance of 1 to 10 cm sized space debris in GEO?

To help answer this research question a couple of sub-questions can be formulated that will help in answering the main research question. The first sub-question reads as follows:

- 1.1 *How does the accuracy of the orbit determination compare, when only one satellite observes a satellite versus when multiple satellites observe the same object?*

Having multiple satellites observing the same object can increase the accuracy of the OD for this object. However, the cost of such a system would also increase, the increase in accuracy thus should be substantial. Can a single observing satellite achieve a high enough accuracy to fully fill the requirements, or are multiple observers a must?

- 1.2 *How does the constellation design change the performance of the system?*

The orbit of the observing satellite will have a major effect on the observations that can be done and the coverage of the space debris population. If the observing satellite is closer to the space debris objects the aperture size and thus satellite size can be smaller, the time it takes for the space debris to cross the field of view of the satellite will be longer, as the relative velocity is lower, thus making it possible to make more observations. However, having an observing satellite farther away increases the section of the GEO that the sensor can see thus making it possible to observe more objects at the same time. The larger relative velocity will also mean that the observing satellite will be able to cover the whole orbit in a shorter amount of time, thus increasing the time in which the orbit estimations can be updated. Additionally, the inclination and number of total satellites will also effect both the number of observations that can be performed and the accuracy of the orbit determinations.

- 1.3 *How does the orbit and size of the space debris objects effect the performance of the system?*

The orbit and size of the space debris objects will effect the number of observations the system can make of a particular object, which will in turn effect the accuracy of the orbit determinations. For example, the eccentricity and inclination will determine the maximum time that an object can be observed. Knowing the relative performance of the system for the different orbits and sizes of the space debris objects will help answer the main research question.

To answer these questions, first the constellation design needs to be optimised. There are two main performance metrics for this optimisation, the number of successful orbit determinations and the accuracy of the orbit determination. To determine the value of these performance metrics for a single constellation design the following methodology has been used. Firstly, the orbits of both the observing satellites and space debris objects will be simulated. The orbital elements of the satellites are design variables and will be optimised. The orbits of the space debris objects are based on statistical data to give a realistic performance of the different constellation designs. An optical sensor is modelled to simulate real-life observations. This model takes into account the position and relative velocity of the satellites and space debris objects, the background signals and errors. The design for the optical sensor parameters is also part of the optimisation. The resulting measurements are then used to first get an initial orbit determination, using a simplex fusion method. If this initial orbit determination is sufficiently accurate, this initial orbit determination will be used as an initial guess for the unscented Kalman filter. The resulting accuracies and the number of successful orbit determination are then used to find the optimal constellation design. A design space exploration will then be performed to determine the lower and upper bounds for the optimisation. The Taguchi method will first be used for a preliminary optimisation. After which a factorial optimisation will be done to find the optimal constellation design. The performance of the optimal design will then be analysed to answer the main and sub-research questions.

The report is structured in the following way, in Chapter 2 the optical observations will be discussed. In Chapter 3 the methods used for the propagation of the orbits are discussed. This is followed by a discussion of the estimation methods used for the orbit determination in Chapter 4. The used numerical methods are described in Chapter 5. In Chapter 6 the used software can be found. Chapter 7 describes the design space explorations. The design optimisation and subsequent analysis are discussed in Chapter 8. Finally, in Chapter 9 the conclusions and recomendations can be found.

2

Optical observations

To determine the orbit of the space debris objects, all satellites in the constellation will have a optical sensor to make measurements. These are called angles-only measurements as they only provide the direction from the observer to the object and not the range between the two. An optical sensor works by detecting the photons that hit the sensor, usually a charged-coupled device. A space debris object can be detected if the ratio between the signal photons (the photons that are reflected by the object) and the noise photons, the signal to noise ratio (SNR), detected by a optical sensor is higher than a certain threshold. In this chapter an overview will be given on how these observations will be simulated. In Section 2.1 the method to determine if a space debris object lies in the field of view of the satellite is discussed. Section 2.2 describes the errors which effect the measurement and finally in Section 2.3 the method to determine the signal to noise ratio is discussed.

2.1. Observation

The performance of different types of constellations will be analysed. Two different types of constellations will be looked at. The first type is a constellation where all satellites are relatively far away from each other and a single space debris object can only be observed by one satellite at the same time. The second type is a constellation where two or more satellites orbit close to each other and look in the same direction. This type of constellation makes it possible for a space debris object to be observed by multiple satellites at the same time. The main advantage of the first constellation type, is that it can observe more unique space debris objects with the same number of satellites as the second type. This will lead to more observations and a higher frequency of observations per unique space debris object. The second type of constellation, however, will provide more accurate orbit determination per space debris object, due to the multiple observations per time step.

To determine if the optical sensor can observe a space debris object, it must lie in the field of view (FOV) of the sensor. To determine this, a line of sight vector is projected from the location of the observing satellite to infinity, a pyramid shape centered around this line of sight is then created, the angle between the vertices and the line of sight vector is determined by the FOV angle. The direction of the line of sight vector is dependent on the type of constellation the observing satellite is in. For the first type, all satellites are far away from each other, the direction of the line of sight vector is the same as the radial direction of the observing satellite in the RSW reference system. For the second constellation type, multiple satellites orbiting close to each other, the direction for the line of sight vector for each satellite is determined in the following way. The average inclination and true anomaly for all satellites in the same group are determined at each time step. The Cartesian position of a target point is determined, using the average true anomaly and inclination and a semi-major axis at the centre of the GEO region ($a = 42,163$ km). The direction of the line of sight vector for each satellite in the group is then calculated by taking the direction vector between the position of the satellite and the target point. This makes sure that the FOVs for each satellite in the group overlap as much as possible at the point where most space debris objects are expected, this will lead to more simultaneous observations.

To check if the space debris object lies in the FOV of the optical sensor, the following method is

used. To speed up the simulation, it is first checked if the object lies in front of the observing satellite:

$$\mathbf{p} \cdot \hat{\mathbf{n}} > d \quad (2.1)$$

where \mathbf{p} is the relative position vector from the observing satellite to the space debris object, $\hat{\mathbf{n}}$ is the line of sight unit vector, d is the distance from the optical sensor to the projection plane. Then, the relative vector from the origin of the projection plane, to where the vector \mathbf{p} intersects the projection plane, is calculated as follows:

$$\mathbf{p}' = \frac{d\mathbf{p}}{\hat{\mathbf{n}} \cdot \mathbf{p}} - d\hat{\mathbf{n}} \quad (2.2)$$

The object lies in the FOV of the optical sensor if it satisfies the following constraints:

$$\begin{cases} -\frac{w}{2} \leq u' \leq \frac{w}{2} \\ -\frac{h}{2} \leq v' \leq \frac{h}{2} \end{cases} \quad (2.3)$$

where u' and v' are the horizontal and vertical coordinates of \mathbf{p}' respectively and w and h are the width and height of the projection plane, see Figure 2.1. These are calculated in the following way:

$$w, h = \tan \theta \cdot (\mathbf{p} \cdot \hat{\mathbf{n}}) \quad (2.4)$$

where θ is the FOV angle.

2.2. Error

In an ideal world it would be possible to measure the exact position of an object relative to the optical sensor. However, we do not live in an ideal world and at every step of the measurement process errors are introduced. In this subsection the different error sources that influence the optical measurements will be discussed.

The first error is the noise. Noise is a random, unwanted disturbance in all non ideal electronic signals. This noise error causes random fluctuations in the measured signal. There are multiple different types of noise, there is both internal noise generation (in the electronics of the sensor) and external noise. The internal noise can be split up into two different noise sources, read-out noise and dark noise. Read-out noise, σ_{ro} , is caused by the internal fluctuations and noise of the components of the sensor. Dark noise, σ_{dark} , is caused by thermal conditions of the sensor. External noise is noise caused by the environment, for example, the light of stars or the reflection of sunlight by the Moon. In the SNR calculation this noise is represented by the e_b .

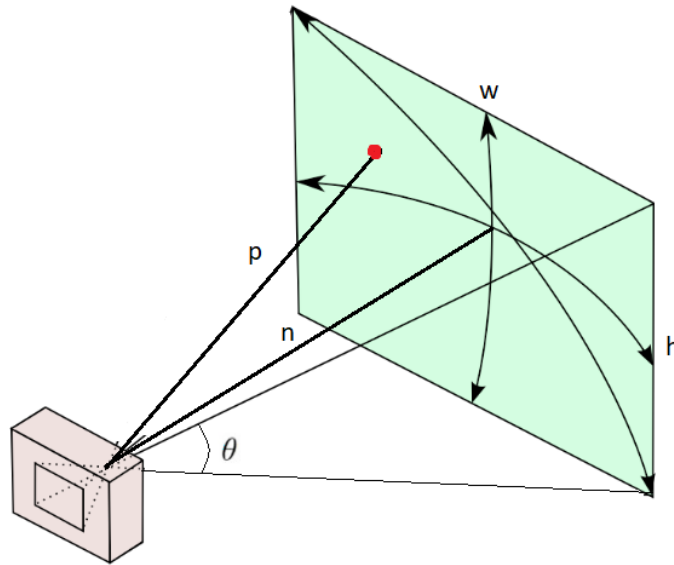


Figure 2.1: FOV check

Another error that is present for all optical measurements is the pointing error. A pointing error is the difference between the intended pointing angle of a sensor/instrument versus the actual pointing angle. The intended angle at which the object is detected is thus slightly wrong and leads to an error in the OD. Pointing errors can occur due to, misalignment's in the sensors, external disturbances or miscalculations. For satellites additional pointing errors can occur due to, reaction wheel errors, star tracker errors or gyro errors (Ott et al., 2011). The average pointing error is around $1-\sigma = 1-5$ arc-seconds in a Gaussian distribution (Ansalone and Curti, 2013). For the first simulations a pointing error of $1-\sigma = 3$ arc-seconds will be used. The effect of smaller or larger pointing errors on the performance of the system will be investigated during the sensitivity analysis.

Additionally, the optical measurements will be made from a satellite. So only the relative angle between the satellite and the object will be known. To get the relative angle between the centre of the earth and the object, the position of the observing satellite needs to be known. This position can be determined using orbit determination, however, the orbit determination is not perfect so an error is introduced due to the uncertainty of the position vector of observing satellite. The orbit determination of an operational satellite is luckily a lot more precise than that of space debris. For (near) GEO based satellites the position can be determined with an accuracy of around 1 m (Guo et al., 2010)(Deng et al., 2014), this error becomes smaller as the semi-major axis becomes smaller. However, since it is not yet known in what the orbit of the satellites will be the upper value 1 m will be used in the following simulations. The effect of smaller or larger satellite position errors on the performance of the system will be investigated during the sensitivity analysis.

The pointing and satellite position error is added to the measurements in the following way. The position vector of the space debris object (target) can be written as (Ansalone and Curti, 2013):

$$\mathbf{r}_T = \rho \hat{\mathbf{L}} + \mathbf{r}_O + \epsilon_{r_0} \quad (2.5)$$

where \mathbf{r}_T is the position of the target, ρ the range between the target and the observer, \mathbf{r}_O the position vector of the observer, ϵ_{r_0} is the position error of the observing satellite and $\hat{\mathbf{L}}$ is the unit vector between the target and observer, all these vectors are expressed in the ECI frame, see Figure 2.2.

The angular measurement unit vector $\hat{\mathbf{L}}$ is noiseless, to add noise from a random direction, two different rotations are needed. Let:

$$\hat{\mathbf{L}} = l_1 \hat{\mathbf{k}}_1 + l_2 \hat{\mathbf{k}}_2 + l_3 \hat{\mathbf{k}}_3 \quad (2.6)$$

where $\hat{\mathbf{k}}_1, \hat{\mathbf{k}}_2, \hat{\mathbf{k}}_3$ are the unit vectors in the ECI frame, then one of these unit vectors are chosen such that:

$$\hat{\mathbf{L}} \times \hat{\mathbf{k}}_i \neq \mathbf{0} \quad (2.7)$$

The angular measurement with random noise then becomes:

$$\hat{\mathbf{L}}_{meas} = \hat{\mathbf{g}} \cos \beta + (\hat{\mathbf{L}} \times \hat{\mathbf{g}}) \sin \beta + \hat{\mathbf{L}}(\hat{\mathbf{L}} \cdot \hat{\mathbf{g}})(1 - \cos \beta) \quad (2.8)$$

where the versor $\hat{\mathbf{g}}$ is given by the following:

$$\hat{\mathbf{g}} = \hat{\mathbf{L}} \cos \alpha + (\hat{\mathbf{h}} \times \hat{\mathbf{L}} \sin \alpha) \quad (2.9)$$

with:

$$\hat{\mathbf{h}} = \frac{\hat{\mathbf{L}} \times \hat{\mathbf{k}}_i}{|\hat{\mathbf{L}} \times \hat{\mathbf{k}}_i|} \quad (2.10)$$

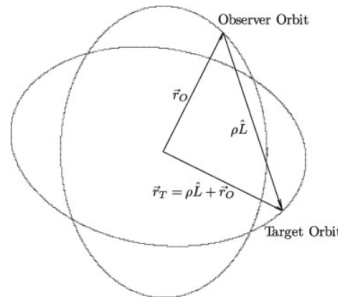


Figure 2.2: Target orbital position with respect to the observer (Ansalone and Curti, 2013)

where α is a angle determined by the Gaussian distribution with the standard deviation of the sensor, β is a randomly chosen angle from a uniform distribution between 0 and 2π .

2.3. Signal to Noise ratio

To know how close a space-based optical sensor should be placed to detect space debris objects as small as 1 to 10 cm, first it needs to be known how an optical sensor works. An optical sensor works by detecting the photons that hit the sensor, usually a charged coupled device (Krag et al., 2001). A space debris object can be detected if the ratio between the signal photons (the photons that are reflected by the object) and the noise photons, the SNR, detected by a optical sensor is higher than a certain threshold. To calculate the SNR ratio, first the following assumptions need to be made to simplify this calculation:

- All space debris objects are spherical in shape.
- All space debris objects have the same value for its albedo, from observations the mean value for space debris is 0.175 (Mulrooney et al., 2008).
- There is an equal number of diffuse and specular (mirrored) surfaces for the space-debris population. This assumption is supported by observational data (Shell, 2010).
- Grey-body reflectance is assumed, which means that the albedo is the same for all wavelengths.
- An SNR threshold of 2.5 will be used (Shell, 2010) (Xi et al., 2016).

Using these assumptions the signal photon flux is calculated using the following method (Shell, 2010). The apparent visual magnitude needs to be determined:

$$m_{obj} = m_{sun} - 2.5 \log \left[\frac{d^2}{R^2} \cdot \rho \cdot p(\psi) \right] \quad (2.11)$$

where R is the distance between the observer and the space debris object, d is the diameter of the object, m_{sun} is the visual magnitude of the sun and has a value of -26.73, ρ is the albedo of the object. The function, $p(\psi)$, is a function of the solar phase angle, ψ , and is given by the following expression for diffuse objects:

$$p_{diff}(\psi) = \frac{2}{3\pi} [\sin \psi + (\pi - \psi) \cos \psi] \quad (2.12)$$

while for specular surfaces the phase angle function is a constant 1/4. Equation 2.11 then becomes:

$$m_{obj} = m_{sun} - 2.5 \log \left[\frac{d^2}{R^2} \cdot \left| \frac{\rho_{spec}}{4} + \rho_{diff} \cdot p_{diff}(\psi) \right| \right] \quad (2.13)$$

The visual magnitude of the object is then converted to the resulting signal photon flux, E_{RSO} that reaches the sensor in the following way:

$$E_{RSO} = 5.6 \times 10^{10} \cdot 10^{-0.4 \cdot m_{obj}} \quad (2.14)$$

The SNR is then calculated using the following method (Tola, 2015). The signal photon flux is used to determine the number of electrons generated by the charge coupled device, e_s , as a result of the signal photons hitting the sensor:

$$e_s = E_{rs0} \cdot \tau \cdot QE \cdot A \quad (2.15)$$

where τ is the optical transmittance, for the simulation a value of 0.75 is used (Shell, 2010), A is the aperture area, QE is the quantum efficiency of the sensor. The per-pixel noise due to read-out noise, dark noise, and background noise is:

$$\sigma_{pixel}^2 = \sigma_{ro}^2 + E_{background} \cdot t_{exp} + \sigma_{dark} \quad (2.16)$$

where σ_{ro} is the read out noise, t_{exp} is the exposure time which is determined depending on the constellation design and FOV of the sensor. The exposure time should always be longer than the dwell time (the total duration for which the light spot created by the space debris object is over a single pixel),

t_d , so the exposure time will be set equal to the maximum possible dwell time encountered during the simulation. The dwell time is calculated as follows:

$$t_d = \frac{\theta}{\omega \times w} \quad (2.17)$$

where θ is the FOV angle, ω is the angular velocity of the space debris object with respect to the optical sensor and w is the number of pixels in each row and column of the charge coupled device. The maximum possible dwell time occurs when the observing satellite and space debris object lie in the same orbital plane and when the angular distance of space debris object to the observing satellite is π radians to the observing satellite. However, since a space debris object can only be observed if it lies in the FOV of the optical sensor, the maximum possible dwell time is calculated when a space debris is located at the edge of the FOV from a co-planar observing satellite.

The $E_{background}$ is calculated using the following expression:

$$E_{background} = 5.6 \times 10^{10} \cdot 10^{-0.4 \cdot m_{background}} \quad (2.18)$$

where $m_{background}$ is the apparent visual magnitude, this value can change depending on the viewing direction of the optical sensor, solar activity, and other factors, however, the commonly used average sky brightness for space based sensors is $22 \text{ } m_v/\text{arcsec}^2$ (Shell, 2010). The SNR is then determined using the following equation:

$$SNR = \frac{e_s \times t_d}{\sqrt{e_s \times t_d + \sigma_{pixel}^2}} \quad (2.19)$$

For the simulation, some of the parameters of the charge coupled device will be based off a off the shelf charge-couple device. The CCD270-00 F5 ¹ produced by Teledyne imaging will be used, this charge coupled device has been extensively tested and will be used for ESA's Plato mission (Endicott et al., 2012), which also uses optical observations in the visible wavelength. The specifications of this charge coupled device can be seen in Table 2.1.

An example of a SNR calculation for a space debris object observed by a space based optical sensor is provided in (Shell, 2010). Here it is shown that a 5 cm space debris object in GEO observed by a GEO based optical sensor at a distance of 736 km with a difference in inclination of 7.5 degrees, using a comparable charge-coupled device and a aperture size of 5 cm would result in a SNR of around eight, while a 1 cm sized space debris object in the same orbit would result in a SNR of around one.

Table 2.1: Charge-coupled device parameters

QE	87	[%]
σ_{ro}	0.8	[e ⁻]
σ_{dark}	28	[e ⁻]

¹<https://www.teledyneimaging.com/en/aerospace-and-defense/products/sensors-overview/ccd/ccd270-00-f5/>
accessed: 10/1/2023

3

Orbit propagation

To assess the extent to which a constellation of satellites with optical sensors can increase the surveillance of 1-10 cm size space debris in GEO, the positions of both the satellites and space debris objects need to be known. Therefore, the orbits of these objects need to be propagated. In Section 3.1 the difference in orbit propagation between satellites and space debris objects will be discussed, following this Section 3.2 described the reference frames that will be used. In Section 3.3, the different transformations needed to change between reference frames will be explained. Section 3.4 discusses the different sets of state variables that will be used in the simulations. The to be used force and environment models are talked about in Section 3.5, and finally Section 3.6 discusses the different equations of motions that will be used.

3.1. Space debris objects vs satellites

The orbit propagation for the space debris objects and the satellites will be different from each other. The orbit of the space debris objects should be a relatively accurate representation of a real orbit and be use a more precise force model compared to the force models used in the estimation models. This is because for real life orbit determination the force model used will always slightly differ from the real dynamics acting on the space debris object. The use of a force model that is too simplified and similar to the force model used in the estimation methods will thus lead to unrealistically high accuracies. A realistic orbit of the space debris objects is thus needed to accurately assess the performance of a similar real life system.

For the satellites the accuracy of the orbit is less important, because the accuracy of the orbit does not have an effect on the performance of the system. A small deviation from the real life orbit will not have a significant effect on the orbit determination methods and the number of observations made. So to save computational time, a more simplified force model can be used for the satellite orbit propagation, because this will not effect the final performance of the system. The differences in the orbit propagation also means that the used reference frames, transformations, state variables, force models and equations of motion will differ.

The method for generating the initial states for the space debris objects and the satellites is also different. The initial states for the different satellites in the constellation are design variables, a list of Kepler elements are provided by the user for each satellite and these are used for the orbit propagation. The initial states of the space debris objects are randomly generated from a statistical distribution, which can be seen in Figure 3.1. The semi-major axis of the space debris objects roughly follow a normal distribution centered with a mean of around 42,200 km. All inclinations lie between 0 and 15 degrees and the number of space debris objects increases as the inclination gets higher. Most of the objects have an eccentricity close to zero and the number of objects rapidly decreases as the eccentricity gets bigger. Probability functions will be used that closely resemble these distributions. The distribution was generated by using publicly available orbit information of space debris objects in GEO ¹. Only the distributions of the semi-major axis, inclination and eccentricity are shown. This is because the distribution of the other Kepler elements where close to uniform. The orbital information are of course

¹<https://www.space-track.org>: date accessed:10/11/2022

only of larger space debris objects (>10 cm), however, there are no significant differences between the distributions of Kepler elements for different size's of space debris for which TLE's are available, so the existing space debris objects between 1 cm and 10 cm will most likely follow the same distribution. One additional note on the distribution of the inclinations of the space debris objects, the objects usually start with an inclination close to zero, however, the object gradually increase their inclination to a maximum of around 15 degrees (Schildknecht et al., 2004).

3.2. Reference frames

Not all computations done in the simulation will use the same reference frame. It is, therefore, important to have a clear overview of which reference frames will be used and what transformations need to be performed to change to a different reference frame. The three reference frames that will be used are the Earth centered inertial (ECI), Body fixed and the Local Vertical Local Horizon (LVLH) reference frame, shown in Figure 3.2. The ECI frame will be used for the orbital propagation of the space debris objects and the satellites. Optical measurements are measured in the reference frame of the observing satellite, therefore, the Body fixed frame will be used for the simulation of the optical measurements, the Body fixed frame can be defined in different manners. To decrease the computational cost it has been decided to let the Body fixed frame coincide with the LVLH reference frame, this allows the measurements to be converted to the ECI frame with one transformation instead of two. The space debris objects will only use the ECI reference frame, while the satellites use all reference frames described in this section.

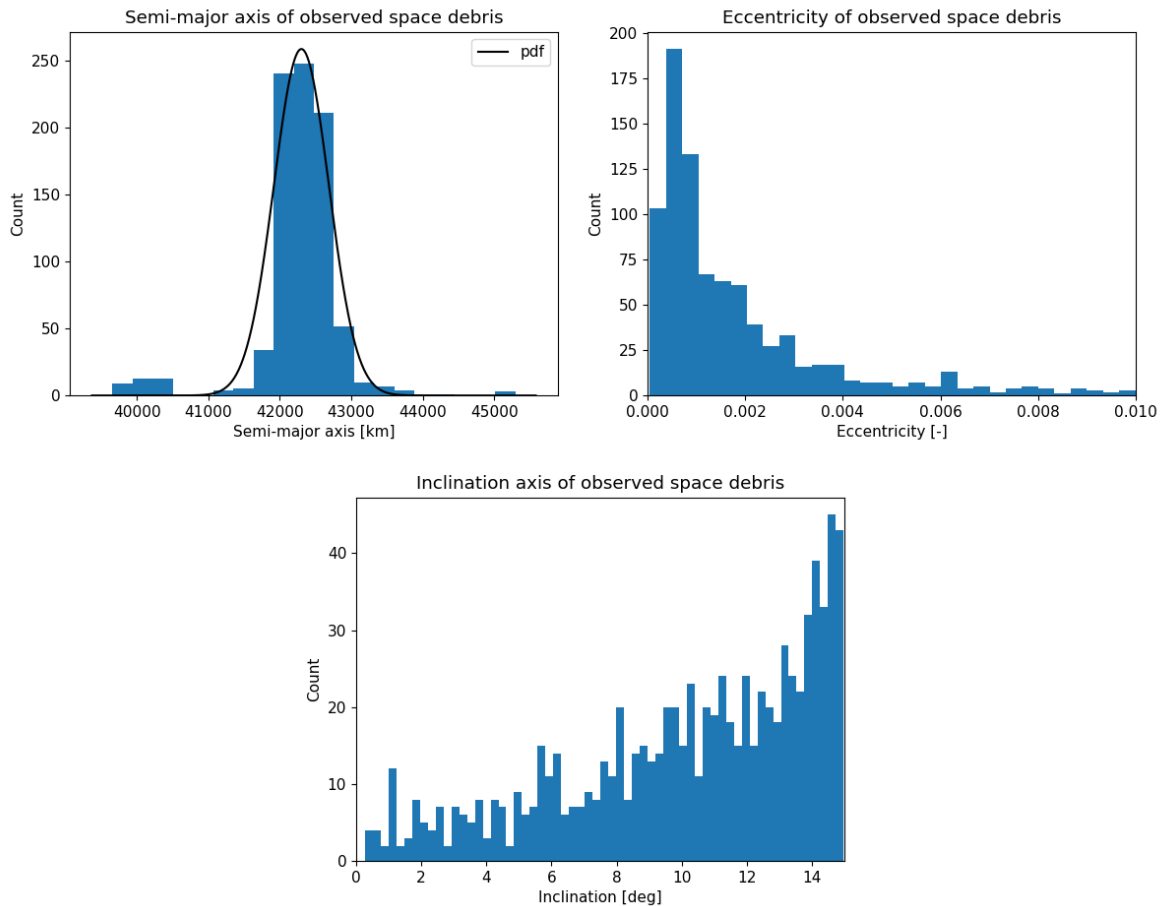


Figure 3.1: Distribution of Kepler elements of space debris in GEO region

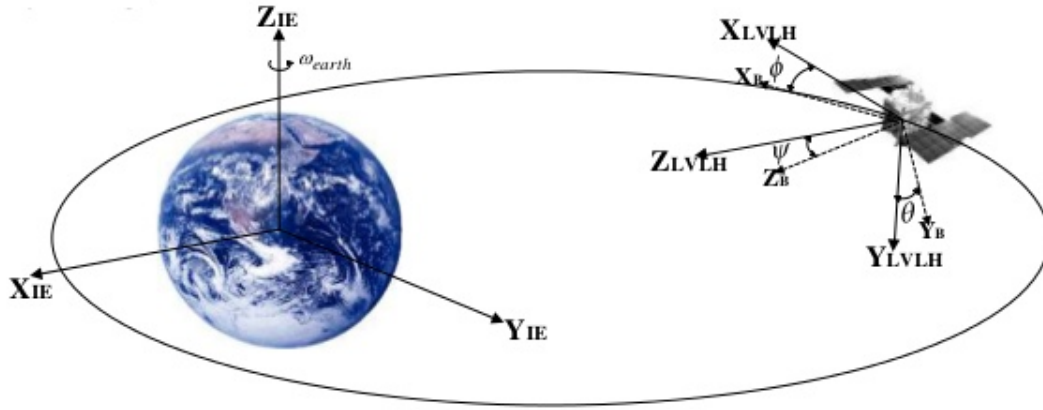


Figure 3.2: Body fixed, LVLH, ECI reference frames (Ismail, 2016)

3.2.1. Earth centered inertial reference frame

The ECI reference frame has its origin in the centre of mass of the Earth. The x_{ECI} axis points in the direction of the vernal equinox. The z_{ECI} axis is pointed along the rotational axis of the Earth, while the y_{ECI} axis completes the right handed coordinate system. The $x_{\text{ECI}}, y_{\text{ECI}}$ plane coincides with the equatorial plane. However, due to the precession of the rotational axis of the Earth, the vernal equinox is not fixed. Therefore, the orientation of the x_{ECI} is usually defined to point in the direction of the vernal equinox at a certain epoch. The most commonly used ECI frame is the J2000 frame, where the x_{ECI} axis points toward the vernal equinox measured at 01-01-2000 at 12:00 terrestrial time, this reference frame will also be used for the orbit propagation.

3.2.2. Body Fixed frame

As mentioned before, the body fixed reference frame, \mathcal{F}_{BF} , is commonly used for the representation of observation angles or vectors. The body fixed frame is uniquely defined for each satellite. But it is common to have the origin of this reference frame in the centre of mass of the satellite and to have one of the planes of the reference frame to coincide with the symmetry axis of the satellite (Wakker, 2015). However, since the propagation of the satellite will treat the satellite as a point mass, no rotational dynamics will be applied. It is, therefore, beneficial to let the body fixed frame coincide with the Local Vertical Local Horizon reference frame, this will make the transformation between the observation in the body fixed frame to the ECI reference frame easier.

3.2.3. Local Vertical Local Horizon

The Local Vertical Local Horizon reference frame, $\mathcal{F}_{\text{LVLH}}$, has its origin in the centre of mass of the satellite. One of either the x_{LVLH} or y_{LVLH} points along the velocity vector of the satellite. The z_{LVLH} axis is commonly pointed in the radial direction of orbit, usually towards the centre of mass of the object the satellite is orbiting. The remaining axis then completes the right-handed reference frame.

3.3. Transformations

Since \mathcal{F}_{BF} and $\mathcal{F}_{\text{LVLH}}$ will coincide in the simulation, only one reference frame transformation needs to be performed, the transformation between the LVLH and the ECI reference frame. This transformation can be performed by performing three rotations around the axis of the ECI frame:

$$[x_{\text{LVLH}} \ y_{\text{LVLH}} \ z_{\text{LVLH}}]^T = \mathbf{R}_z(\theta_t) \mathbf{R}_x(i) \mathbf{R}_z(\Omega) [x_{\text{ECI}} \ y_{\text{ECI}} \ z_{\text{ECI}}]^T \quad (3.1)$$

with the following rotation matrices:

$$\mathbf{R}_z(\theta_t) = \begin{bmatrix} \cos \theta_t & -\sin \theta_t & 0 \\ \sin \theta_t & \cos \theta_t & 0 \\ 0 & 0 & 1 \end{bmatrix} \quad \mathbf{R}_x(i) = \begin{bmatrix} 1 & 0 & 0 \\ 0 & \cos i & -\sin i \\ 0 & \sin i & \cos i \end{bmatrix} \quad \mathbf{R}_z(\Omega) = \begin{bmatrix} \cos \Omega & -\sin \Omega & 0 \\ \sin \Omega & \cos \Omega & 0 \\ 0 & 0 & 1 \end{bmatrix} \quad (3.2)$$

where θ_t is the argument of latitude ($\omega + \theta$), i is the inclination of the orbit, and Ω is the right ascension of the ascending node.

3.4. State variables

Different sets of state variables will have to be used for the simulation of the system. In this section these state variables will be described, along with the reason why these sets of state variables are needed for the simulation. Furthermore, the transformations between the different state variables will be discussed.

3.4.1. Cartesian coordinates

Cartesian coordinates will be used for the orbit propagation of the satellites. Cartesian coordinates have been chosen because this allows the Kepler orbit of the satellites to be calculated without needing to transform to state variable, this makes it computationally faster than using other sets of state variables. The Cartesian coordinates consist of x , y and z -coordinates to describe the position of an object in three dimensional space and \dot{x} , \dot{y} and \dot{z} are used to represent the velocity of an object. Which gives the following state vector:

$$\mathbf{x} = [x, y, z, \dot{x}, \dot{y}, \dot{z}]^T \quad (3.3)$$

3.4.2. Kepler elements

Kepler elements will be used to generate the initial states of the satellites and space debris. This is because the publicly available orbit information of the space debris objects, see Figure 3.1, are provided in Kepler elements. Additionally, Kepler elements can provide a better understanding of the actual state of the object in comparison to for example Cartesian or Rodrigues parameters. This will be especially useful for answering research question 1.3, how the orbit of the space debris object changes the performance of the system. The state vector expressed in Kepler elements gives the following:

$$\mathbf{x} = [a, e, i, \omega, \Omega, \theta]^T \quad (3.4)$$

where a is the semi-major axis, e the eccentricity, i the inclination, ω the argument of periapsis, Ω the longitude of the ascending node and θ the true anomaly, see Figure 3.3. Additionally, the mean anomaly, M , and eccentric anomaly, E , are sometimes added to this state vector, these variables are used for the transformation between state variable sets.

To transform from Cartesian coordinates to Kepler elements the following computations need to be performed, the semi-major axis and eccentricity can be computed in the following way (Wakker, 2015):

$$r = \|\mathbf{r}\| \quad ; \quad V = \|\mathbf{V}\|; \quad \mathbf{h} = \mathbf{r} \times \mathbf{V}; \quad \mathbf{N} = \begin{pmatrix} 0 \\ 0 \\ 1 \end{pmatrix} \times \mathbf{h} \quad (3.5)$$

$$a = \frac{1}{\left(\frac{2}{r} - \frac{V^2}{\mu}\right)}; \quad \mathbf{e} = \frac{\mathbf{V} \times \mathbf{h}}{\mu} - \frac{\mathbf{r}}{r}; \quad e = \|\mathbf{e}\| \quad (3.6)$$

where μ is Earth's gravitational parameter. The other Kepler elements can be found using the following equations:

$$i = \arccos\left(\frac{h_z}{\|\mathbf{h}\|}\right); \quad N_{xy} = \sqrt{N_x^2 + N_y^2}; \quad \Omega = \text{atan2}\left(\frac{N_y}{N_{xy}}, \frac{N_x}{N_{xy}}\right) \quad (3.7)$$

$$\omega = \pm 1 \cdot \arccos(\mathbf{e} \cdot \mathbf{N}); \quad \theta = \pm 1 \cdot \arccos(\mathbf{r} \cdot \mathbf{e}) \quad (3.8)$$

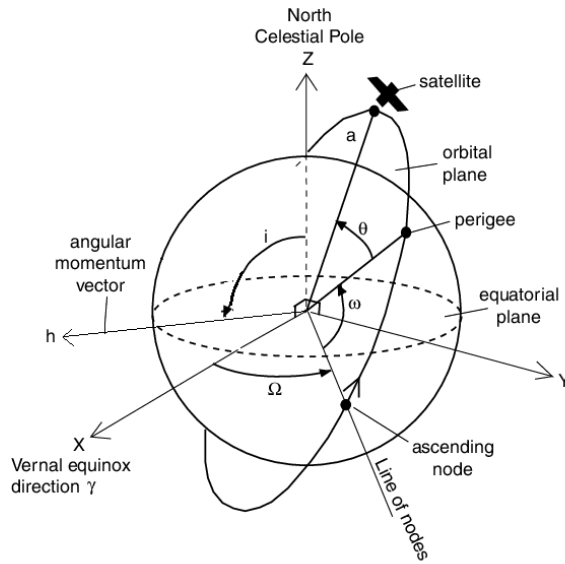


Figure 3.3: Kepler elements (De Weck et al., 2008)

where the sign of ω is +1 if $(\mathbf{N} \times \mathbf{e}) \cdot \mathbf{h} > 0$, the sign of θ is +1 if $(\mathbf{e} \times \mathbf{r}) \cdot \mathbf{h} > 0$, otherwise the signs are -1. The eccentric anomaly and mean anomaly can then be found in the following way:

$$E = 2 \cdot \text{atan} \left(\sqrt{\frac{1-e}{1+e}} \tan \frac{\theta}{2} \right); M = E - e \sin E \quad (3.9)$$

The transformation from Kepler elements to Cartesian coordinates is done using the following method (Wakker, 2015):

$$\begin{pmatrix} \xi \\ \eta \end{pmatrix} = \begin{pmatrix} r \cos \theta \\ r \sin \theta \end{pmatrix}; \quad \begin{pmatrix} x \\ y \\ z \end{pmatrix} = \begin{bmatrix} l_1 & l_2 \\ m_1 & m_2 \\ n_1 & n_2 \end{bmatrix} \begin{pmatrix} \xi \\ \eta \end{pmatrix}; \quad \begin{aligned} \dot{x} &= \frac{\mu}{H} [-l_1 \sin \theta + l_2(e + \cos \theta)] \\ \dot{y} &= \frac{\mu}{H} [-m_1 \sin \theta + m_2(e + \cos \theta)] \\ \dot{z} &= \frac{\mu}{H} [-n_1 \sin \theta + n_2(e + \cos \theta)] \end{aligned} \quad (3.10)$$

with:

$$\begin{aligned} l_1 &= \cos \Omega \cos \omega - \sin \Omega \sin \omega \cos i \\ l_2 &= -\cos \Omega \sin \omega - \sin \Omega \cos \omega \cos i \\ m_1 &= \sin \Omega \cos \omega + \cos \Omega \sin \omega \cos i \\ m_2 &= -\sin \Omega \sin \omega + \cos \Omega \cos \omega \cos i; \quad H = \sqrt{\mu a (1 - e^2)} \\ n_1 &= \sin \omega \sin i \\ n_2 &= \cos \omega \sin i \end{aligned} \quad (3.11)$$

To find θ the eccentric anomaly needs to be found. There is no analytical solution for this, so this needs to be done iteratively in the following way:

$$E_{i+1} = E_i + \frac{M - E_i + e \sin E_i}{1 - e \cos E_i} \quad (3.12)$$

this calculation is repeated until it converges to a eccentric anomaly. The true anomaly can then be computed using the following formula:

$$\theta = 2 \arctan \left(\sqrt{\frac{1+e}{1-e}} \tan \frac{E}{2} \right) \quad (3.13)$$

3.4.3. Modified Equinoctial Elements

Modified Equinoctial Elements will be used for the orbit propagation of the space debris objects. There are multiple different methods which could have been used for the propagation the orbits of space

debris objects, Cowell, Encke, Kepler Elements, Modified equinoctial elements and the Unified State Model. The Modified equinoctial elements have been chosen for the propagation of the orbit of the space debris due its computational efficiency, accuracy and because it does not have singularities for orbital elements that will be used for the space debris population.

The state vector using Modified Equinoctial Elements are the following:

$$\mathbf{x} = [a, e_c, e_s, W_c, W_s, \lambda]^T \quad (3.14)$$

To transform classical Kepler elements to Modified Equinoctial Elements, the following equations can be used:

$$\begin{aligned} a &= a \\ e_c &= e \cos(\omega + \Omega) \\ e_s &= e \sin(\omega + \Omega) \\ W_c &= \sin(i) \sin(\Omega) \\ W_s &= \sin(i) \sin(\Omega) \\ \lambda &= \omega + \Omega + M \end{aligned} \quad (3.15)$$

3.5. Force and environment models

There is a significant difference between the force and environment models used for the satellites and space debris objects. For the satellites only the point mass gravity force due to the Earth is included. The force and environment model for the space debris objects is more extensive, taking into account all forces that have a significant effect on the orbit of the space debris objects, like the Earth's gravitational model, third body perturbations and solar radiation pressure. Other perturbations due to ocean or solid Earth tides, relativistic forces and drag did not have a large enough effect on the orbits of objects in GEO to be worth the additional computational cost (Roh et al., 2011)(Yoon et al., 2004)(Lee et al., 1997).

3.5.1. Point mass gravity

The point mass gravity is the only forces which will be used for the propagation of the orbit of the satellites. As already mentioned in Section 3.1, the orbit of the satellites does not have to be very accurate since the accuracy of the satellite orbit will not effect the performance of the system as long as the orbit of the satellites remains constant for the whole simulation time. Using only point mass gravity will provide a computationally fast circular orbit for the satellites. Adding more forces to the dynamical model will only increase the computational cost with no added benefit to the research.

The point mass gravity can be expressed in the following way:

$$\mathbf{a}_{point} = -\frac{\mu}{r^2} \mathbf{r} \quad (3.16)$$

where μ is the standard gravitational parameter of Earth equal to $3.986 \times 10^{14} [\text{m}^3 \text{s}^{-2}]$.

3.5.2. Earth's gravitational model

For short term orbit propagation it was found in literature that using a spherical harmonic gravity field with a degree and order of five gave sufficiently accurate results (Roh et al., 2011) (Yoon et al., 2004). Using a higher degree and order did give an even more accurate orbit, however, for short term orbit propagation (less than a year) the difference in accuracy was not worth the extra computational cost. The spherical harmonic gravity field is expressed in the following way (Wakker, 2015):

$$U(\mathbf{r}) = \frac{\mu}{r} \sum_{n=0}^{n_{max}} \sum_{m=0}^n \left(\frac{R_{Earth}}{r} \right)^n \bar{P}_{nm}(\sin \phi) (\bar{C}_{nm} \cos m\theta + \bar{S}_{nm} \sin m\theta) \quad (3.17)$$

where R is the mean equatorial radius, θ is the geographic longitude, ϕ is the geocentric latitude, $C_{n,m}$ and $S_{n,m}$ are constants which depend on the chosen model. The degree and order, n, m , are as mentioned before 5 and 5. The function $\bar{P}_{nm}(\sin \phi)$ is the Legendre function:

$$\begin{aligned} \bar{P}_n(x) &= \frac{1}{(-2)^n n!} \frac{d^n}{dx^n} (1-x^2)^n \\ \bar{P}_{n,m} &= (1-x^2)^{m/2} \frac{d^m \bar{P}_n(x)}{dx^m} \end{aligned} \quad (3.18)$$

The gravitational force acting on a body orbiting the Earth would then be:

$$\mathbf{a}_{grav} = \nabla U(\mathbf{r}) \quad (3.19)$$

3.5.3. Third body perturbation

In literature it was found that only the point mass gravitational effect of the Sun and the Moon need to be included in the force model to provide an accurate orbit. The effects of other bodies in the solar system did not have an significant enough effect on the accuracy compared to the added computational cost (Roh et al., 2011) (Yoon et al., 2004) (Lee et al., 1997). The acceleration caused by these third bodies can be described in the following manner (Wakker, 2015):

$$\mathbf{a}_{body} = \mu_{body} \left(-\frac{\mathbf{r}_{body-Object}}{\|\mathbf{r}_{body-Object}\|^2} + \frac{\mathbf{r}_{body-Earth}}{\|\mathbf{r}_{body-Earth}\|^2} \right) \quad (3.20)$$

3.5.4. Solar radiation pressure

The only other perturbation that needs to be included in the force model is the solar radiation pressure, all other perturbations did not have an significant enough effect on the accuracy to be worth the extra computational cost (Roh et al., 2011) (Yoon et al., 2004). The acceleration due to the Solar radiation pressure can be written as follows (Wakker, 2015):

$$\mathbf{a}_{solarrad} = -vP \frac{c_{RA}}{m} \frac{\mathbf{r}_{Sun-Object}}{\|\mathbf{r}_{Sun-Object}\|} \quad (3.21)$$

where P is the solar radiation pressure, A is the cross sectional area of the object, c_r is the reflection coefficient which is usually assumed to be equal to 1 (Schutz et al., 2004), v is the shadow function, which is zero if the object lies in the shadow of the Earth and one if it is out of the shadow. The object is in the shadow if (Curtis, 2013):

$$\phi > v_1 + \frac{\pi}{2} \quad \text{with : } v_1 = \arccos \frac{R_E}{r} \quad \text{and } \phi = \arccos(\mathbf{r} \cdot \mathbf{r}_{Sun}) \quad (3.22)$$

3.5.5. Ephemerides model

Both the acceleration due to the third body perturbations as well as the solar radiation pressure, require the position vector between the Earth and a third body or between the object and the Sun. To compute these position vectors, the position of this third body is required. The position of these third bodies are contained in the ephemerides model, which give the position of a body as a function of time. The ephemerides model can be numerically generated, by assuming the body has a Kepler orbit (possibly with analytical variations in the Kepler elements). However, the ephemerides model can also be taken from tabulated data, which are usually obtained by numerical integration. These have a higher accuracy compared to the Kepler orbits while also not being computationally expensive and are therefore also the preferred ephemerides model for this simulation.

3.6. Equations of motion

As discussed earlier the orbit propagation for the space debris objects will be done using modified equinoctial elements, while for the satellites an Kepler orbit will be used.

3.6.1. Modified equinoctial elements

The equations of motion for these modified equinoctial orbital elements are (Brouwer and Clemence, 2013):

$$\frac{da}{dt} = 2 \frac{na}{GM_{\oplus}} \frac{\partial R}{\partial M} \quad (3.23)$$

$$\frac{de_c}{dt} = \frac{na}{GM_{\oplus}} \sqrt{1-e^2} \frac{\partial R}{\partial e_s} - \frac{na}{GM_{\oplus}} \frac{e_s}{\sqrt{1-e^2}} \tan \frac{i}{2} \frac{\partial R}{\partial i} - \frac{na}{GM_{\oplus}} \frac{e_c \sqrt{1-e^2}}{1+\sqrt{1-e^2}} \frac{\partial R}{\partial M} \quad (3.24)$$

$$\frac{de_s}{dt} = \frac{na}{GM_{\oplus}} \sqrt{1-e^2} \frac{\partial R}{\partial e_c} + \frac{na}{GM_{\oplus}} \frac{e_c}{\sqrt{1-e^2}} \tan \frac{i}{2} \frac{\partial R}{\partial i} - \frac{na}{GM_{\oplus}} \frac{e_s \sqrt{1-e^2}}{1+\sqrt{1-e^2}} \frac{\partial R}{\partial M} \quad (3.25)$$

$$\frac{dW_c}{dt} = -\frac{na \cos i}{GM_\oplus \sqrt{1-e^2}} \frac{\partial R}{\partial W_s} - \frac{na}{GM_\oplus} \frac{W_c \cos i}{\sqrt{1-e^2}(1+\cos i)} \left(\frac{\partial R}{\partial \tilde{\omega}} + \frac{\partial R}{\partial M} \right) \quad (3.26)$$

$$\frac{dW_s}{dt} = -\frac{na \cos i}{GM_\oplus \sqrt{1-e^2}} \frac{\partial R}{\partial W_c} - \frac{na}{GM_\oplus} \frac{W_s \cos i}{\sqrt{1-e^2}(1+\cos i)} \left(\frac{\partial R}{\partial \tilde{\omega}} + \frac{\partial R}{\partial M} \right) \quad (3.27)$$

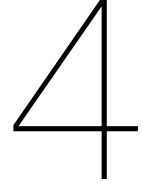
$$\frac{d\lambda}{dt} = -\frac{2nar}{GM_\oplus} R + \left(1 - \sqrt{1-e^2}\right) \frac{\partial(\omega + \Omega)}{\partial t} + 2\sqrt{1-e^2} \sin^2 \frac{i}{2} \frac{\partial \Omega}{\partial t} \quad (3.28)$$

where n is the mean orbital angular velocity, G is the gravitational constant, M_\oplus is the mass of the Earth, M is the mean anomaly, $\tilde{\omega}$ is the perigee longitude, R is the perturbation function, which contains all the perturbations that are included in the simulation (Yoon et al., 2004).

3.6.2. Kepler orbit

The equations of motion for the Kepler orbit can be written in the following way:

$$\begin{bmatrix} x_{i+1} \\ y_{i+1} \\ z_{i+1} \\ v_{x,i+1} \\ v_{y,i+1} \\ v_{z,i+1} \end{bmatrix} = \begin{bmatrix} x_i + v_{x_i} * \delta t \\ y_i + v_{y_i} * \delta t \\ z_i + v_{z_i} * \delta t \\ v_{x_i} + a_{x_i} * \delta t \\ v_{y_i} + a_{y_i} * \delta t \\ v_{z_i} + a_{z_i} * \delta t \end{bmatrix} \quad (3.29)$$



Estimation methods

To turn the measurement into orbit estimations different orbit determination methods will be used. An initial orbit determination will first be used to provide an initial guess for the more precise orbit determination method. In this chapter the orbit estimation methods that will be used during the simulation are described. In Section 4.1 the initial orbit estimation method will be discussed and in Section 4.2 the precise orbit determination method will be talked about.

4.1. Simplex Fusion

If the initial guess for the position of the space debris object is not accurate enough, the sequential estimation methods will not converge to a viable solution. Therefore, an initial orbit determination (IOD) needs to be performed that will result in a reasonably accurate orbit estimation. The observing satellites will only be able to measure the unit direction vector from the satellite to the target, no range information is available. Therefore, so called angles-only orbit determinations need to be used. These methods provide an initial orbit estimation using only the unit direction vector. There exists many angles-only IOD methods, such as the Gauss and double-r method (Vallado, 2001). However, most of the commonly used angles-only IOD methods perform very poor for co-planar observation cases, space based observations and or require observations with very large time intervals due to the poor observability of these objects (Karimi and Mortari, 2011).

The proposed system will make use of space based observations, where co-planar observations and observations with a short time interval are likely to occur. The commonly used angles-only IOD methods are therefore not suitable for this problem. A simplex fusion method for IOD proposed in (Handley and Hagerty, 2020) performs well for these specific cases as well as for more conventional observations cases. Additionally, this method can easily combine observations of multiple satellites even if the satellites can only make observations for a part of the total observation time, which is also something that is likely to happen for the proposed system. For these reasons the simplex fusion method will be used. The simplex fusion method consists of three parts, the sensor data fusion, the cost function and the optimisation of the cost function, these three parts will be discussed in the following sections.

Sensor data fusion

The simplex fusion method works as follows (Handley and Hagerty, 2020), the IOD problem for n observations can be written as follows:

$$\begin{pmatrix} \mathbf{r}_1 \\ \mathbf{r}_2 \\ \vdots \\ \mathbf{r}_n \end{pmatrix} = \begin{pmatrix} \mathbf{R}_1 + \rho_1 \hat{\mathbf{p}}_1 \\ \mathbf{R}_2 + \rho_2 \hat{\mathbf{p}}_2 \\ \vdots \\ \mathbf{R}_n + \rho_n \hat{\mathbf{p}}_n \end{pmatrix} \quad (4.1)$$

where \mathbf{r}_i is the position vector of the space debris object, \mathbf{R}_i is the position vector of the observing satellite, $\hat{\mathbf{p}}_i$ is the unit direction vector from the satellite to the space debris object and ρ_i is the range

between the satellite and space debris object. All the continuous observations of a single space debris object will then be combined in the following way:

$$\begin{pmatrix} t_1 & \mathbf{R}_1 & \hat{\mathbf{p}}_1 \\ t_2 & \mathbf{R}_2 & \hat{\mathbf{p}}_2 \\ \vdots & \vdots & \vdots \\ t_n & \mathbf{R}_n & \hat{\mathbf{p}}_n \end{pmatrix} \quad (4.2)$$

where t_i is the time at which the observation has been made.

Cost function

For each observation set, the state vector of the space debris object at one time, t_k , is estimated. This state vector is estimated by optimising the cost function using a candidate solution. The cost function for each candidate solution is determined in the following way, firstly, the state vector is propagated to each time step, t_i , in the observation set, this is done by using an RK4 integrator, this integrator was chosen because it is a fixed step size integrator that is computationally fast and provides high enough accuracies for the relatively short integration times that will be used. Using the state vectors at each time, t_i , a measurement vector is calculated between the propagated candidate state vector and the actual position vector of the observing satellites, $\hat{\mathbf{p}}_i$. For each time step, t_i , the angle error, β_i , between the actual measurement vector, $\tilde{\mathbf{p}}_i$, and the measurement vector using the propagated candidate solution, $\hat{\mathbf{p}}_i$, is calculated in the following way:

$$\beta_i = \tan^{-1} \frac{\|\hat{\mathbf{p}}_i \times \tilde{\mathbf{p}}_i\|}{\hat{\mathbf{p}}_i \cdot \tilde{\mathbf{p}}_i} \quad (4.3)$$

This will result in n angle errors for each candidate solution. The cost function for that candidate solution is then determined by using the sum of squares of the n angle errors:

$$J = \sqrt{\sum_{i=1}^n |\beta_i|^2} \quad (4.4)$$

The cost function will be determined in this way for all candidate solutions and this cost value will be used as an input for the optimisation method described in the following section.

Optimisation

The cost function is minimised using the Nelder-Mead simplex optimiser, see Chapter 5. A simplex is the smallest convex set containing all vertices, for example, a 1-dimensional simplex is a line, a 2-dimensional simplex is a triangle, a 3-dimensional simplex is a tetrahedron and so on for the higher dimensions. The initial simplex consists of $n + 1$ points in n -dimensional space, in this case the state vector (x, y, z, vx, vy, vz) needs to be estimated, so n is equal to six.

The initial simplex is generated by projecting the measurement vector at a time, t_k , from the position of the observing satellites, using 40 different plausible ranges, R_n , see Figure 4.1. The upper and lower limit of these plausible ranges are determined by subtracting the semi-major axis of the observing satellite from the upper and lower bounds of the GEO region defined in Chapter 3. The fitness for each of the 40 candidate solutions is then calculated, by determining the value of the cost function, J . The seven $(n + 1)$ best candidate solutions will then form the initial simplex.

The optimiser runs for a maximum of 400 iterations or until a tolerance of 10^{-8} is reached. The number of iterations was determined by looking at the difference in average position accuracy per number of iterations, see Figure 4.2, where it is clear that average position accuracy does not improve significantly after around 400 iterations, therefore the maximum number of iterations that will be used is 400.

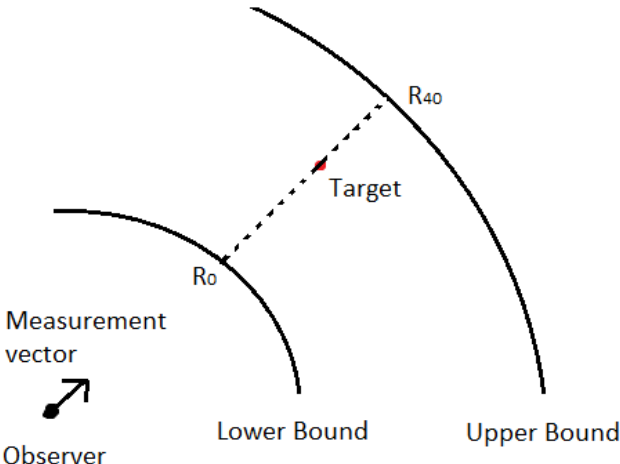


Figure 4.1: Initial simplex generation

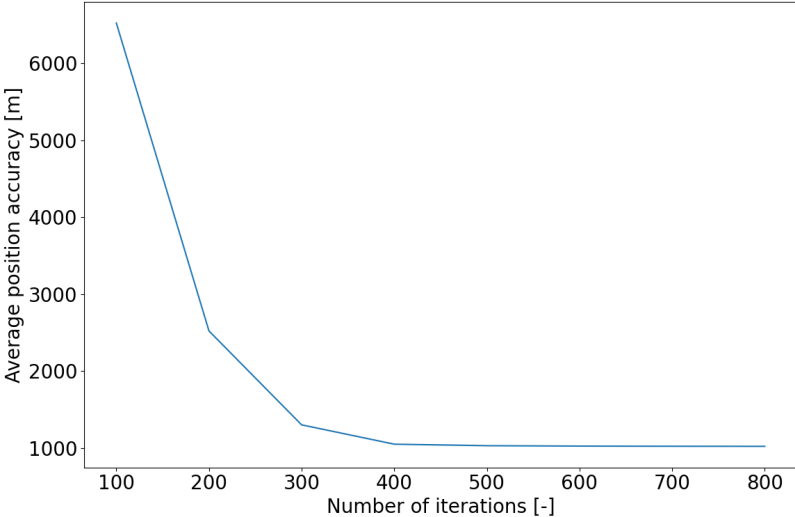


Figure 4.2: Average position accuracy as a function of iterations

4.2. Unscented Kalman filter

Depending on the constellation design, the time interval between two observation sets of a unique object can differ from one day to sometimes a couple of weeks. The orbit determination thus needs to be precise enough to make it possible to track the space debris object. Additionally, a sequential estimation method is preferred compared to a batch method, because, when one satellite detects a space debris object it needs to be able to perform real time orbit determination, in order for other satellites to start tracking the same object.

There are three commonly used sequential estimation methods, the extended Kalman filter (EKF), the unscented Kalman filter (UKF) and particle filters. Compared to an EKF, a UKF shows better performance for most problems, especially non-linear problems, for a similar computational cost. A particle filter normally provides a better accuracy than a UKF, however, due to the relatively slow dynamics in GEO, it is estimated that this increase in accuracy would be quite small compared to the UKF. A particle filter is also much more computationally expensive and considering that a large number of orbit estimations need to be performed for each run, it was decided to use a UKF.

The Unscented Kalman filter (UKF) is a non linear version of the Kalman filter. The UKF makes use of a minimal set of sigma points, which are a weighted set of sample points based on the covariance of the estimation. A unscented transformation, which is a function that estimates the result of a probability distribution transformed by a non-linear transformation, uses these sigma points to propagate the covariance and mean of the state distribution (Ebeigbe et al., 2021).

The sigma points are determined as follows (Julier and Uhlmann, 2004):

$$\begin{aligned} \mathbf{X}_{0,i}^a &= \mathbf{x}_i^e \\ \mathbf{X}_{k,i}^a &= \mathbf{x}_i^e + (\sqrt{(n+\lambda)\mathbf{P}_{i-1}^e})_k \quad \text{for } k = 1, \dots, n \\ \mathbf{X}_{k,i}^a &= \mathbf{x}_i^e - (\sqrt{(n+\lambda)\mathbf{P}_{i-1}^e})_k \quad \text{for } k = n+1, \dots, 2n \end{aligned} \quad (4.5)$$

where $\mathbf{X}_{k,i}^a$ is the k th column of \mathbf{X}_i^a , n is the dimension of the state vector, the matrix \mathbf{P} is the covariance matrix. The covariance matrix is a 6x6 matrix, which is initialised in the following way:

$$\mathbf{P}_0 = \begin{bmatrix} \sigma_{r,0}^2 \mathbf{I}_{3 \times 3} & 0 \\ 0 & \sigma_{v,0}^2 \mathbf{I}_{3 \times 3} \end{bmatrix} \quad (4.6)$$

where $\sigma_{r,0}$ and $\sigma_{v,0}$ are the initial position and velocity co-variances respectively. The matrix \mathbf{Q} is the process noise matrix, this matrix is initialised the following way:

$$\mathbf{Q}_0 = \begin{bmatrix} \sigma_{v,Q}^2 \mathbf{E}_{3 \times 3} & 0 \\ 0 & \sigma_{a,Q}^2 \mathbf{E}_{3 \times 3} \end{bmatrix} \quad (4.7)$$

the composite scalar λ is defined in the following way:

$$\lambda = \alpha^2(n+k) \quad (4.8)$$

where α is usually set to a small positive value (e.g., 1e-3) and κ is usually set to zero (Wan and Van Der Merwe, 2000). The k th column of the term $(\sqrt{(n+\lambda)(\mathbf{P}_i + \mathbf{Q}_k)})$ can be found by applying a Cholesky factorisation, which decomposes a positive-definite matrix into a lower triangular matrix and its corresponding conjugate transpose, this factorisation makes numerical solutions more efficient (Krishnamoorthy and Menon, 2013). A prediction for the state vector can then be made by using a weighted mean of the previously described sigma points in the following manner:

$$\mathbf{X}_i^p = \sum_{k=0}^{2n} W_i^{(m)} \mathbf{X}_{k,i|i-1}^a \quad (4.9)$$

with the following weights $W_i^{(m)}$:

$$W_0^{(m)} = \frac{\lambda}{\lambda+n}; \quad W_i^{(m)} = \frac{\lambda}{2(\lambda+n)}; \quad i = 1, \dots, 2n. \quad (4.10)$$

The covariance matrix is updated using the following equation:

$$\mathbf{P}_i^p = \sum_{k=0}^{2n} W_i^{(c)} [\mathbf{X}_{k,i|i-1}^a + \mathbf{X}_i^p][\mathbf{X}_{k,i|i-1}^a + \mathbf{X}_i^p]^T + \mathbf{Q} \quad (4.11)$$

where \mathbf{Q} is the process covariance matrix, the weights $W_k^{(c)}$ are given by:

$$W_0^{(c)} = \frac{\lambda}{\lambda+n} + (1 - \alpha^2 + \beta); \quad W_k^{(c)} = \frac{\lambda}{2(\lambda+n)}; \quad k = 1, \dots, 2n \quad (4.12)$$

with $\beta = 2$ (Wan and Van Der Merwe, 2000). The predicted measurements then become:

$$\mathbf{Y}_i^p = \sum_{k=0}^{2n} W_k^{(m)} \mathbf{Y}_{k,i|i-1}^a \quad (4.13)$$

The measurements are ordered in the following manner:

$$\mathbf{Y}^p = \begin{bmatrix} \hat{\mathbf{L}}_{s_1-t_i}^p \\ \vdots \\ \hat{\mathbf{L}}_{s_i-t_i}^p \\ \vdots \\ \hat{\mathbf{L}}_{s_q-t_i}^p \end{bmatrix} \quad (4.14)$$

where $\hat{\mathbf{L}}_{s_i-t_i}$ is the unit direction vector between the satellite and the object. The predicted measurements can then be calculated in the following manner:

$$\hat{\mathbf{d}}_{s_i-t_i}^p = \frac{\mathbf{r}_{t_i}^p - \mathbf{r}_{s_i}}{\sqrt{(\mathbf{r}_{t_i} - \mathbf{r}_{s_i}) \cdot (\mathbf{r}_{t_i} - \mathbf{r}_{s_i})}} \quad (4.15)$$

The covariance matrix that is associated with the measurements then becomes:

$$\mathbf{P}_i^{yy} = \sum_{k=0}^{2n} W_k^{(c)} [\mathbf{Y}_{k,i|i-1}^a - \mathbf{Y}_i^p][\mathbf{Y}_{k,i|i-1}^a - \mathbf{Y}_i^p]^T + \mathbf{R} \quad (4.16)$$

the matrix \mathbf{R} is the measurement covariance matrix:

$$\mathbf{R} = \sigma_m^2 E_{3n \times 3n} \quad (4.17)$$

where σ_m is the measurement covariance. The covariance matrix between the state and measurements is computed as follows:

$$\mathbf{P}_i^{xy} = \sum_{k=0}^{2n} W_k^{(c)} [\mathbf{X}_{k,i|i-1}^a - \mathbf{X}_i^p][\mathbf{Y}_{k,i|i-1}^a - \mathbf{Y}_i^p]^T \quad (4.18)$$

This can then be used for the computation of the Kalman gain matrix \mathbf{K}_i in the following way:

$$\mathbf{K}_i = \mathbf{P}_i^{xy} (\mathbf{P}_i^{yy})^{-1} \quad (4.19)$$

The estimation of the state and the covariance can then finally be updated using the following relations:

$$\mathbf{X}_i^e = \mathbf{X}_i^p + \mathbf{K}_i (\mathbf{Y}_i^m - \mathbf{Y}_i^p) \quad (4.20)$$

$$\mathbf{P}_i^e = \mathbf{P}_i^p + \mathbf{K}_i \mathbf{P}_i^{yy} \mathbf{K}_i^T \quad (4.21)$$

This next observation is then read, this is done until all observations have been read.

For example, an observer makes a measurement of the elevation, ϵ and declination, δ of a space debris object. These measurements will be non-linear. The UKF uses sigma points to approximate a linear function from the original non-linear function. These sigma points have two coordinates, ϵ and δ , the coordinates of these sigma points are dependent on the current estimation of the state (ϵ , δ) and the current covariance, according to Equation 4.5. These sigma points are then transformed using the non-linear dynamics that act of the space debris object. These new transformed sigma points are used to predict the new mean (estimation of ϵ and δ) and covariance. The actual measurements of the ϵ and δ of the space debris object made by the observer will most likely be different from the predicted values. The predicted state estimation and covariance are updated using the ϵ and δ measurements made by the observer, using Equations 4.20 and 4.21. This is repeated for all made observations.

5

Numerical methods

To test the performance of each constellation design different numerical methods need to be used. This chapter describes the numerical methods and where they will be used in the simulation. In Section 5.1 the numerical integrator will be discussed, in Section 5.2 the random number generator and in Section 5.3 the Nelder-Mead optimisation method.

5.1. Integrator

An integrator will be used to generate the orbits of both the space debris objects and the satellites, additionally the IOD method described in Chapter 4 also uses an integrator during its optimisation to generate candidate solutions.

The orbit of quite a few objects need to be propagated for at least a couple of days and with a time step between 1 second and a couple of minutes, therefore, a computationally fast integrator should be used to decrease the computation time. Furthermore, the satellites have a constant sampling size for the optical measurements, the position of both the satellites and space debris object thus needs to be known at each regular spaced time step. Using a variable time step integrator would require the use of an interpolator, which is less computationally efficient and introduces additional errors.

The Runge-Kutta 4 (RK4) integrator is a computationally efficient fixed step size integrator, which has also been shown to provide good accuracies for the long-term integration of the orbit of GEO based satellites (Lee et al., 1997). Therefore, an RK4 integrator will be used for the integration.

The RK4 integrator uses for function evaluations and works as follows (Lambert, 1991):

$$\mathbf{x}_{i+1} = \mathbf{x}_i + \frac{1}{6}h(k_1 + 2k_2 + 2k_3 + k_4) \quad (5.1)$$

$$t_{i+1} = t_i + h \quad (5.2)$$

with:

$$\begin{aligned} k_1 &= f(t_i, y_i) \\ k_2 &= f\left(t_i + \frac{h}{2}, y_i + h\frac{k_1}{2}\right) \\ k_3 &= f\left(t_i + \frac{h}{2}, y_i + h\frac{k_2}{2}\right) \\ k_4 &= f(t_i + h, y_i + hk_3) \end{aligned} \quad (5.3)$$

where h is the fixed step size, which will be chosen to be equal to the sampling rate of the optical observations.

5.2. Pseudo Random number generator

For the space debris population, a random set of orbital elements will be chosen from the distribution of space debris, as explained in Chapter 3. A computer is not actually able to select a truly random number, so instead different algorithms are used to create so-called Pseudo-Random numbers. In order for the simulations using pseudo random numbers to be reproducible a seed is used, which makes sure that sequences are fixed between different runs. As the software will be written in Python,

the used Pseudo-Random number generator will be the Mersenne Twister. This algorithm is very well tested and broadly used. For a extensive explanation of this algorithm see (Matsumoto and Nishimura, 1998).

5.3. Simplex Nelder-Mead optimisation

As mentioned in Chapter 4 the Nelder-Mead optimisation method will be used to minimise the cost function for the IOD method. The Nelder-mead method is a direct search method used for multidimensional unconstrained optimisation without using derivatives. This method is chosen, instead of for example a univariate or grid search method, for its robustness when dealing with non-linear and discontinuous solution spaces, its low computational cost and its suitability for parameter estimation when the function values are subject to noise (Gao and Han, 2012).

The simplex Nelder-Mead optimisation works as follows (Nelder and Mead, 1965). The method is first initialised by determining the fitness value for $n+1$ (in this case $n = 6$) points, these seven points form the initial simplex. A simplex is a geometrical shape, it is the n -dimensional version of a triangle, so for one dimension it is a line, for two dimensions it is a triangle and for three dimensions it is a tetrahedron. The vertices are ordered from best to worst (lowest fitness function to highest). The method changes the variables such that the simplex moves towards the minimum function minimum, the way in which the simplex moves is determined using the following algorithm. First the centroid, \bar{x} , of the simplex is calculated, the centroid is the centre of each point in the simplex except for the worst point:

$$\bar{x} = \frac{\sum_{i=1}^n x_i}{n} \quad (5.4)$$

The parameters of the worst point are then changed using the centroid. First the parameters are reflected in the following way, see Figure 5.1:

$$x_r = \bar{x} + \alpha(\bar{x} - x_{worst}) \quad (5.5)$$

where α is the reflection coefficient, if the reflected point has a lower fitness value than another point in the simplex except for the best point, a new simplex can be formed and the next iteration can be done. If the x_r has a lower fitness value than the best point in the simplex, x_r is expanded even further in the direction of the earlier reflection, see Figure 5.1:

$$x_e = x_r + \gamma(x_r - \bar{x}) \quad (5.6)$$

where γ is the expansion coefficient. If x_e results in a better fitness value than x_r , a new simplex is formed by replacing x_{worst} with x_e , the simplex has then moved to the minimum and a new iteration can be done. However, if the reflected point was worse than its initial value, a contraction is tried, see Figure 5.1. There are two types of contraction, inside and outside contraction, inside contraction is used when the x_r is worse than the original value:

$$x_c = \bar{x} + \beta(x_{worst} - \bar{x}) \quad (5.7)$$

where β is the contraction coefficient, if x_c is better than the original point, a new simplex is formed and a new iteration is started. Outside contraction is used when x_r is better than the original value but is worse than the second worst point:

$$x_c = \bar{x} + \beta(x_r + \bar{x}) \quad (5.8)$$

If x_c is better than x_r a new simplex is formed and a new iteration can be done. If both inside and outside contraction do not result in a new simplex a lest operation is performed, shrinking, this is mostly a fail-safe and is rarely used:

$$x_{point}^* = x_{best} + \delta(x_{point \neq best} - x_{best}) \quad (5.9)$$

The Nelder-Mead stops when either the maximum number of iterations has been reached or when the simplex has converged. The convergence is reached when:

$$\sigma < \text{tol} \quad (5.10)$$

$$\sigma = 2 * \left(\frac{f(x_{worst}) - f(x_{best})}{f(x_{worst}) + f(x_{best}) + \text{tol}} \right) \quad (5.11)$$

For the IOD method, these simplexes would be generated in a six dimensional space, where each axis represents one of the six elements of the state vector, so there would be an x -axis, y -axis, vx -axis etc. The location of the seven vertices that make up the initial simplex would then be determined by the seven state vectors that resulted in the lowest cost function. The simplex will then be transformed by changing the location of the worst performing vertex (state vector) using the algorithm explained earlier. There will then be a new worst vertex, which is then again transformed, this shrinks the simplex. This goes on until the simplex has converged or the maximum number of iterations has been reached. The estimated state vector is then the mean value of the seven vertices (state vectors) that form the final simplex.

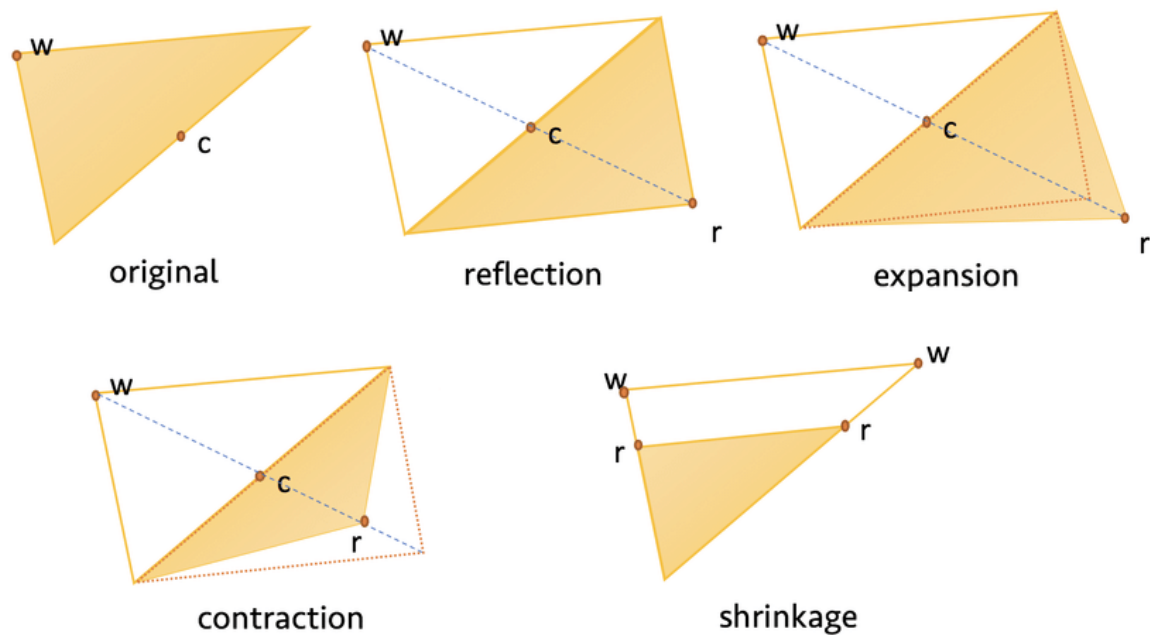


Figure 5.1: Nelder-Mead optimisation (Jiang et al., 2019)

6

Software

In this chapter the software needed to perform the design and simulation of the system. All the code will be written in Python, due to its easy use compared to other languages such as C++. This chapter is separated into three sections. In Section 6.1 external software packages that will be used for the simulation will be discussed, in Section 6.2 the software architecture will be described. Finally, in Section 6.3 the validation and verification of the software will be discussed.

6.1. External Software

If all the individual software blocks in the architectural design would have had to be coded, the seven month period designated for the thesis would have never been enough. Luckily, use can be made of external software. In this section the external software packages that will be used for the simulation will be discussed. The rest of the software blocks will have to be coded from scratch.

6.1.1. Tudat

The TU Delft Astrodynamics Toolbox, Tudat, contains several useful libraries for the propagation of orbital dynamics, written in both Python and C++. Tudat is developed and updated by students and staff of the Aerospace Engineering Faculty of the TU Delft. For this simulation Tudat will be used for the orbital dynamic propagation of the space debris population and the satellites. Tudat will be used because it allows for a lot of freedom in the set-up of the simulations, is relatively fast and can be easily combined with the other code written in Python. The, in Chapter 3 mentioned, environment models can be automatically generated by Tudat. Furthermore, Tudat also offers a wide range of propagation and integration methods, which also include the RK4 integration method as well as the propagation using the Modified Equinoctial Elements ¹. The ephemerides database, along with properties of bodies in the solar system, that will be used will be provided by SPICE ephemerides files. These ephemerides files are provided by NASA ² and can be easily loaded into Tudat.

All libraries and features present in Tudat have their own built-in unit test. All these unit tests can be run to verify the functions in Tudat. These individual functions can be considered verified if these unit tests are successfully run, no additional verification and validation tests have to be run.

6.1.2. NumPy and SciPy

NumPy and SciPy are both free open source libraries, which are commonly used in engineering based software. SciPy ³ mostly contains modules for mathematical operations such as, integration, ordinary differential equation solvers and interpolation. While NumPy ⁴ is mainly used for matrix related computations such as matrix multiplication or inversion. Both NumPy and SciPy come with built-in unit tests.

¹<http://tudat.tudelft.nl/index.html>: date accessed:6/1/2023

²<https://naif.jpl.nasa.gov/naif/index.html>: date accessed:6/1/2023

³<https://www.scipy.org/>: date accessed:6/1/2023

⁴<https://numpy.org>: date accessed:6/1/2023

6.2. Architectural Design

The architectural design diagram will give an overview of how all software blocks are connected and which inputs and outputs are needed for each block. In the diagrams, the square blocks are the input and or outputs of the software functions (round blocks), the arrows signify the data-streams of the in and outputs in to or out of the software functions. An overview of the whole architectural design can be seen in Figures 6.1. The architectural design can be split up into four different sub-modules. Each run starts with the initial state sub-module which generates the initial states of all space debris objects and satellites, according to provided statistical distribution of space debris and constellation design parameters. The generated initial states are then used as an input for the orbit propagation modules, which provides the full state history of space debris objects and satellites. The observation sub-module uses these state histories to generate all possible measurement vectors that the observing satellites could have made of each space debris object. If enough measurement vectors have been made for a space debris object, the measurement vectors will be used as an input for the orbit propagation sub-module, which will output a state estimation of for that particular space debris object. This state estimation is then compared to the propagated orbit of the space debris object to determine the accuracy of the orbit determination. The number and accuracy of the successful orbit determinations are then used to determine the relative performance of the constellation design. This whole process is repeated for each constellation design.

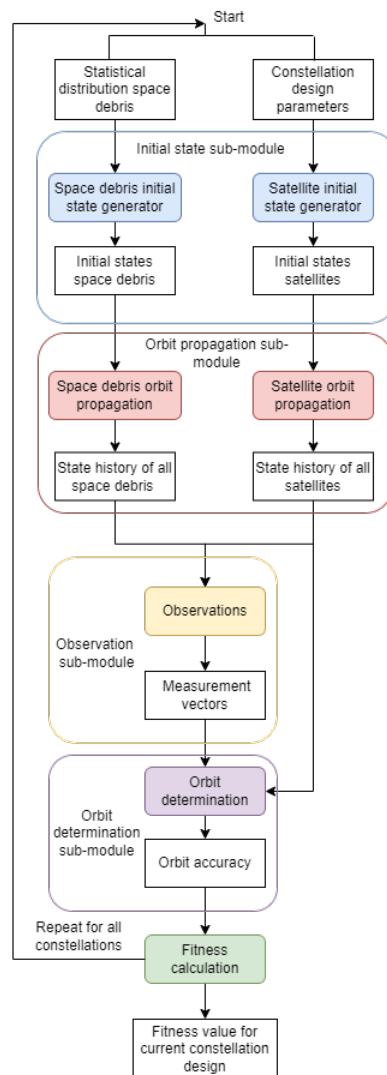


Figure 6.1: Software modules diagram

6.2.1. Initial state

The Initial state module is responsible for the initial states of all the objects for which the orbit will have to be propagated. The number of space debris objects and the statistical distribution of the space debris in GEO, see Chapter 3, are the inputs for the generation of initial states of the space debris objects. It uses these inputs to generate a space debris population with a similar Kepler element distribution as that of the inputs. For the initial states generation of the satellites, the constellation design parameters are used as the input. The output of this module are the initial states of each satellite and each space debris object, see Figure 6.2.

6.2.2. Orbital Propagation

The Orbital propagation module is responsible for providing the state vectors of each satellite and space debris object for each epoch. The module can be separated in to two different parts, the orbit propagation of the space debris and the orbit propagation of the satellites, see Figure 6.3.

The inputs for the orbit propagation of the space debris objects are the initial states generated by the Initial state module, the force model as defined in Chapter 3, the propagation method, simulation time, simulation time step, integrator settings, the tabulated ephemerides of the Earth, Sun, and Moon and the solar radiation parameters. The output are the full state histories in Cartesian coordinates for each space debris object, which are generated using the build-in dynamic simulator of the Tudat software package.

The inputs for the orbit propagation of the satellites are the simulation time, simulation time step, integrator settings and the initial states generated by the initial state module. It then uses a simplified dynamic model to generate the Kepler orbit for each satellite. The outputs of this module are the full state histories in Cartesian coordinates for each satellite.

6.2.3. Observation

The Observation module is responsible for providing observation vectors. The inputs for this module are the state vectors of the space debris and satellites, FOV angle, Sun position, space debris parameters, sensor parameters, background parameters, SNR threshold and measurements errors. The module first checks whether or not the space debris objects lies in the FOV of a satellite, this is done by projecting a pyramid shape from the observing satellite and checking if the space debris lies in this pyramid according to Equations 2.2-2.4. If the space debris object does not lie in the FOV of the satellite the procedure is repeated for a different epoch and/or space debris object. If the space debris object does lie in the FOV, the SNR is calculated by determining the amount of signal photons that reach the optical sensor according to Equations 2.11-2.15 and comparing this value to the amount of noise

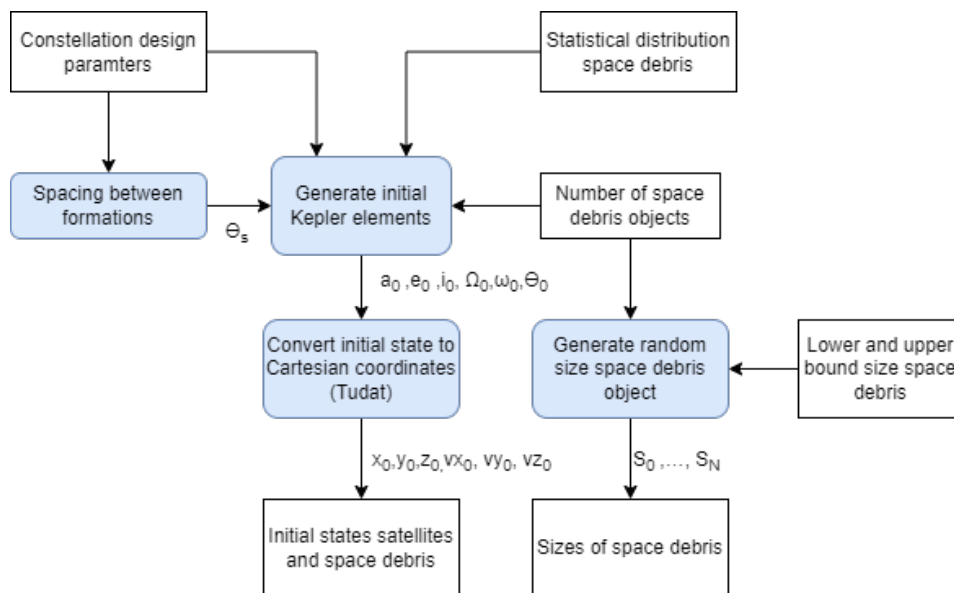


Figure 6.2: Initial state module diagram

State conversion

This function is built in by Tudat and thus was verified using the build in acceptance tests. It was also verified by comparing the results of the conversion to hand calculations.

6.3.2. Orbit propagation

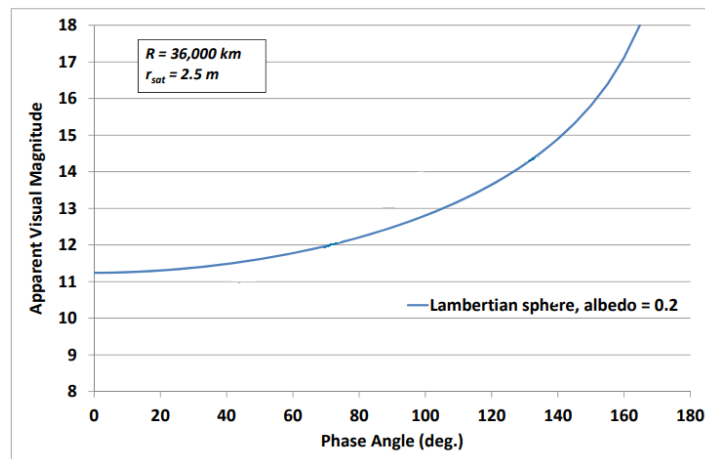
The external software Tudatpy is used for the entire orbit propagation module. Tudatpy has build in acceptance tests which are run during installation. All the acceptance tests were successful, thus the orbit propagation module is considered verified and validated.

6.3.3. Observations

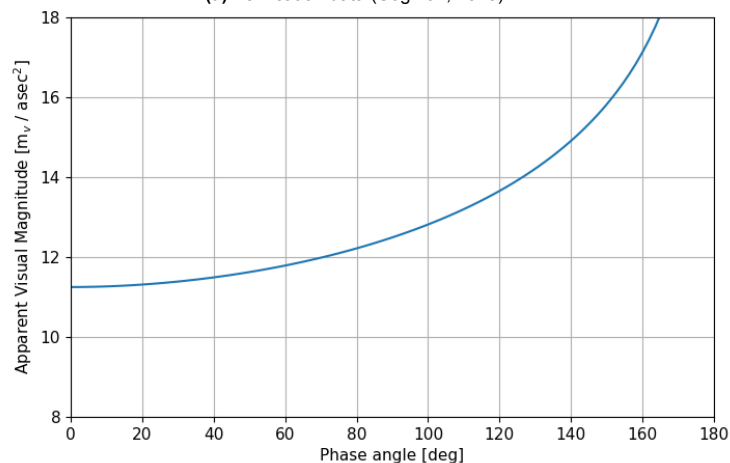
The first observation sub-module, the visual magnitude calculation, will be verified by comparing the results from the simulations to those reported by Congnion (2013). This paper was chosen, because it also uses real-life data of GEO-based satellites to validate its results. The paper provides the results for the following observation scenario:

- Distance between observer and satellite is 36,000 km
- The satellite is assumed to a diffuse Lambertian (ideal reflecting surface) sphere with a radius of 2.5 m and an diffuse albedo of 0.2.

The visual magnitude as a function of the phase angle for both the verification data and the simulation results are shown in Figures 6.6a and 6.6b. The results of the simulation match up perfectly with those reported in the paper and thus can be considered to be verified.



(a) Verification data (Cognion, 2013)



(b) Simulation results

Figure 6.6: Apparent magnitude of a Lambertian sphere, with albedo = 0.2 for different phase angles

The second observation sub-module that needs to be verified, is the SNR calculation. This sub-module will be verified by comparing the result to those reported by Tola (2015). In this paper the SNR is calculated for stars with different visual magnitudes and varying values of the sky background. The paper uses some slight differences between the methods used in the paper and those used in the code. First of all, the signal electrons received by the sensor is calculated in the following way

$$\varepsilon(m, T) = \Phi_i(m, T) \cdot \eta_T(\lambda_0, \lambda_1) \cdot \kappa_{optics} \cdot QE \cdot FF \cdot A \quad (6.1)$$

where k_{optics} is the optical lens transmittance, FF is the fill factor, in the method described in Chapter 2, these two values are represented by the total optical transmittance, τ . The photo irradiance for the star is calculated in the following way:

$$\Phi_i(m, T) = 7.37 \cdot 10^{14} \cdot \frac{10^{-0.4 \cdot m}}{T} \quad (6.2)$$

where m is the apparent magnitude of the star and T is the temperature of the star. The ratio of photons for the specific bandwidth of the sensor is calculated in the following way:

$$\eta_T(\lambda_0, \lambda_1) = \frac{1}{\Phi(T)} \int_{\lambda_0}^{\lambda_1} \phi_\lambda(T) d\lambda \quad (6.3)$$

where the total number of photons are calculated in the following way:

$$\Phi(T) = \alpha T^3 \quad (6.4)$$

where α is a constant ($\alpha = 1.52 \cdot 10^{15}$ [-]). The energy of a photon for a specific wavelength is determined as follows:

$$\phi_\lambda(T) = \frac{2\pi c}{\lambda^4 \left(e^{\frac{hc}{\lambda k T}} - 1 \right)} \quad (6.5)$$

where c is the speed of light ($c = 2.997 \cdot 10^8$ [m/s]), k is the Boltzmann's constant ($k = 1.38 \cdot 10^{-23}$ [JK⁻¹]), and h is Planck's constant ($h = 6.626 \cdot 10^{-34}$ [J/s]).

The paper uses the telescope parameters for their simulation, which can be seen in Table 6.1. The SNR as a function of apparent magnitude and background irradiance from the simulation and the paper can be seen in Figures 6.7a and 6.7b. Here it can be seen that as the apparent stellar magnitude increases (the brightness decreases) the SNR exponentially drops, there is also a clear drop in the SNR as the background brightness increases, which is expected since more noise signal reaches the optical sensor. For both the SNR as a function of apparent magnitude and background irradiance, the simulation results and the verification data match up perfectly, which indicates that the module works as intended and can be viewed as verified.

6.3.4. Orbit determination

The orbit determination module can be split up into two sub-modules, the initial orbit determination using the simplex fusion method and the precise orbit estimation method using the unscented Kalman filter, in this section these two methods will be verified.

Simplex Fusion

The initial orbit determination simplex fusion method will be verified by comparing it to the results provided by Handley and Hagerty (2020). This paper uses the following simulation settings, the states of

Table 6.1: Simulation parameters

Parameter	Value	Unit	Parameter	Value	Unit
Temperature Star	10000	K	k_{optics}	78.472	%
$[\lambda_0, \lambda_1]$	[400, 800]	nm	w	2048	pixels
FOV	4	deg	A	972	cm ²
FF	90	%	v_{slew}	1/240	deg/s
QE	50	%	σ_{ro}	30	e ⁻

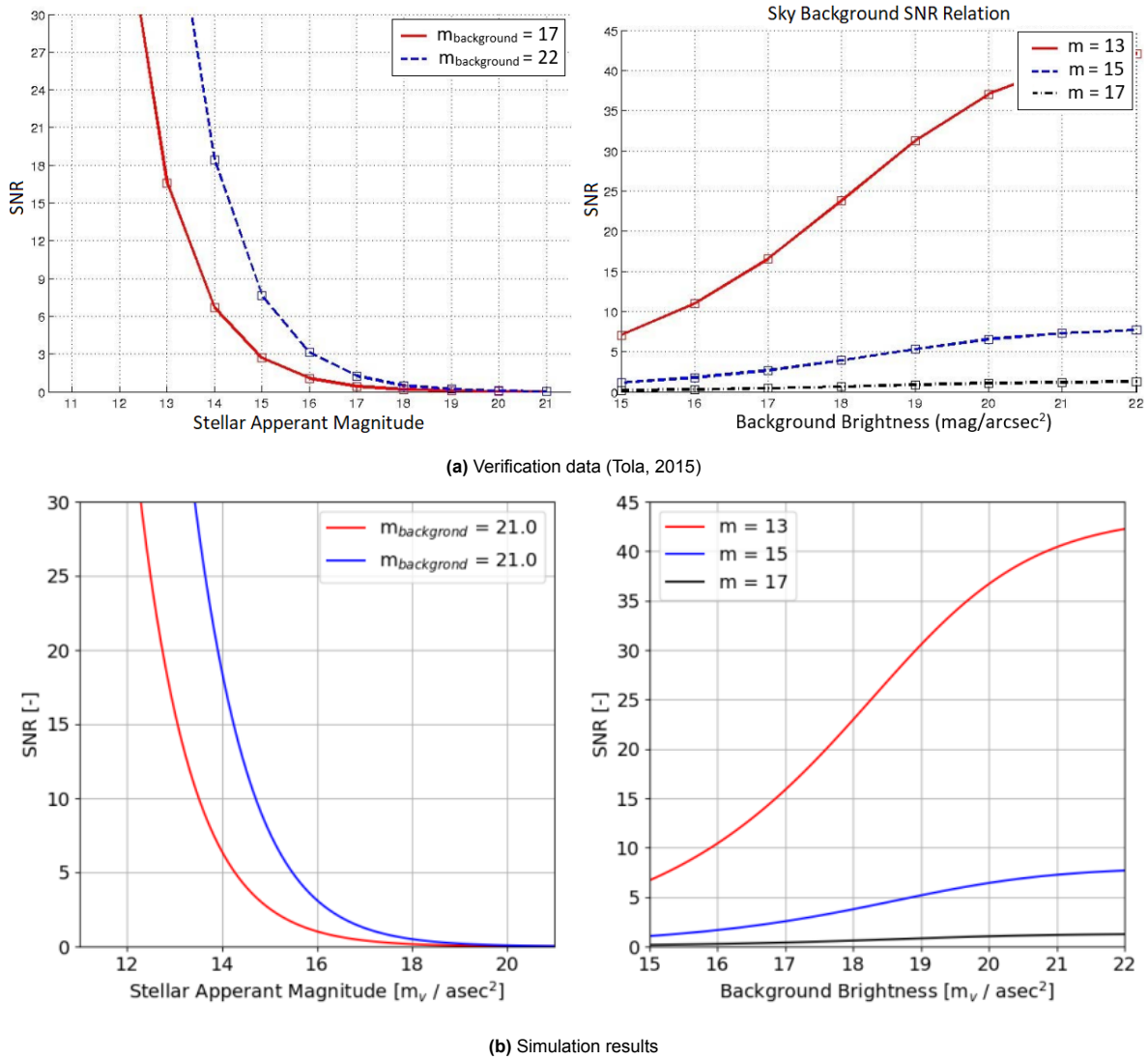


Figure 6.7: SNR as function of different stellar apparent magnitude (Left). SNR as a function of background brightness (Right).

3000 targets were propagated using an RK8(9) integrator, the maximum number of iterations is 2000, a tolerance of 10^{-12} , the initial state of these targets were randomly chosen using a Gaussian probability distribution using the values for the mean and standard deviation, $[\mu, \sigma]$, seen in Table 6.2:

Two observing satellites were simulated also using the same RK8(9) integrator, the initial states reported in Table 6.3 were used. The observations of these satellites were simulated with an interval of 300 seconds. Additionally, zero-mean Gaussian noise was added to the angle measurements in the same way as described in Chapter 2, the σ value of this noise was varied to determine the convergence rate of the method for different noise values. The paper reports a success rate of the initial orbit determination as function of the observation angle. This success rate is percentage of the targets for which a successfully initial orbit determination has been performed, in this paper an initial orbit determination is successful if the estimated semi-major and semi-minor axis are accurate to 1% of the true value and

Table 6.2: Mean and standard deviation values for target initial states

a [km]	e [-]	i [deg]	ω [deg]	Ω [deg]	Θ [deg]
[42164, 100]	[0, 0.001]	[0, 45]	[0, 180]	[0, 180]	[0, 180]

Table 6.3: Initial states of observing satellites

	a [km]	e [-]	i [deg]	ω [deg]	Ω [deg]	Θ [deg]
Satellite 1	42,164	0	10	0	0	20
Satellite 2	42,164	0	0	0	0	0

if the attitude error is lower than 1 degree. The attitude error is calculated in the following way:

$$\Delta = \mathbf{C}_t \mathbf{C}_e^T \quad (6.6)$$

$$\theta_{error} = \cos^{-1}[(\text{tr}(\Delta) - 1)/2] \quad (6.7)$$

where \mathbf{C}_t and \mathbf{C}_e are the ECI \rightarrow LVLH rotation matrices for the true and estimated states respectively.

There are two notable differences between the simulation reported in the paper and the simulation performed for the verification. First of all, for the propagation of the state vectors of the satellites and targets a fixed step size RK4 was used instead of a variable step size RK8(9) used in the paper. Since the propagation of the candidate solutions is also performed using an RK4 integrator, it is expected that the success rate of the verification simulations are higher than those reported in the paper.

The paper does not describe the method it used to generate the full state vector from the candidate position vector, it only mentions that it assumes a circular orbit. At first, it was assumed that the velocity in the z-direction was zero, such that a perpendicular vector could be generated counterclockwise to the xy-position vector and using the orbital velocity corresponding to the semi-major axis of the target. However, using a zero z-velocity for all candidate solutions prevented the optimiser to converge. Therefore, a random z-velocity was added to each candidate state vector, with a mean of zero and a standard deviation of 100 m/s. It is unknown, how this issue is handled in the paper, so this could lead to differences between the verification data and the results. However, this most likely only results in a difference of convergence speed, since almost all successful initial orbit determinations needed far less iterations than the maximum of 2000.

In Figure 6.8 the results of the verification of the simplex fusion can be seen. The success rate of the simulations is always slightly higher (1-4%) than those reported in the paper. The cause of this is most likely the fact that the simulation uses the same integrator as that used for the propagation of the candidate state vector, while the paper uses a more precise integrator for the propagation of the targets and observing satellites.

To check whether this is the case, the simulations were repeated again using an RK4 integrator for the orbit propagation, however, instead of comparing the results to the verification data, a second simulation was run where the orbit was propagated using a variable step size RK7(8) integrator (an RK8(9) integrator is not available in Tudat). For the propagation of the candidate solution an RK4 integrator was again used for both the simulations. Since everything is exactly the same for the two simulations expect the integrator, the difference in the success rate should be similar to the difference in success rate for the original simulation and the verification data. This is confirmed by looking at Figure 6.9, where it can be seen that the differences in the success rate are very similar for the simulation using the RK7(8) integrator and the verification data using the RK8(9) integrator. The small differences could be explained by the fact that there is a difference in the accuracy of the RK7(8) and RK8(9) integrator and the fact that it is not known how the z-velocity is calculated for the verification data.

UKF

The UKF will be verified in two steps, first a simple 1d linear problem is used to check if the UKF works properly. Secondly, a more representative model is used to fully verify the UKF. The following 1d dynamics have been used:

$$\begin{pmatrix} x_i \\ y_i \end{pmatrix} = \begin{bmatrix} 1 & dt \\ 0 & 1 \end{bmatrix} \begin{pmatrix} x_{i-1} \\ y_{i-1} \end{pmatrix} \quad (6.8)$$

the system is initialised in the following way:

$$\begin{pmatrix} x_i \\ y_i \end{pmatrix} = \begin{pmatrix} 1 \\ 2 \end{pmatrix} \quad \mathbf{P}_0 = \begin{bmatrix} 1 & 1.1 \\ 1.1 & 3 \end{bmatrix} \\ \mathbf{R}_0 = [0.0065] \quad \mathbf{Q}_0 = \begin{bmatrix} 0 & 0 \\ 0 & 0.001 \end{bmatrix} \quad (6.9)$$

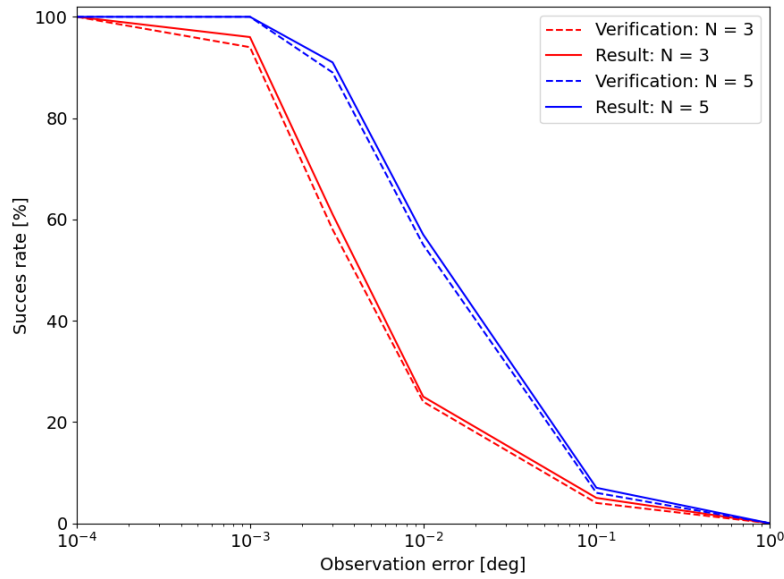


Figure 6.8: Success rate of Simplex fusion as a function of the observation error for N observations

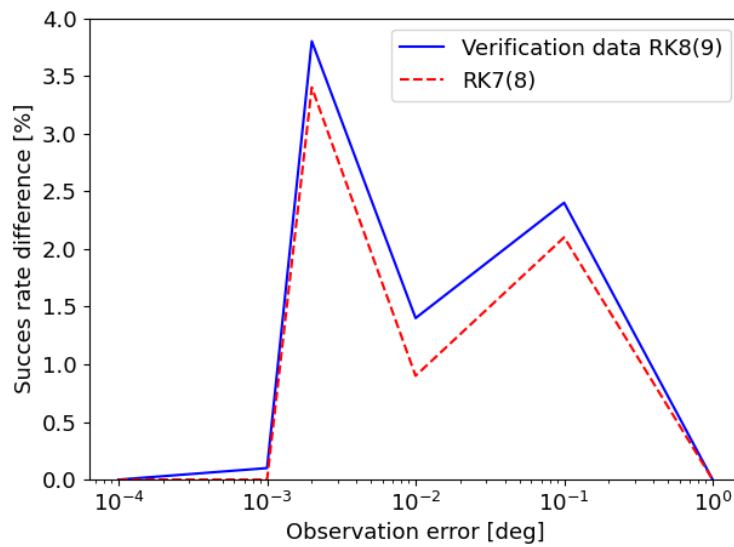


Figure 6.9: Difference in success rate as a function of the observation error for five observations

The observations are generated by adding an error to the x position from a normal distribution ($\sigma = 0.1$). The results can be seen in Figure 6.10, the filter converges quickly in around 20 seconds, the estimation error of 0.16 m oscillates between the 3- σ bounds which indicates that the UKF works properly for this simple 1d problem.

The above mentioned model is very simple and very different from the dynamics and observation model that will be used in the simulations. Therefore, the UKF will be verified using a more similar problem. Felicetti and Emami (2016) report the performance of a UKF which has been used to estimate the orbit of highly inclined space debris in LEO using the observations of an observing satellite in a polar orbit, see Table 6.4. These simulations settings were used to generate line of sight measurements, this was done using a simulation time of one hour and a time step of one second. The UKF was initialised using the values below:

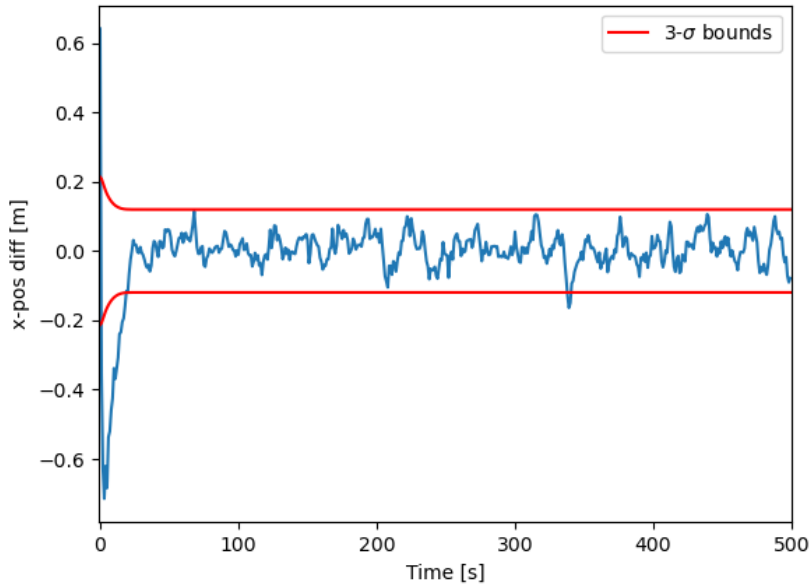


Figure 6.10: x-position error as a function of time

Table 6.4: Simulation settings

	Observing satellite	Space debris	Unit
Number	4	200	[-]
Semi-major axis	7171	6900-7300	[km]
Inclination	98.2	53-113	[deg]

$$\begin{pmatrix} \mathbf{x}_0 \\ \mathbf{v}_0 \end{pmatrix} = \begin{pmatrix} \mathbf{x} + 10,000 \\ \mathbf{v} + 100 \end{pmatrix} \quad \mathbf{P}_0 = \begin{bmatrix} 10,000^2 \mathbf{I}_{3 \times 3} & 0 \\ 0 & 100^2 \mathbf{I}_{3 \times 3} \end{bmatrix} \quad (6.10)$$

$$\mathbf{R}_0 = (5'')^2 \mathbf{I}_{3n \times 3n} \quad \mathbf{Q}_0 = \begin{bmatrix} 0 & 0 \\ 0 & 0.0001^2 \mathbf{E}_{3 \times 3} \end{bmatrix}$$

Since the initial states of both the space debris and satellites are randomly chosen within the bounds, it is impossible to recreate the exact observations scenarios, for which the results are provided in the paper. The paper does mention that for an ideal observation scenario, where all four satellites can make measurements at the same time, the UKF converges quickly to an accuracy of $3\text{-}\sigma = 6$ m. To replicate this result, an object and time interval of at least 10 minutes was chosen where the object was observable by all satellites. The results of this simulation can be seen in Figure 6.11, it can be seen in the figure that it is similar to the results of Felicetti and Emami (2016), the filter converges quickly and does this to around an accuracy of $3\text{-}\sigma = 8$ m. The small difference between accuracies of 2 meters could be caused by the two following things. First of all, it is not reported in the paper how the measurement error is applied to each measurement, this could be different from the method mentioned in Chapter 2, which could lead to a difference in measurement vectors and thus a difference in the maximum achievable estimation accuracy.

Secondly, the paper does not report the exact orbit of the space debris for which the estimation accuracy is given which corresponds to the ideal observation scenario. Thus it is likely that the orbits of the space debris are different. A smaller semi-major axis will lead to faster dynamics, which will effect the accuracy of the prediction step in the UKF. A difference in orbit is thus most likely the cause of the difference in estimation accuracy between the two models.

To check whether this was the case two different simulations were run. The effect of varying the observation error on the position error was investigated. It is expected that a varying observation error effects the position error and this can indeed be seen in Figure 6.12, were there , this confirms that a differently applied measurement error can indeed increase the estimation accuracy. However, this

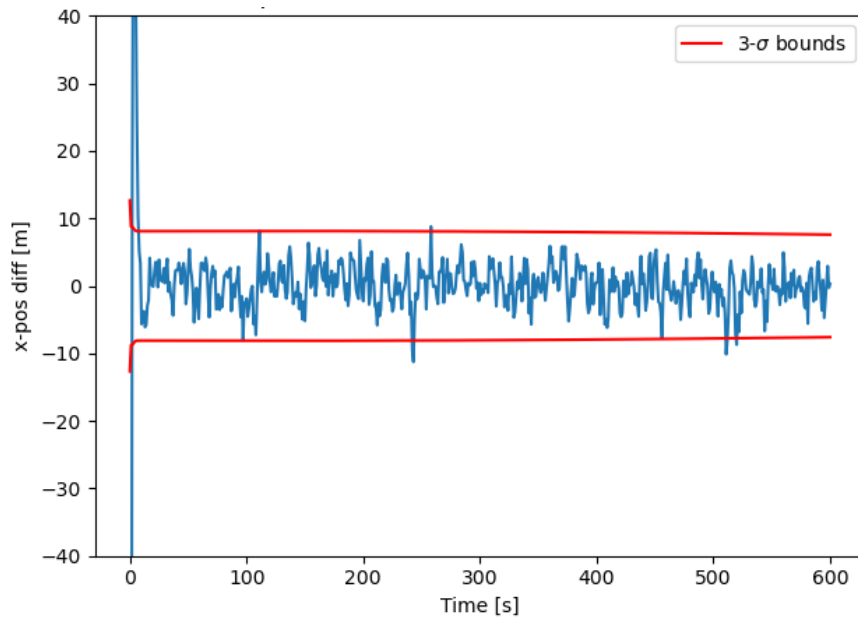


Figure 6.11: x-position error as a function of time

alone does not explain the accuracy difference of 2 m. The effect of changing the semi-major axis of the space debris objects on the position error was also looked into. In Figure 6.12, it can be seen that the position error decreases as the semi-major axis increases. The position error between the upper and lower bounds of the semi-major axis can be as large as 2.5 meters. The difference in observation error and semi-major axis of the space debris object can thus explain the estimation accuracy between the simulation and the verification data.

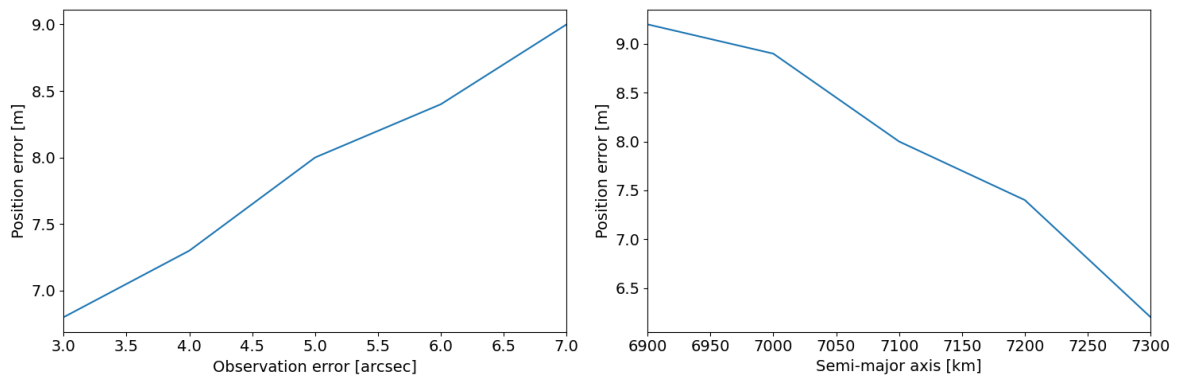


Figure 6.12: Difference in position error as a function of the observations error (left) and the semi-major axis of the observed space debris object (right)

7

Design space

In this chapter the design space in which the optimisation will take place will be discussed. This design space consists of all design variables that make up a constellation design and their lower and upper bounds between which the value can change. In the Section 7.1 of this chapter the design variables will be discussed, what is the effect of these variables on the performance of the constellation and what are their lower and upper bounds? In Section 7.2 a design space exploration is performed where the bounds are decreased to improve the speed and robustness of the optimisation. In Section 7.3 the UKF will be tuned using the design variables. Finally, in Section 7.3 the final lower and upper bounds for the design variables are given which will be used for the optimisation.

7.1. Design variables

There is a total of six design variables that make up the full constellation design, the sensor size, focal length, semi-major axis, inclination, number of satellites per group and the total number of satellites in the whole constellation. In this section their effect on the performance of the constellations is discussed as well as the initial upper and lower bounds.

Sensor size

The CCD sensor size, A_{sensor} , is the area of the CCD sensor which actively converts the incoming photons into a electrical signal. A larger sensor will be able to receive more individual photons at the same time and will provide a higher resolution, this increases the SNR for an object. However, a larger sensor will also lead to a larger FOV angle (when using the same focal length), which will have a negative effect on the SNR for an object. The bounds for the sensor size were determined by looking at the state of the art CCD sensors that are currently available. Most CCD sensors used in NASA and ESA missions are produced by the same company, Teledyne, so the bounds for the sensor size will be determined by looking at their smallest and largest sensor size's available, designed for space-based observations. From their website ¹, the smallest possible sensor size is 10 x 10 mm and the largest is 82 x 82 mm. These will be the initial bounds used for the simulations.

The sensor size is determined by two factors, the pixel size, p and the amount of pixels per row of the sensor, w . As can be seen in Chapter 2, the pixel size and number of pixels per row both have an effect on the SNR calculation. From the Teledyne website, it can be seen the the lower and upper size limit for the pixel size is 10 μm and 50 μm . To determine which combination of pixel size and number of pixels gives the best performance for this observation scenario, simulations where run. For different observations (varying; distance between satellite and object, focal ratio's, and FOV angles) the SNR was calculated for different combinations of pixel sizes and number of pixels per row. In Figure 7.1, the results of this optimisation can be seen. It is clear that the performance of the optical system is higher when the pixel size is as small as possible and the number of pixels is as large as possible. Thus, for the following simulations, the smallest pixel size will be used, 10 μm , and the number of pixels per row then follows from the sensor size.

¹<https://www.teledyneimaging.com/en/aerospace-and-defense/applications/space-astronomy-space-science/>

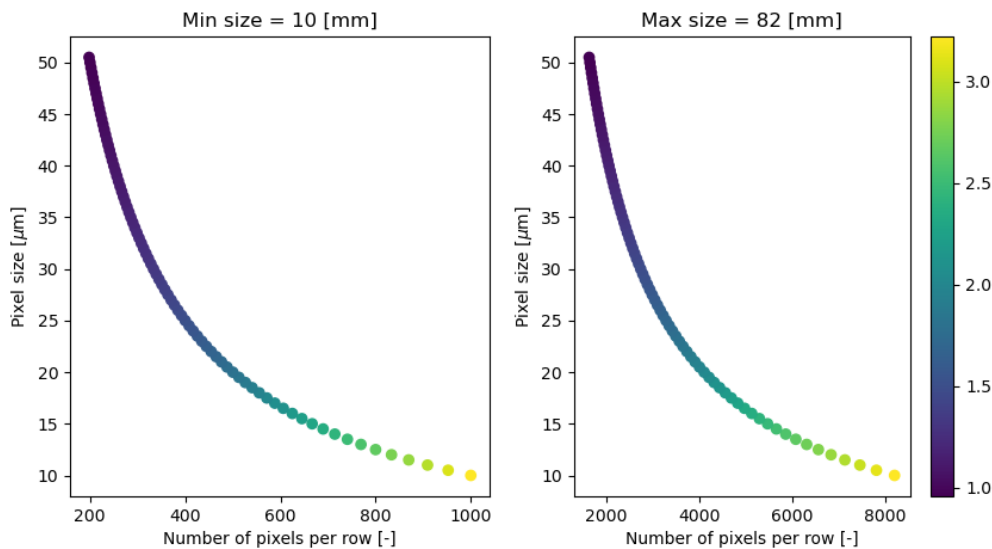


Figure 7.1: SNR for as a function of pixel size and number of pixels per row

Focal length

The focal length of the optical telescope is the distance between the aperture of the sensor and the CCD sensor. The focal length has a large effect on the performance and the design of the different constellations. This is because of two reasons. First of all, the larger the focal length the larger the satellite will have to be to house the telescope, the focal length should thus be as small as possible. Secondly, the focal length is proportional to the field of view of the telescope. A large focal length will allow for a smaller field of view and as could be seen in Chapter 2, this will lead to a higher SNR, which will increase the conversion rate of space debris objects that pass through the field of view to actual observations. However, a smaller FOV also leads to less space debris objects crossing that FOV, which will limit the possible observations. There are no clear definitive lower or upper bound limitations for the focal length. The focal length could theoretically be a couple of meters, however, this would result in a very large and expensive satellite. On the other hand, the focal length could also be very small, but this would mean that the distance between satellite and space debris would also have to be very small, which would severely limit the number of observations. Since there is no clear definitive lower and upper bound for the focal length, an initial lower and upper bound for the design-space exploration have been chosen to be, 0.05 and 1.0 m, respectively, however if the system shows good performance close to the lower and upper bound they will be changed.

Semi-major axis

The semi-major axis of the satellites will have a large effect on the performance of the constellation. A small semi-major axis will increase the distance between the satellite and the space debris objects, this has two advantages. Firstly, the region of the GEO that it can observe using the same FOV angle is larger the further away the satellite is from GEO, this will lead to more space debris objects crossing the FOV of the satellite and thus more potential observations. Secondly, the relative velocity of the satellite with respect to the space debris objects is larger when the semi-major is smaller, this will lead to more potential observations of unique space debris objects for the same time period as a larger semi-major axis, additionally, each object will be observed more regularly.

A larger semi-major axis also has two major advantages compared to a smaller one. The distance between satellite and space debris object will be smaller, thus more light from the object will reach the optical sensor, which will increase the SNR of the objects, so more potential observations will be converted to actual observations. Secondly, the smaller relative velocity between satellite and object will lead to more consecutive observations which will in turn result in a higher accuracy of the orbit estimations.

To determine the lower bound for the semi major axis, the largest possible distance between the satellite and space debris object in GEO is calculated for which an object with a diameter of 10 cm is

visible for the largest possible telescope (focal length 1.0 m). Figure 7.2 shows that the SNR increases as the semi-major axis increases and that the slope also increases as the semi-major becomes higher. At 13,750 km the line crosses the SNR threshold of 2.5, thus this semi-major axis will be used as the lower bound. The upper bound of the semi-major axis is equal to the lower bound GEO region which in this case is 41,000 km.

Inclination

The inclination of the observing satellites can have two different effects on the performance of the constellation. First of all, satellites in orbits with varying inclinations, will be able to observe a slightly different GEO region than other satellites. If many space debris objects are located in this particular GEO region, this could lead to an increase in space debris objects. Furthermore, when satellites in the same group have different inclinations, the measurement vectors that each satellite will make for a specific space debris object will vary more, than when all satellites have the same inclination. This could benefit the accuracy of the IOD and UKF, especially when the observed space debris object are in a co-planar orbit with one or more of the satellites (Hippelheuser, 2021).

The lower and upper bounds of the satellite inclination are determined by the GEO region that will be investigated. Having an inclination higher than that of the space debris objects will not be beneficial, the satellite would then also start to observe parts of space where no space debris objects could ever be observed. The lower and upper bounds of the satellite inclination will be the same as those for the space debris objects, thus ± 15 degrees.

Number of satellites per group

The constellation will most likely consist of multiple groups of satellites that orbit closely to each other. A high number of satellites per group will lead to observations from multiple points of view of the same space debris object at a certain time. This will improve the accuracy of the IOD and UKF and make it less susceptible for measurement errors. A smaller number of satellites per group will make it possible to observe more of the GEO region using the same amount of total satellites, which will lead to more observations of unique space debris objects.

For the 3D positioning using GPS satellites at least four satellites are needed, however, these satellites make range observations, while for this constellation only line of sight vectors are measured. In theory, the line of sight measurements of only two satellites are needed to determine the position of an object in 3D space. However, due to the measurement errors that effect each measurement, using more satellites will lead to a more precise orbit estimation, however after a certain number of satellites, the accuracy improvement does not improve significantly. Therefore, the lower and upper bound for the number of satellites per group are two and five, respectively.

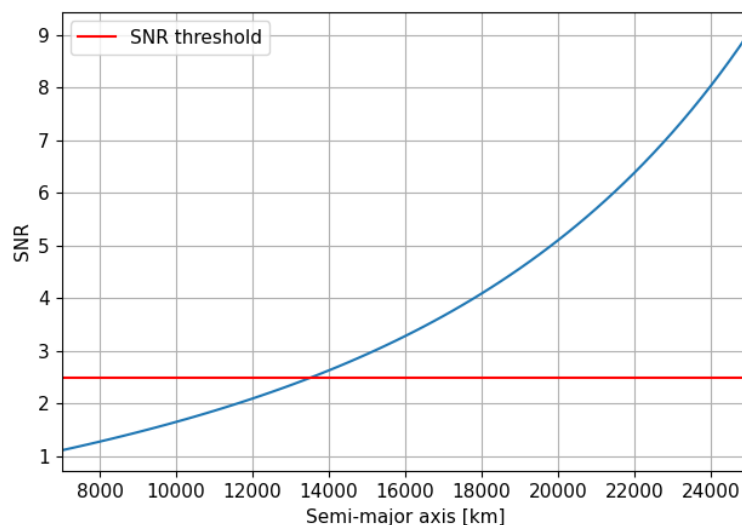


Figure 7.2: SNR as function of semi-major axis of the observing satellite (SNR threshold = 2.5)

Number of total satellites

A larger number of total satellites will always lead to a better performance of the whole constellation, it will lead to more observations as well as more simultaneous observations of the same space debris object, which will improve the orbit determination accuracy. However, using more satellites will increase the cost of the constellation and thus should be kept as small as possible. For this optimisation a maximum of 16 total satellites has been chosen as the upper limit. The lower limit is two, since at least two satellites are needed per group to get an accurate orbit estimation. All upper and lower bounds for each design variable discussed in this section are summarised in Table 7.1.

7.2. Design space exploration

The computational cost to determine the performance of the different constellation designs are quite high ranging from five minutes to more than one hour depending on the amount of satellites in the constellation. The current bounds for design variables as described in the previous section are too broad at the moment, either a very long simulation time is needed (1-2 weeks) or the interval between possible values for a design variable need to be large, such that there is a limited number of combinations tested, however, this will likely not result in the actual best constellation design. Therefore, a design-space exploration is needed, this will hopefully result in decreasing the bounds of the design variables and perhaps give some additional insight in the effect of the different variables on the performance. To determine the bounds for each design variable, separate simulations will be run for all design variables. This way the true lower and upper bounds for a single design variable can be determined without having to take interactions between design variable into account.

Sensor size

To further narrow down the bounds of the sensor size, the SNR for different FOV angles and sensor sizes are simulated. The simulations were run using the simulation settings in Table 7.2, however, the overall trends and conclusions that can be seen/made from the results are the same for all observation scenarios.

The results of these simulation can be seen in Figure 7.3. Here the SNR is shown for different combinations of sensor size and FOV angles, additionally the figure also shows the corresponding focal lengths that result from particular sensor size and FOV angle combinations. As could be expected the lower FOV angles lead to higher SNRs for the same sensor size. One surprising trend can be seen in Figure 7.3 is the fact that the SNR is constant for the same focal ratio and is thus not dependent on the sensor size. A larger sensor, for the same focal length, leads to a larger FOV, which in turn leads to more possible observations. Since the SNR is independent from the sensor size, it is always preferable to use the largest possible sensor and thus largest FOV. Therefore, for the rest of the simulations, a sensor size of 82x82 mm will be used.

Table 7.1: Initial design variables

	Lower bound	Upper bound	Unit
A_{sensor}	10 x 10	82 x 82	[mm]
L_f	0.05	1.0	[m]
a_{sat}	13,750	41,000	[km]
i_{sat}	0	± 15	[deg]
$N_{formation}$	2	5	[-]
N_{total}	2	16	[-]

Table 7.2: Simulation settings

	Observing satellite	Space debris	Unit
Semi-major axis	35,000	42,167	[km]
Inclination	0	0	[deg]
Theta	0	0	[deg]
Phase angle	0	0	[deg]

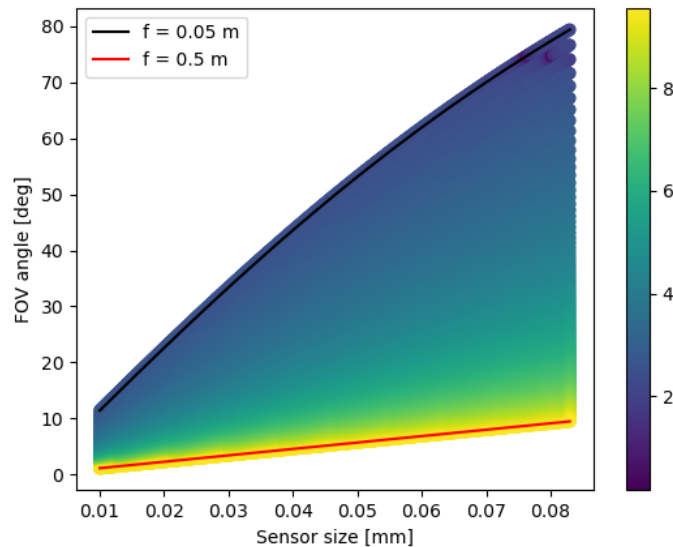


Figure 7.3: SNR for different FOV angles and sensor size

Focal length & semi-major axis

To narrow down the bounds of the focal length and semi-major axis, it was investigated what percentage of space debris objects the satellite could observe. The overall performance of a constellation design is very dependent on the amount of space debris objects it can observe in a certain time period. If certain values of focal length and semi-major axis results in significantly lower performance than others, these focal length and semi-major axis will then be excluded from further investigation.

The results of these simulations are shown in Figure 7.4a. At the higher bound of the semi-major axis the percentage is very low, however, when looking at Figure 7.4b, it can be seen that almost all objects in its FOV have a SNR higher than the threshold. The very low percentage is thus caused due to a lack of space debris objects that cross the FOV of the satellite. The opposite effect can be observed near the lower bounds of the semi major axis, where only a very limited amount of space debris objects have a SNR higher than the threshold, however, due to the large number of space debris objects that cross the FOV of the sensor, there is still a significant percentage of space debris objects observed.

In Figure 7.4b, it can be seen that a higher focal length leads to more objects with a SNR higher than the set threshold, which could be expected since the a higher focal length leads to a smaller FOV, which in turn leads to a higher SNR. However, when looking at Figure 7.4a, there is no significant relation between the focal length and the percentage of space debris objects observed. This is again caused by the fact the a larger focal length leads to a smaller FOV, which means that the satellite can observe only a small amount of space debris objects. So the performance for constellations with large semi-major axis and focal length, are limited by the amount of space debris objects that crosses the FOV, while for the smaller semi-major axis and focal lengths, the performance is limited by the SNR of the objects.

In Figure 7.4a, a triangular region is marked, this region contains all combinations of focal length and semi-major axis that result in at least a 35% observation performance, and perform significantly better than the combinations outside of this region. The upper and lower bounds for the semi-major axis bounds will now be 20,000 km and 36,000 km, respectively. The upper and lower bounds for the focal length bounds will now be 0.1 m and 1.0 m respectively.

Inclination

To try and narrow down the bounds of the inclination of the satellites the performance of constellation designs using different delta inclinations. To asses the performance of each constellation design two metrics were used, the average number of observations and the average position error per constellation design. Two different types of constellation designs were tested, for which multiple different simulations where run for each type. The first type of constellation uses co-planar orbits in this case all satellites will have an inclination of 0 degrees and a spacing between them of 2 degrees. The second type of

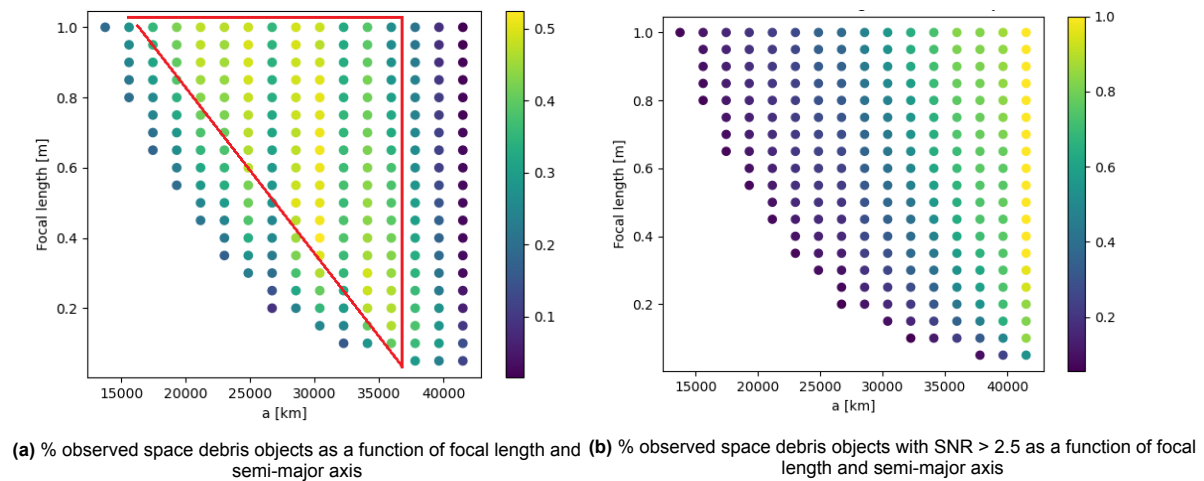


Figure 7.4: Focal length and semi-major axis design exploration

constellation uses different inclinations for each satellite of the group, one constellation will have a difference of inclination of 5 degrees ($i_1 = -5^\circ, i_2 = 0^\circ, i_3 = 5^\circ$), the other constellation will have a difference of inclination of 15 degrees ($i_1 = -15^\circ, i_2 = 0^\circ, i_3 = 15^\circ$). Using these two types of constellations gives insight into the effect of the inclination of a satellite on the number of observations as well as the effect of the difference in inclination between satellites in the same group on the accuracy of the orbit determination.

The results can be seen in Table 7.3. It can be seen that there is a smaller negative relation between the average number of observations and the difference in inclination of the satellites. There is also a clear difference in the average position error. When the satellites in a group are in co-planar orbits, the average position error is significantly worse than when different inclinations are used for each satellite in the group. As mentioned before, this is due to the fact that the measurement vectors are very similar, which decreases the observability of an object which in turn decreases the accuracy. So, no co-planar orbits will be used for satellites in the same group.

Satellites per formation

The number of satellites per formation will have an effect on the accuracy of the IOD and the subsequent UKF, to try and narrow down the initial design bounds the accuracy of the IOD will be compared between the different number of satellites per formation. For each number of satellites per formation, nine different constellation designs are simulated, varying in semi-major axis and inclination. The average position error for all these nine constellation designs is then calculated, the results can be seen in Table 7.4. As expected, the IOD method does not converge when only each formation consists of only one satellite, leading to very large position errors. The larger number of satellites per formation all result in relatively accurate orbit estimations. As expected, using a larger number of satellites will lead to a higher accuracy. However, using five instead of four satellites per group only improves the accuracy by 10 meters and this accuracy improvement is not significant enough to be worth the extra cost and decrease in total observations. Therefore, the lower and upper bounds for the number of satellites per formation will now be two and four respectively.

Table 7.3: Constellation performance for varying inclination differences

Δi	0	± 5	± 15
Average number of observations [-]	57	53	50
Average position error [km]	14.75	2.93	2.86

Table 7.4: Orbit determination accuracy for different numbers of satellites per formation

# satellites per formation	1	2	3	4	5
Average position error [km]	7.78e5	2.44	1.86	1.30	1.32

7.3. UKF tuning

The UKF needs to be initialised such that it converges and gives accurate orbit estimations for each of the different observations scenarios. For example, a difference in semi-major axis will increase the estimation uncertainty due to the relatively larger measurement error. Using the final design bound for the semi-major axis, the UKF can be tuned such that it will converge for the different possible observation scenarios. By trial and error the appropriate initialisation values were found for different observation scenarios, these data points were then used to determine the relation between the semi-major axis and the needed initialisation values. Two different metrics were used to determine if the initialisation values resulted in a well working UKF. First, it was checked whether or not the UKF had converged after the last measurement was made. Secondly, the estimation error of the UKF needed to oscillate between the $3\text{-}\sigma$ bounds. Since the orbit determination accuracy will be different for different constellation designs, no accuracy requirement was used in order to determine the performance of the UKF. The initialisation values were chosen such that it provided (close to) the maximum accuracy possible as long as it complied with the two metrics mentioned earlier. This resulted in the following initialisation values:

$$\mathbf{P}_0 = \begin{bmatrix} (750)^2 \mathbf{I}_{3 \times 3} & 0 \\ 0 & (5)^2 \mathbf{I}_{3 \times 3} \end{bmatrix} \quad (7.1)$$

$$\mathbf{R}_0 = \left(\left(\frac{-1.5}{12 \times 10^6} \times (a - 24 \times 10^6) + 4 \right) \cdot 4.84814 \times 10^{-6} \right) \mathbf{I}_{3n \times 3n}$$

$$\mathbf{Q}_0 = \begin{bmatrix} 0 & 0 \\ 0 & (0.4)^2 \mathbf{E}_{3 \times 3} \end{bmatrix}$$

where 4.84814×10^{-6} comes from the conversion of radians to arcseconds. As can be seen in Figure 7.5 these settings leads to a well-tuned UKF, the UKF converges and the error oscillates between the $3\text{-}\sigma$ bounds. It can also be seen that a larger semi-major axis leads to a lower estimation uncertainty, as explained previously, this is caused due to the relatively higher measurement error when the distance between space debris object and observer becomes larger.

Conclusions

Table 7.5 shows the final design variable bounds for the design variables that will be used for the optimisation of the constellation design. For the sensor size it was found that the best performance would always occur for the largest possible sensor size. The performance of the system was the best for semi-major axis values in the middle of the initial interval, so the lower and upper bound can be brought closer together. For the focal length all values from the initial range could provide adequate performance, however, the best performance was seen for focal lengths in the middle of the initial interval. An increase in the difference in inclination of the satellites had a positive effect on the accuracy of the orbit determination, however, it had a negative effect on the number of observations the system could make. The optimal value for the difference in inclination will thus dependent on which metric is deemed more important. Finally, the satellites per formation increased the average position accuracy of the orbit determinations, however, this was only up until four satellites, after which the accuracy increase was negligible. Using only one satellite per formation gave a very large position error and will therefore no longer be considered in the optimisation.

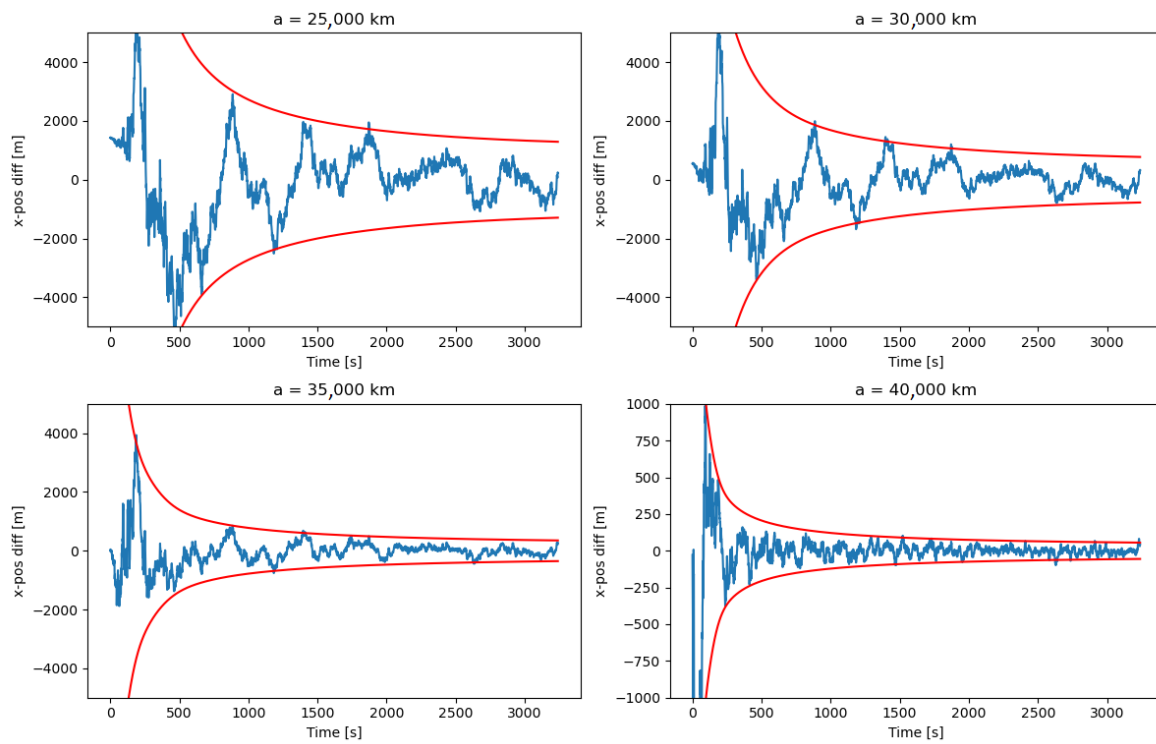
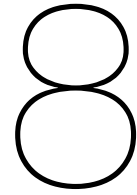


Figure 7.5: UKF performance for different semi-major axis: $a = 25,000; 30,000; 35,000; 40,000$ km

Table 7.5: Design variables

	Lower bound	Upper bound	Unit
A_{sensor}	82 x 82	82 x 82	[mm]
L_f	0.1	1.0	[m]
a_{sat}	20,000	36,000	[km]
i_{sat}	0	± 15	[deg]
$N_{formation}$	2	4	[-]
N_{total}	2	16	[-]



Design optimisation & analysis

To answer the main research question it is first important to find the (near) optimal constellation design. To find the optimal design different optimisation methods will be used. In Section 8.1 the results of initial optimisation using the Taguchi method is presented. Following that, in Section 8.2 the factorial optimisation method is used to find the optimal design. The performance of this optimal design is discussed in Section 8.3. The sensitivity of both the design process as well the performance of the optimal design will be looked at in Section 8.4. Finally, Section 8.5 will discuss the robustness of the design.

8.1. Taguchi method

The Taguchi method is a method developed to gather the most relevant data points in the least number of experiments possible. The method is used to design experiments to investigate the effect of different design parameters on the mean and variance of the performance metric of a system. Instead of testing all possible combinations of design variables, the Taguchi method tests pairs of combinations. This is done by using orthogonal arrays. The results of the experiments designed using the Taguchi method gives valuable insight into how (much) the different design variables influence the performance of a system, while using the the least amount of experiments necessary. The Taguchi method is best used when single runs of an experiment are computationally costly and when between three to 50 design variables are investigated (Taguchi, 1995). Since this is the case for the design space exploration the Taguchi method will be used.

The first step of the Taguchi method, is specifying the performance metric that needs to be optimised. This needs to be a singular value. Therefore, the simulations will be run twice, one time for measuring the effect of the different design variables on the number of successful orbit determinations and once for the average position accuracy.

The values for each design variable are determined by using an orthogonal array. There are many different orthogonal arrays available to choose from. The objective in choosing an orthogonal array is to minimise the number of experiments that need to be performed. The orthogonal array is dependent on the number of design variables and the number of levels for each design variable (number of values the design variable can be). In this case, there are five design variables and it has been decided to use at least three levels for each variable. The lowest number of levels that can be chosen is two, however, this only provides a linear line and in many cases does not give any insight into where the possible optimal value of the design parameter lies. The smallest orthogonal array that can be used is the L25 array, see Appendix B. This orthogonal array allows for six design variables with five levels each; only five design variables will be tested, however, one or more columns can be left open without effecting the orthogonality (Taguchi, 1995). For the number of satellites per formation, only three levels can be used ($N_{for} = 2,3,4$), however, each design variable has five levels each, this is resolved by using the *dummy level technique* which allows for the assigning of a factor with m levels to a column with n levels, where $n > m$, this is done by assigning levels four and five to an already used value, these values will then be estimated with a higher level or precision than the levels that are not repeated (Taguchi, 1995). For the number of satellites per formation level four will be assigned to two satellites per formation and

level five to four satellites per formation.

The value which some design variables can take is dependent on another design variable. For example, the minimum focal length needed when the semi-major axis is 20,000 km is 0.82 m, while for a semi-major axis of 35,000 km the focal length can be as small as 0.15 m. So instead of using the same focal length for each level irregardless of the semi-major axis, the possible focal length range is divided in to five levels (a=21,000 km; [1=0.8, 2=0.85, 3=0.9,4=0.95, 5=1.0], a=35,000 km; [1=0.2, 2=0.4, 3=0.6, 4=0.8, 5=1.0]). The same holds for the relation between the number of satellites per formation and the total satellites, however, for the total satellites only four levels will be used, as this is the maximum when four satellites are used in a formation, the total number of satellites can only be four, eight, 12 or 16.

To determine the effect of each design variable on the performance metric a signal to noise ratio is calculated for each run. The signal to noise ratio is then calculated in the following way (Taguchi, 1995):

$$SN_i = 10 \log \left[\frac{\bar{y}_i^2}{\sigma_i^2} \right] \quad (8.1)$$

where \bar{y}_i^2 is the mean of the performance metric and σ_i is the variance. If performance metric needs to be maximised, which is the case for the number of orbit determinations, this equation can be written in the following way (Taguchi, 1995):

$$SN_i = -10 \log \left[\frac{1}{N_i} \sum_{u=1}^{N_i} \frac{1}{y_u^2} \right] \quad (8.2)$$

where y is the value for the performance metric and N is the number of tests per experiment. If the design variable needs to be minimised, which is the case for the average position accuracy, the signal to noise ration is calculated in the following way (Taguchi, 1995):

$$SN_i = -10 \log \left[\sum_{u=1}^{N_i} \frac{y_u^2}{N_i} \right] \quad (8.3)$$

In this case, the simulation is run three times per experiment and for each run a different seed (1, 242, 2345) is used to initialise the orbit of the space debris objects. The average S/N ratio for each level of each design variable is then calculated.

The simulation settings that will be used are the following:

Number of space debris objects	200	[-]
Simulation time	1	[week]
Time step	120	[s]

A total of 200 space debris objects will be simulated, this value has been chosen to give a good coverage of all possible orbits that could occur. The bounds for the orbital elements of the space debris objects are the same as mentioned in Chapter 3. A total simulation time of one week has been chosen, such that the constellations where the satellites have a semi major axis equal to the highest bound mentioned above has made a full revolution compared to the space debris objects in GEO. The time step is determined by the requirement of the IOD method that the spacing between observations needs to be at least 120 seconds (Handley and Hagerty, 2020). The smallest possible simulation step has been chosen because this allows for a fairer comparison between the constellation designs with a larger and smaller semi-major axis. For smaller semi-major axis the relative velocity is higher, which can result in too few observations of an object for the IOD, to limit this the smallest possible time step will be used.

8.1.1. S/N results

When looking at the different signal to noise ratios for the separate levels of the different design variables, the individual values of the S/N do not provide a lot of insight. The main use of these SNR values comes from looking at the difference between the maximum and minimum SNR value that occur for each design variable. The larger this difference is, the larger the effect the design variable has on the performance of the design.

In Table 8.1 the maximum and minimum SNR are given for each design variable as well as the difference between these values for the number of successful orbit determinations. As can be seen the total number of satellites has the largest effect on the number of successful orbit determinations, followed by the semi-major axis of the satellites in the constellation, the focal length has the third most effect, followed by the inclination difference of the satellites and the number of satellites per formation has the least amount of effect on the number of successful orbit determinations.

The SNRs for the average position accuracy are given in Table 8.2. The semi-major axis has the most effect on the position accuracy of the different constellation designs, followed by satellites per formation, difference in inclination, focal length and finally the total number of satellites.

The semi-major axis has a large effect on both the performance metrics and is therefore the most important design variable. A slight change in the semi-major axis will have a large effect on both the metrics, so extra consideration should be given to this parameter during the following optimisation.

The total number of satellites and the number of satellites per group have a large effect on one of the performance metrics but have only a limited effect on the other. These design variables can thus be changed to improve the performance with regards to one of the metrics while only having a limited effect on the other performance metric. This could be especially useful if increasing or decreasing the design variables had a positive effect on one of the metrics but a negative effect on the other metric.

The focal length and inclination both have an average influence on the two performance metrics. These design variables can be mostly used to further tune the constellation design.

8.1.2. Successful orbit determinations

The SNR presented in the previous section only provides a metric of how much each design variable effects the performance of the constellation design. It does not give insight into the relation between the different levels of each design variable and the two different performance metrics. To get a better understanding of these relations, the average performance metric for each level of each design variables are plotted in Figures 8.1 and 8.5, these figures will be discussed in this and the following section. Because for each level there are only five data points, there is a level of randomness that should be taken into consideration when discussing the results. This randomness is caused by interactions between two or multiple design variables. For example the performance of a certain focal length will partly be dependent on the semi-major axis, since not all combinations will be tested, it could be that certain focal lengths are tested using a more favourable semi-major axis than other focal lengths.

Semi-major axis

As can be seen in Figure 8.1, between levels two and five, there is a clear negative relation between the semi-major axis and the average number of successful orbit determinations. This was expected, a smaller semi-major axis (lower levels) allows a satellite to observe a larger region of the GEO belt at a single time step compared to when a satellite orbits closer to the space debris objects, leading to more observations which can turn in to successful orbit determinations. Additionally, the higher relative velocity of satellites with a smaller semi-major axis also allows that satellite to observe more different parts of the GEO belt in the same time frame as compared to a satellite with a higher semi-major axis.

These two reasons explain the negative relation between the semi-major axis and the number of observations. This negative relation, does not hold up for the first level, where there is a very signifi-

Table 8.1: Maximum, minimum and delta SN of the design variables for the number of successful orbit determinations

	Semi-major axis	Focal length	Sats. per formation	Inclination	Total satellites
Max SN [-]	27.1	24.5	22.5	23.8	28.0
Min SN [-]	16.2	16.2	17.7	17.0	14.1
Delta SN [-]	10.9	8.3	4.9	6.8	13.9

Table 8.2: Maximum, minimum and delta SN of the design variables for the number of successful orbit determinations

	Semi-major axis	Focal length	Sats. per formation	Inclination	Total satellites
Max SN [-]	30.6	25.4	29.2	28.1	25.3
Min SN [-]	19.1	19.6	18.4	20.9	21.9
Delta SN [-]	11.5	5.9	10.8	7.2	3.3

cant drop in observations compared to levels two and three, where an increase of observations was expected. The reason for this sudden drop can be explained by looking at Figure 8.2a, where the conversion rate (the number of successful orbit determinations compared to the number of observations) as a function of the semi-major axis is plotted. It can be seen that the conversion rate for a semi-major axis of 20,000 km is significantly lower than that of semi-major axis larger than 24,000 km. This explains why the number of successful orbit determinations for level one is significantly lower than for levels two and three.

There are two reasons why the conversion rate is lower for smaller semi-major axis, the measurement time and the relative measurement error. In Figure 8.2b the average measurement time as a function of the semi-major axis is plotted, there is clear positive relation between the measurement time and the semi-major axis. This is caused by the difference in relative velocity between the space debris objects and the satellites for the different semi-major axis. Additionally, for the smaller semi-major axis the relative measurement error is larger compared to that of satellites with a larger semi-major axis, due to the increased distance between satellite and space debris object. A shorter measurement time, which means less measurements, and a larger relative measurement error leads to an decreased accuracy of both the IOD and the UKF. In Figure 8.3a, the effect of an inaccurate IOD can be seen on the performance of the UKF, a very large error in the initial guess of the object causes the UKF to not converge and work properly. If the IOD or the UKF does not converge properly for a particular measurement set, this measurement set is not used, which leads to a lower conversion rate.

These two reasons explain why smaller semi-major axis result in a lower conversion rate, however, a more linear relation was expected, but there is a sharp jump between 20,000 and 24,000 km. Looking again to Figure 8.2b, the average measurement time is exactly 240 seconds for a semi-major axis of 20,000 km. This is equal to the minimum possible measurement time, at least three observations with a time step of 120 seconds. Since there is no occurrence of a measurement set with a higher measurement time than 240 seconds for a semi-major axis of 20,000 km, it is likely that the lower conversion rate is caused by the fact that for most observed space debris objects only one or two observations could be made, caused by the high relative velocity of the satellite compared to the object.

A lower time step would thus most likely result in a higher conversion rate and thus a higher number of successful orbit determinations. To test this, a smaller time step of 60 seconds was used for the constellations with a semi-major axis of 20,000 km, the results of this can be seen in Figure 8.3b. The number of successful orbit determinations for the first level is now no longer an outlier and follows the

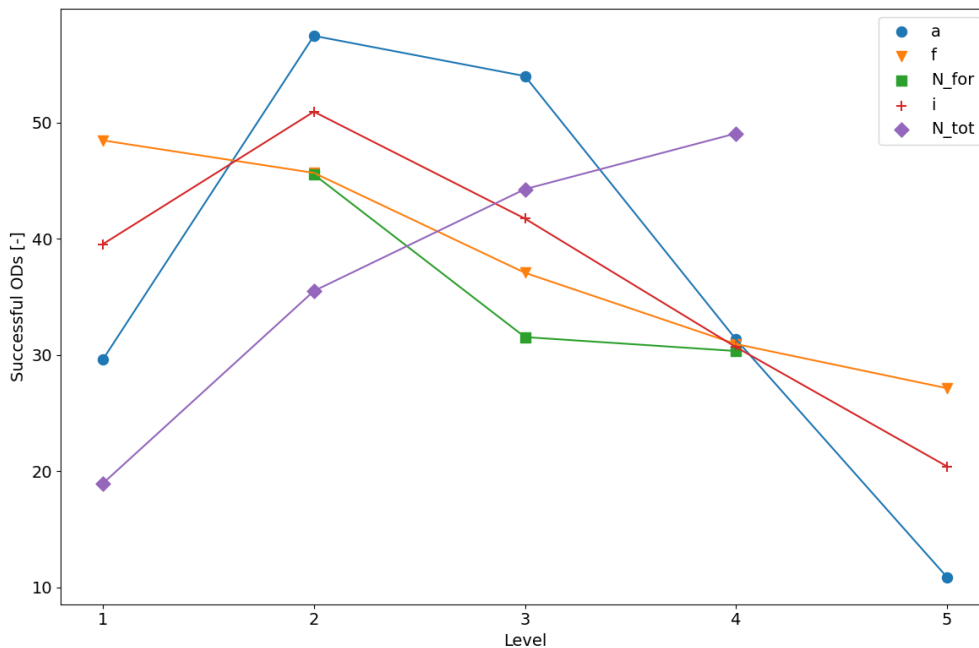


Figure 8.1: successful orbit determinations as a function of different design variable levels

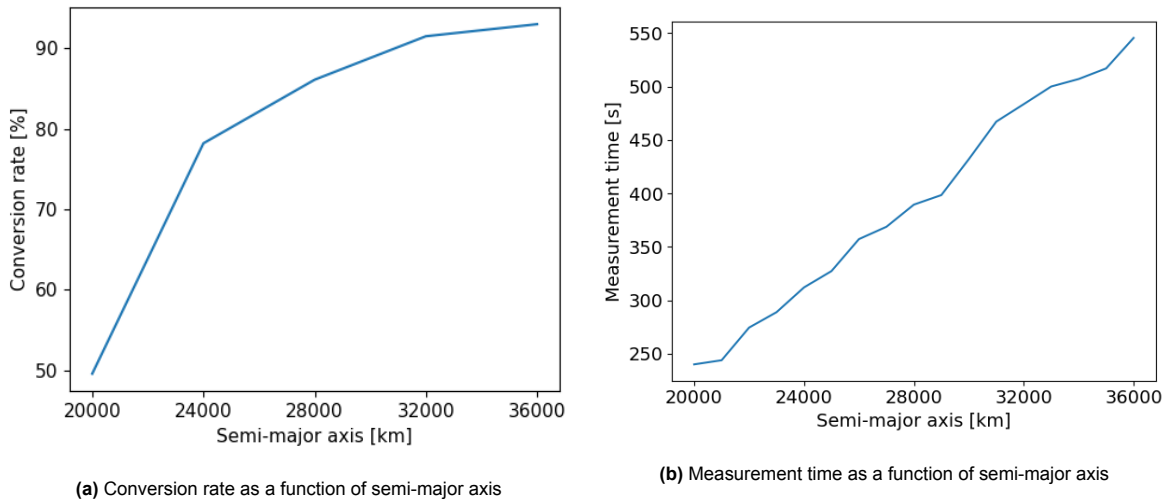


Figure 8.2: Conversion rate and measurement time as a function of semi-major axis

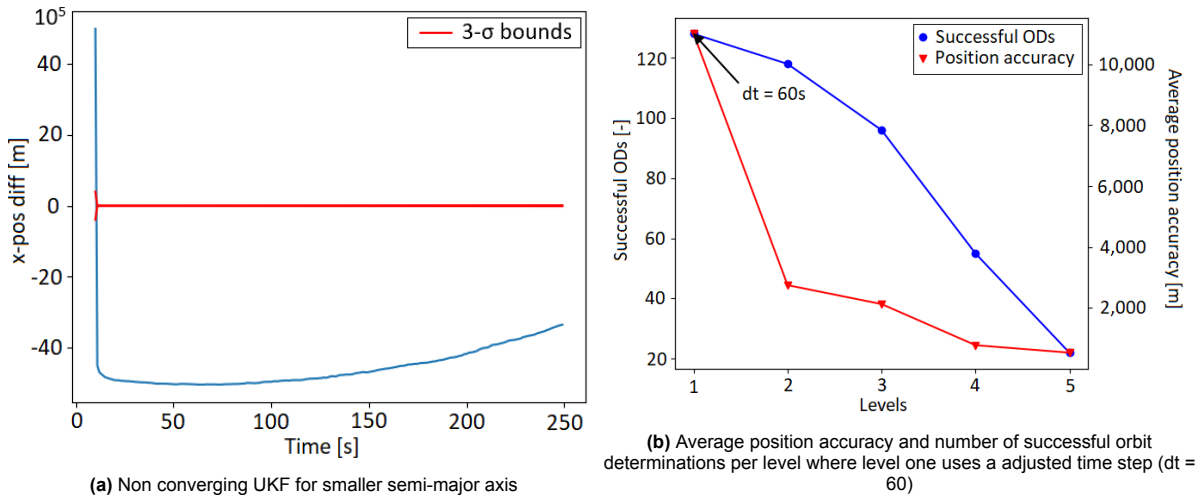


Figure 8.3: Non converging UKF (left) and effect of adjusting the time step (right)

trend of the other levels. However, it can also be seen that the accuracy of these orbit determinations for level one are significantly worse compared than would be expected from the other levels. The optimal design will thus not have a lower semi-major axis than 24,000 km and the time step can be kept at 120 seconds.

Focal length

The effect of the focal length on the number of successful orbit determinations can be seen in Figure 8.1, there is a clear negative relation between the focal length and the number of successful. There are two main reasons for this effect. First, a larger focal length results in a smaller FOV, this limits the number of objects a satellite can observe. Fewer observations will result in fewer measurement sets, which can be used for the IOD and UKF, and thus a larger focal length will limit the number of successful orbit determinations. Second, a smaller FOV also means that an object is less likely to be in this FOV for a longer amount of time and thus a smaller FOV will comparably result in more objects, where less than three observations can be made. This limits the number of successful orbit determinations. Additionally, the larger FOVs also results in more measurements, which increases the changes of convergence of both the IOD and UKF. This increases the conversion rate and thus the number of successful orbit determinations.

Satellites per formation

In Figure 8.1 it can be seen that the number of observations slightly decreases as the number of satellites per formation increases, especially when going from two satellites per formation to three satellites. As expected from Table 8.1, the effect of the number of satellites per formation is not that great, the difference between two and four satellites is only around 15 successful orbit determinations. The main reason for the difference is the fact that for a measurement set to be used for IOD and UKF, the object needs to be observed by all satellites in the formation for at least three measurements. The object thus needs to be in the region where the FOV of all satellites in the formation overlap for more than three time intervals. For a larger number of satellites per formation, this region where the FOV's overlap is smaller compared to when only two satellites make up a formation. This leads to a slight decrease in observations and thus a decrease in successful orbit determinations.

Inclination difference

The number of successful orbit determinations for different levels of inclination difference shows comparable behaviour as for the different levels of semi-major axis, as can be seen in Figure 8.1. Between levels two and five there is a clear negative relation between the inclination difference and the number of successful orbit determinations. But for level one there is a sudden drop in number of successful orbit determinations.

The reason for the negative relation between level two and five is partly the same as the reason why there exists a negative relation for the number of satellites per formation. For larger differences in inclination between satellites, the region where all FOVs coincide is smaller, especially when the argument of periapsis is close to $\pi/2$ or $3\pi/2$. This smaller region leads to less observations and thus successful orbit determinations compared to when the inclination differences between the satellites in the formation is smaller.

The reason for the sudden drop in number of successful orbit determinations can be seen in Figures 8.4 and 8.5. Figure 8.4 shows that there is a significant difference in conversion rate between 2.5 degrees and the higher differences in inclination. The reason for this is the relatively high average position accuracy for an inclination difference of 2.5 degrees as can be seen in Figure 8.5. This inaccuracy sometimes leads to the UKF not converging, which in turn lowers the conversion rate and therefore the number of successful orbit determinations.

Total satellites

As expected, in Figure 8.1 it can be seen that a larger number of total satellites lead to an increase in the number of orbit determinations. A larger number of total satellites increases the total region of the GEO belt that can be observed at each time interval, as well as increasing the GEO belt coverage of the whole constellation compared to a constellation with less total satellites. The number of successful orbit determinations increases for each higher level, however, it can be noted that the gradient of the

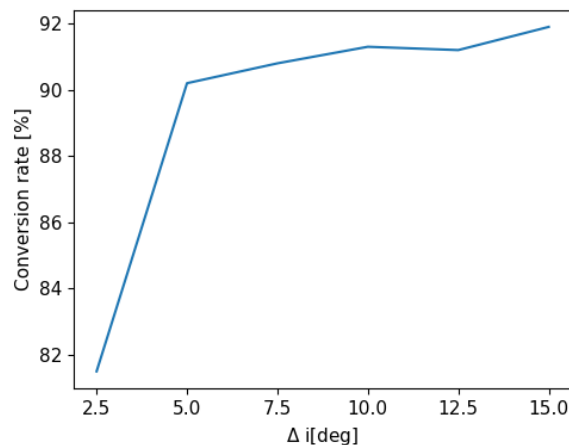


Figure 8.4: Conversion rate as a function of inclination

increase between levels decreases for the higher levels. This could signify that after a certain amount of satellites the number of successful orbit determinations would not increase anymore.

8.1.3. Average position accuracy

Semi-major axis

In Figure 8.5 there is a clear positive relation between the accuracy of the orbit determinations and the semi-major axis. The position accuracy for a semi-major axis of 36,000 km is almost a factor of magnitude smaller than that of a satellite constellation with a semi-major axis of 20,000 km. There are two reasons for this positive relation.

The first reason is the fact that the relative measurement error is smaller when the observing satellites are located closer to the space debris object. The resulting position error, when using the same measurement error, is almost four times as large for a constellation with a semi-major axis of 20,000 km compared to a semi-major axis of 36,000 km. This larger relative measurement error has a negative effect on the accuracy of both the IOD and the UKF. The second reason is that the relative velocity is higher for a smaller semi-major axis compared to a larger semi-major axis, as already explained in the previous section, this leads to less measurements of the same object, which in turn decreases the accuracy of the IOD and UKF.

Focal length

A larger focal length leads to worse position accuracy as can be seen in Figure 8.5. Increasing the focal length decreases the FOV of the telescope, if the sensor is the same size, a decrease in FOV means that on average each space debris object spends less time in the FOV of the satellite, which limits the number of observations that can be done and this in turn decreases the accuracy of both the IOD and UKF.

Between levels four and five, the accuracy is actually slightly better for the higher level, but this is most likely caused by the randomness due to the limited amount of data points for each level and the fact that the effect of the focal length is not that great, as could be seen in Section 8.1.1, which increases the relative effect of the randomness.

Satellites per formation

The larger the number of satellites per formation, the better the average position accuracy gets, as can be seen in Figure 8.5. This effect is most noticeable between level three (two satellites per group) and level three (three satellites per group), where the average position error is almost twice as large for

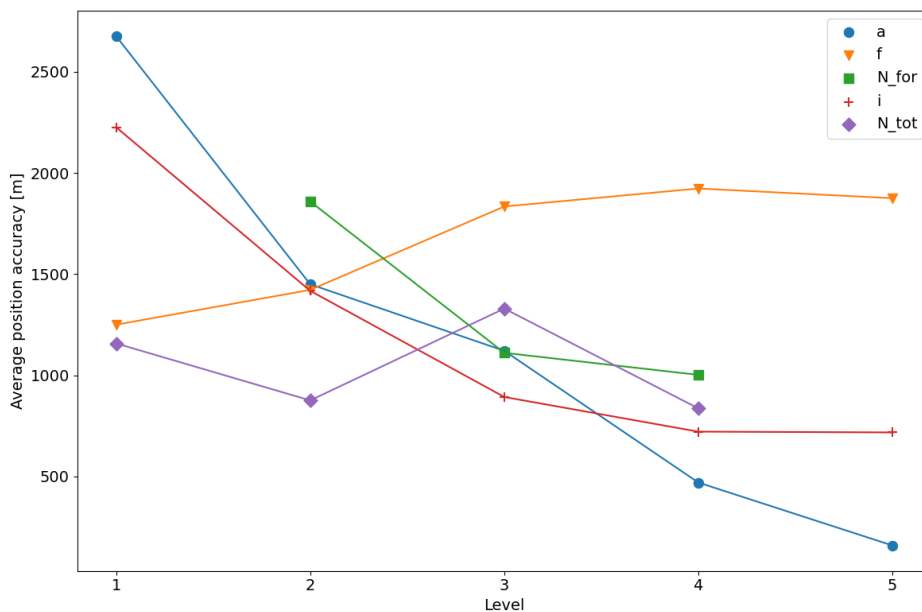


Figure 8.5: Average position accuracy per level

level two compared to level three. Adding a fourth satellite to the group still has a positive effect on the average position error, but the effect is smaller compared to when a third satellite is added, this also confirms results seen in Chapter 7.

Having more satellites per formation improves the average position accuracy in two different ways. First of all, the extra satellites increase the number of measurements for each object. This reduces the effect of the random errors and therefore leads to a better accuracy. Secondly, when a satellite and a space debris object are in a co-planar orbit, the accuracy of the orbit determinations decreases significantly. Adding extra satellites with a different inclination to the group, makes sure that at least one satellite is in a non co-planar orbit, which improves the average position accuracy.

Inclination difference

In Figure 8.5 there is a clear positive relation between the inclination difference and the average position accuracy, for the lower levels. However, for the levels three, four and five the position accuracy does not improve significantly when increasing the difference in inclination.

The larger the difference in inclination between the satellites in the group, the better the accuracy of the IOD and UKF becomes. A larger difference in inclination will lead to a larger difference in position between each satellite in the group. Therefore, the measurement vectors taken for a space debris object by each satellite in the formation will vary more to each other compared to when a small inclination difference is used. This apparently has a clear positive effect on the accuracy of both the IOD and the UKF, up until a certain inclination difference after which the position accuracy does not further improve with an increase in inclination difference.

Total satellites

In Figure 8.5 it can be seen that the average position accuracy for the different level of total satellites fluctuates around 1000 meters, this is also close to the average of the position accuracy for all 25 different constellation designs. In theory the different levels of total satellites should not have a significant effect on the average position accuracy. This is because the level of total satellites signifies the number of satellite groups. An increase in the number of satellite groups should not effect the position accuracy, since an object can only be observed by one group at the time. Adding extra groups thus should not effect the accuracy of the IOD or UKF. The fluctuation that can be seen in the figure is most likely caused by randomness and the fact that for each level only five constellation designs were simulated.

Conclusions

The semi-major axis has a negative relation on the number of successful orbit determinations, except for the lowest level, where the number of successful orbit determinations is limited due to the low average observation time. The semi-major axis has the opposite effect on the average position accuracy, where a higher semi-major axis leads to a higher average accuracy.

A smaller focal length leads to both a higher number of successful orbit determinations and a higher average position accuracy. A small focal length will thus lead to the best overall performance. The lowest possible focal length is dependent on the semi-major axis of the design, however, choosing the absolute minimum focal length for the chosen semi-major axis will most likely not lead to the optimal performance. This is because the lowest possible focal length is calculated by using the most optimal observation scenario, the system will then not be able to detect smaller objects or objects that are further away. The focal length thus still needs to be optimised, however, only the larger focal lengths do not have to be considered anymore.

The number of satellites per formation has a negative relation with the number of successful orbit determinations and a positive relation with the average position accuracy. However, for both the performance metrics the difference between three and four satellites is far smaller compared to the difference in performance between two and three satellites. Considering the extra cost of adding a satellite, using three instead of four satellites will most likely not be worth it.

The inclination difference between the satellites in a group has a negative relation with the number of successful orbit determinations, except for the first level where a low conversion rate limits the performance. The inclination difference has a positive relation with the average position accuracy, however, as the inclination differences become larger the effect of increasing the inclination difference does not improve the accuracy significantly. The most optimal inclination difference will therefore most likely

be at or before the point where increasing the inclination difference does not significantly improve the average position accuracy.

The number of total satellites in the constellation has a positive relation with the number of successful orbit determinations and it has almost no effect on the average position accuracy. When only looking at the performance of the constellation, a large number of total satellites will always be preferred, however, this does not take into account the added cost of adding these satellites.

As can be seen the semi-major axis, inclination difference and number of satellites per formation have a positive effect on one of the performance metrics, but a negative effect on the other. The most optimal design point will thus most likely not be at lower or upper bounds of the design variables, but somewhere in the middle region. Where exactly this optimal point will be, will also depend on which performance metric is deemed more important and other consideration such as the complexity and cost of the mission.

8.2. Limited factorial design

In the previous section it could be seen that most of the design variables have a negative effect on one of the performance metrics but a positive effect on the other metric. A large semi-major axis leads to higher position accuracy but a lower amount of total orbit determinations etc. The only design variable where this is not the case is the focal length, where a smaller focal length leads to both higher accuracy and number of orbit determination. This, in combination with the low number of constellation designs that have been simulated, makes it very difficult to find a optimal design. Therefore, further optimisation still needs to be performed.

To perform this optimisation a grid search, or limited factorial design, will be used. A grid search evaluates all possible combinations of discrete design variables. This method has been chosen in favour of other optimisation methods, such as genetic algorithms, because each simulation of a constellation design is computationally intensive and thus the total number of constellation designs that can be tested is limited. Furthermore, the use of discrete design variables can also give additional insight into the relation between the design variables and performance metrics and the interactions between multiple design variables.

A grid search can still be very computational intensive if many design variables with many different possible values are used. Both the number of design variables and the number of different possible values for each design variable thus need to be limited. One way to do this is by not using the total number of satellites as a design variable. The total number of satellites has no effect on the accuracy of the orbit determination, it also does not effect the number of orbit determinations a single group of satellites can make. The best performing design of a group of satellites will therefore also lead to the best performing constellation design once the total number of satellites is increased. Additionally, not including the total number of satellites as a design variable has the added effect on limiting the average simulation time per constellation design, as only a maximum of four satellites will be used instead of 16 satellites. The effect of the total number of satellites will be further investigated once the best formation design has been found.

The values that each of the remaining design variables can take can be found in Table 8.3. Most of these bounds are similar to those used in Taguchi method, but this time with a smaller interval between the bounds. This is because each design variable has positive effect on one of the performance metric and a negative effect on the other, thus all of these values can lead to a Pareto optimum point and should thus be taken into account during the simulation. However, for the semi-major axis and the focal length slight differences have been made compared to the Taguchi method. In the previous section it became clear that at the lowest level of semi-major axis ($a = 20,000$ km) the number of observations suddenly dropped due to a lower conversion rate, this will therefore not lead to an optimal solution, therefore, the lowest semi-major axis that will be used is 24,000 km. For the focal length, different levels will again be used instead of real values, this is because the possible focal lengths are determined by the semi-major axis. In the previous section it was also found the a lower focal length leads to both a higher orbit determination accuracy and a larger number of orbit determinations. This has been accounted for by taking only the smallest $2/5^{\text{th}}$ of the possible focal lengths and dividing those into five different levels.

In Figure 8.6 the results of the grid search are plotted. The effect of the different design variables on the two performance metrics follow the same behaviour as already reported in the previous section. A larger number of satellites per group results in a higher position accuracy, while only having a very

Table 8.3: Design variables limited factorial design

Number of satellites per group	[2, 3, 4]	[-]
Semi-major axis	[24,000; 26,000; ...; 36,000]	[km]
Focal length	[1, 2, 3, 4, 5]	[-]
Inclination difference	[2.5, 5, ..., 15]	[deg]

small effect on the number of total orbit determinations. As can be seen in the figure, most of the Pareto optimal constellation designs have four satellites. A small semi-major axis leads to a higher number of observations but a lower position accuracy. All possible values of the semi-major axis could lead to a Pareto optimum constellation design. As discussed earlier, a smaller focal length leads to both more orbit determinations and to a higher position accuracy. In Figure 8.6, there seems to be a mix of both large and small focal lengths near the Pareto front. However, this is due to the fact that the focal length is dependent on the semi-major axis, a small semi-major axis can only use large focal lengths, all points near the Pareto front use the smallest or second smallest possible focal length for the semi-major axis. For the inclination difference, there is no clear best solution, although it is clear that the constellation designs with a inclination difference between 5 and 12.5 degrees offer better performance than the inclination difference at the lower and upper bounds.

From the results mentioned above, a Pareto optimal front could be made and an optimal solution could be chosen. However, the intervals between each possible value for the design variables is still quite large, which means that the true optimal design probably lies somewhere between the intervals. So instead of choosing a Pareto optimal constellation design from the results above, the results will be used to further narrow down the upper and lower bounds of the design variables, which will allow for smaller intervals and this will more likely result in a (near) optimal design.

The narrowing down of the bounds of the design variables will be done in the following way. First a point will be chosen, where the x-coordinate is the number of succesfull orbit determinations and the y-

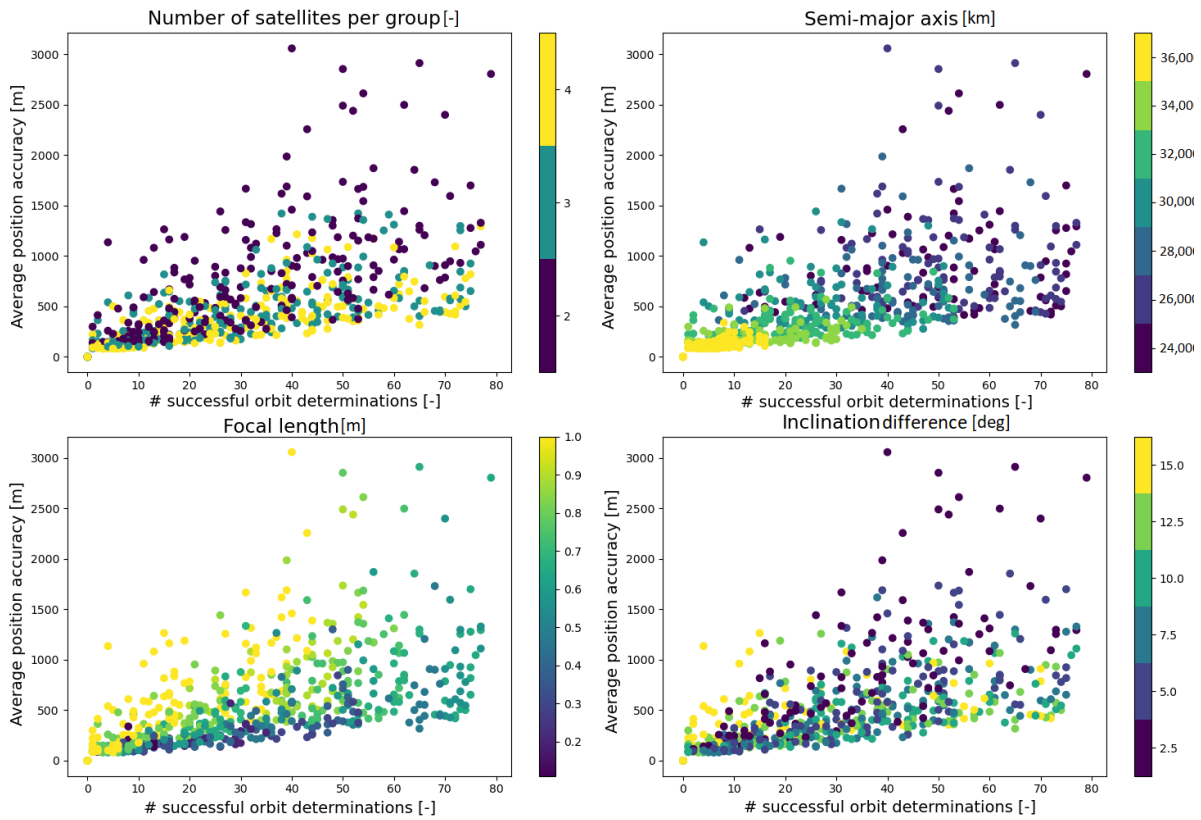


Figure 8.6: Performance metrics for different constellation designs

coordinate is the average position accuracy, this point will represent the most optimal performance. The distance between each point in Figure 8.6 and the chosen point will be calculated. The 20 points closest to the optimal performance will be selected, from these 20 best points, the minimum and maximum value of each design variable will be used as the new bounds.

When picking the coordinates for the point, two things need to be taken into account i.e., performance and mission cost. The performance should be maximised and the mission cost should be minimised. There are two performance metrics, the number of successful orbit determinations and the average position accuracy of the orbit determinations. Looking at Figure 8.6, it is clear that a higher number of successful orbit determinations leads, on average, to a lower position accuracy. There is thus no solution that will lead to the highest performance for both metrics and a point should be chosen that leads to satisfactory performance for both of the metrics, this also means that this point will not lie close to the edges of the Pareto front. There are also no requirements for the number of orbit determinations and average position accuracy, although for the average position accuracy it should be noted that the average position accuracy of publicly available orbit estimations is around 4 km for objects in GEO (Vallado et al., 2013). Considering this, and the fact that all points already have a higher accuracy, a slight preference could be given to a higher number of orbit determinations at the cost of a worse accuracy. There is thus still a large number of points that could be chosen, to make a choice the mission cost should also be considered.

There are three design variables that will have a direct effect on the mission cost, the number of satellites per group, the total number of satellite and the focal length. The total number of satellites will be discussed in a later section, so for now the focus lies with the other two variables. The number of satellites per group will increase the production and launch cost of the mission, a smaller number of satellites per group is thus preferable. Additionally, for the same number of total satellites using less satellites per group also has the added benefit of making it possible to use more groups and thus increasing the GEO region it can search at the same time. However, as could already be seen in Figure 8.6, most of the optimal constellation designs consist of four satellites per group.

A larger focal length will lead to a larger telescope, this has two main effects on the mission cost, it will increase the size of the satellite, which in turn will increase the weight and subsequently launch cost. A larger telescope will also require more power, this will increase the size, cost and weight of the power subsystem and total satellite. It is thus important to minimise the focal length as much as possible.

In Figure 8.6, one point can be identified that offers a high number of observations a relatively good accuracy and minimises the focal length and possibly the number of satellites per group. At a number of successful orbit determinations of around 27.5 there are still constellation designs with an focal length between 0.2 and 0.3 meters and there are also some constellation designs with 2 or 3 satellites per group. Therefore, this point will be chosen as a reference point. By looking at the minimum and maximum values of the design variables of the 20 points closest to the reference point, the new bounds can be set, which can be seen in Table 8.4, the focal length are again adapted to only use the 5 smallest possible focal lengths per semi-major axis. The usage of more than 20 points was also investigated. When using the closest 40 points, 38 of those points still lie inside of the bounds described in Table 8.4 and the best 10 points were centered around the middle of the bounds. It is thus highly unlikely that the optimum lies somewhere around the bounds described below, using more than 20 points would thus be computationally inefficient (more simulations) or would negatively impact the accuracy of the optimisation (larger intervals).

The results of the factorial design simulation using smaller bounds and intervals can be seen in Figure 8.7. The results follow the same trends as those in Figure 8.6, with some slight differences. For the number of satellites per group, there is more separation in the average position accuracy between the different number of satellites per group, four satellites clearly provide the best accuracy and two

Table 8.4: Design variables limited factorial design, narrow bounds

Number of satellites per group	[2, 3, 4]	[-]
Semi-major axis	[27,500;28,000; ..., 33,000]	[km]
Focal length	[1, 2, 3, 4, 5]	[-]
Inclination difference	[5, 6, ..., 13]	[deg]

satellites the worst. In Figure 8.6, there were some constellation designs using two satellites that gave a comparable accuracy as four satellites per group. However, using these smaller bounds it is clear that more satellites will always provide a higher accuracy when all other parameters are the same. By decreasing the bounds of the inclination difference, the performances of the different designs are more randomly distributed than previously. This signifies that the inclination difference has only a limited effect on the two performance metrics.

The same procedure of choosing a point and narrowing the bounds by using the 20 points closest to this point was again repeated. However, there was only an increased performance for the lower constellation designs with a low number successful orbit determinations, where the accuracy was increased significantly. However, this was only the case for constellation designs which resulted in 25 or less successful orbit determinations, for the points with more orbit determinations, the accuracy increase was not significant. As mentioned earlier a higher number of successful orbit determinations is preferred to a higher accuracy. So the smaller bounds and intervals did not improve the performance in the most important region, therefore, a constellation design in Figure 8.7 will be used.

The same reasons that were used for picking a reference point to narrow down the bounds and intervals are used again to pick the best performing point. For the performance metrics, a larger number of successful orbit determinations is preferred over an increase in accuracy. For the design variables, a smaller focal length and a lower number of satellites per group is preferred. Using these objectives, a constellation design was chosen, for which the parameters are displayed in Table 8.5 and Figure 8.8. This design resulted in 32 successful orbit determination with an average position accuracy of 232 meters. This specific constellation design was chosen because, constellation designs with four satellites per group only resulted in an increased accuracy of around 10%, while the constellation designs with only two satellites resulted in a decrease of accuracy of 60%, without increasing the number of successful orbit determinations significantly. Additionally, this constellation design also uses a relatively small focal length.

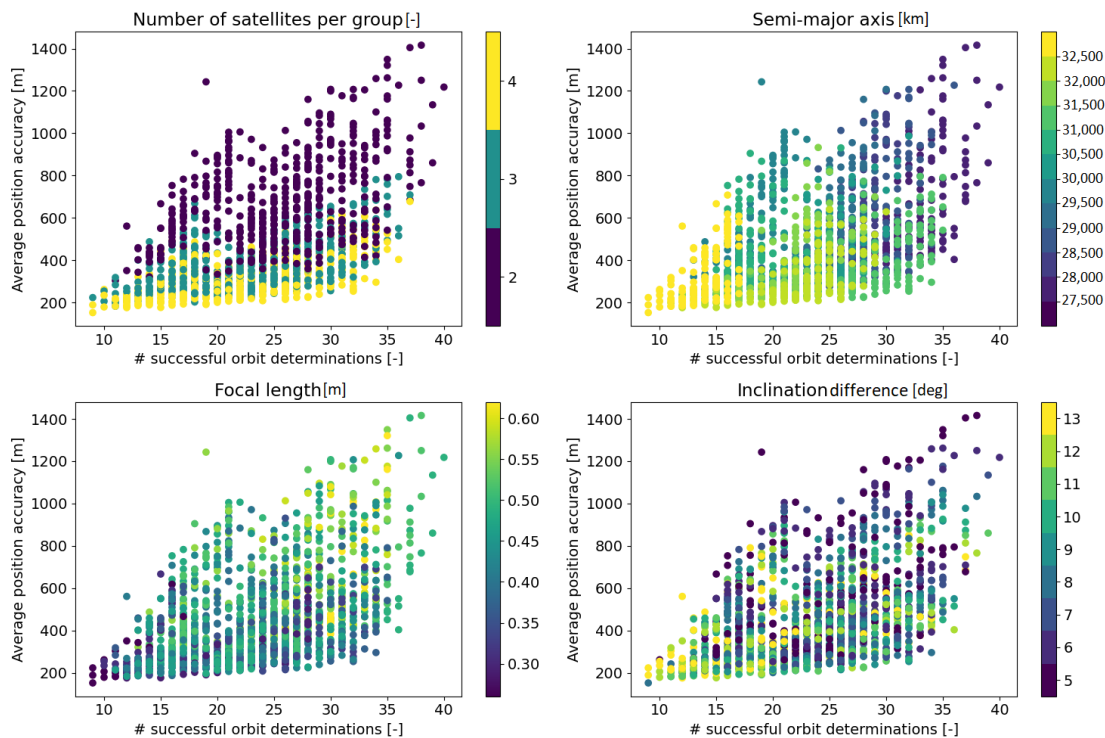
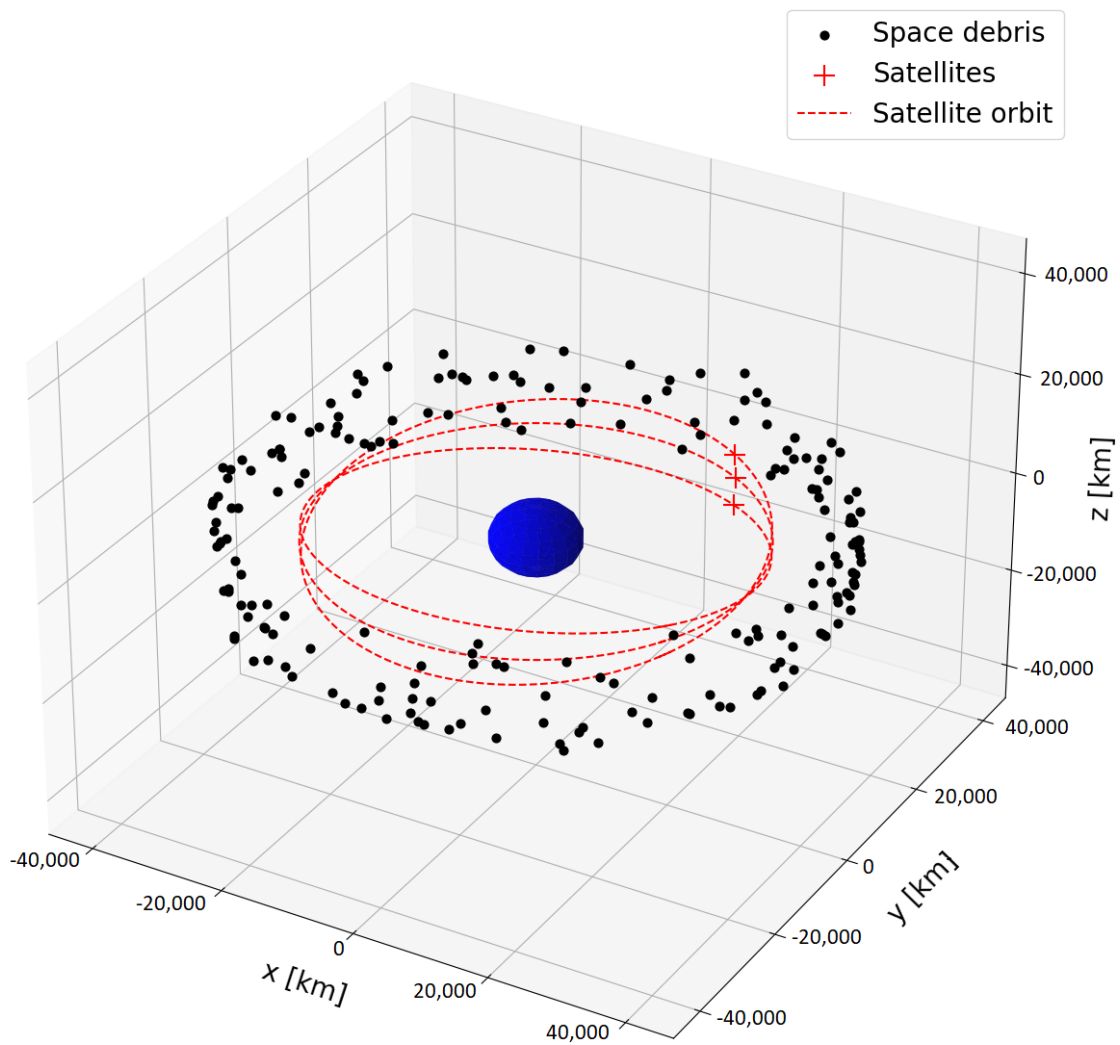


Figure 8.7: Performance metrics for different constellation designs using smaller bounds

Table 8.5: Design variables for optimal constellation design

Number of satellites per group	3	[-]
Semi-major axis	31,000	[km]
Focal length	0.37	[m]
Inclination	-11, 0, 11	[deg]

**Figure 8.8:** Constellation design

Analysis of variance

One of the benefits of using a factorial design and thus discrete values for the design variables is that the effect of the different variables on the performance metrics can be more precisely analysed using an analysis of variance (anova), compared to when continuous values for the design variables are used. One way to test which design variable has the largest effect on the is by looking at the F-test for each variable. The F-test compares the variance between sample means and the variance within samples, the larger the F-value for a design variable the larger the effect that variable has on a performance metric. To perform this F-test, the performance metrics of all constellation designs which used either the maximum or minimum value of a design variable were used. It should be noted that the F-test works the best when the samples are normally distributed. For both the performance metrics this is not the case, this means that the actual F-values do not give any real insight into the effect of the design variable on the performance metrics. However, comparing the F-values for each performance metrics of the different design variables does provide insight into which variable has the largest effect on the metrics.

In Table 8.6, the results of these F-test can be seen. Looking at the F-values for the orbit determination accuracy, it is clear that the number of satellites per formation has the largest effect on the accuracy, followed by the semi-major axis, inclination difference and finally the focal length has the smallest effect on the accuracy. The reasons for why these variables have certain effects on the performance metrics has already been discussed in previous sections and will thus not be repeated. The design variable which has the largest effect on the number of successful orbit determinations is the semi-major axis, followed by the focal length, number of satellites per formation and finally the inclination difference.

The semi-major axis has a large effect on both accuracy and number of successful orbit determinations and is thus the most important design variable which has the most effect on the total performance of a constellation design. If the accuracy needs to be improved without effecting the number of successful orbit determinations too much the number of satellites per formation should be changed. If the opposite is needed, more successful orbit determinations without effecting the accuracy too much, the focal length needs to be changed.

8.3. Optimal design performance

In this section the performance of the optimal constellation design will be discussed. To do this, first the UKF can be tuned for this specific constellation design. In the previous sections, the UKF was initialised using values that were dependent on the semi-major axis of the constellation design. This was done by using some test cases and using that data in a regression analysis to determine a formula for the initial values of the UKF which produced good performance for all different constellation design. However, this performance was not optimal for most cases. Using more optimal values for the initialisation of the UKF gives the following performance, number of successful orbit determinations = 34 and average position accuracy = 198 m, which is an increase of 6% and 15%, respectively. However, it should be noted that for only 17% of the space debris objects at least one successful orbit determination could be performed.

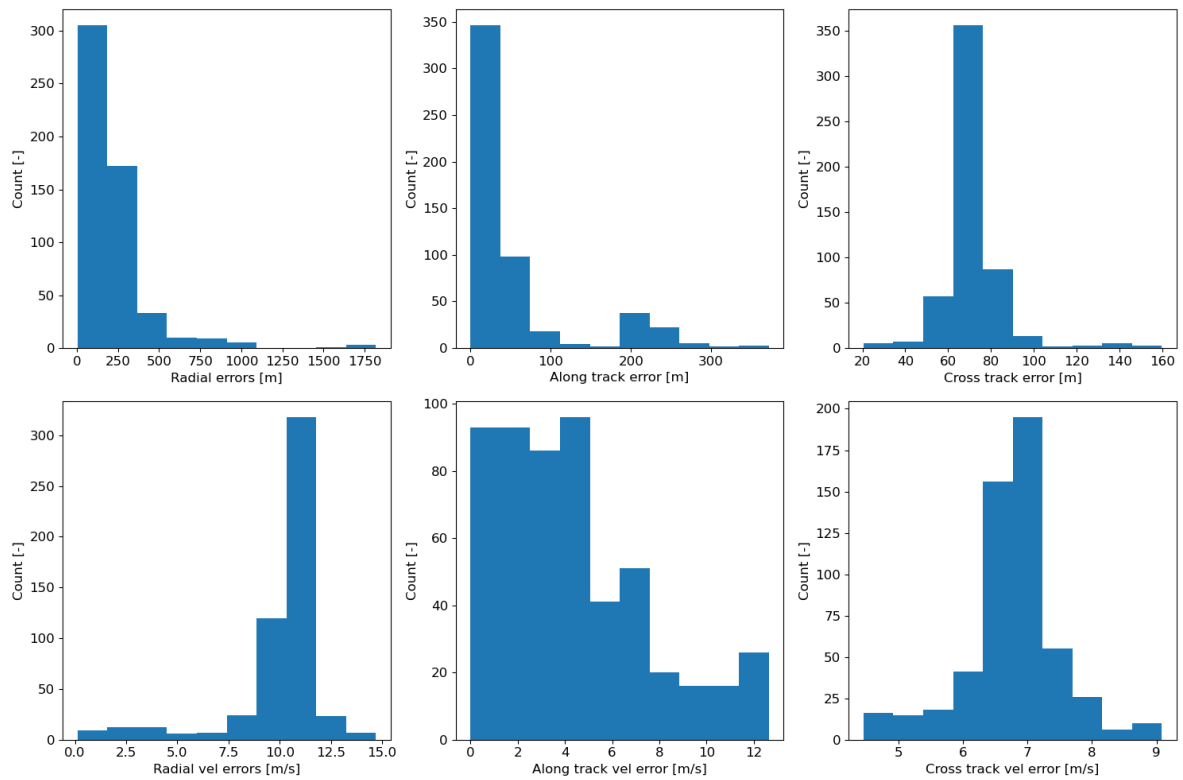
In Figure 8.9 the distributions of the orbit determination errors in the RSW-frame are plotted, in Table 8.7 the average errors are shown. There is not a lot of variance in the distribution of the errors, except for the along track velocity error and some outliers for the radial and along track position error. For the position errors, the radial errors are significantly larger than both the along- and cross-track position error, this is also the case for the velocities. Notably, the orbits of the space debris objects did not have a significant effect on the orbit determinations.

Table 8.6: F-values of the different design variables for the two performance metrics

	Number of satellites per formation	Semi-major axis	Inclination difference	Focal length
Orbit determination accuracy	358.2	243.6	79.3	20.97
Number of successful orbit determinations	67.2	296.0	39.4	148.3

Table 8.7: Mean orbit determination error in RSW-frame

Radial	249.1	[m]
Along-track	96.1	[m]
Cross-track	69.1	[m]
Radial velocity	8.9	[m/s]
Along-track velocity	6.2	[m/s]
Cross-track velocity	6.6	[m/s]

**Figure 8.9:** Errors of orbit determination in RSW-frame

8.3.1. Number of total satellites

In this section the effect of adding more groups of three satellites to the constellation design on the performance metrics is investigated. The total number of satellites does not effect the accuracy of the orbit determinations so only the effect on the number of successful orbit determinations will be looked at, this can be seen in Figure 8.10. As expected there is a clear positive effect of the total number of satellites on the number of successful orbit determinations. However, there are two things that can be noted.

First of all, it was expected that each additional group of three satellites would increase the number of successful orbit determinations, however, when looking at the graph it can be seen that this is not the case: there are multiple points on the graph, where an additional group of satellites actually leads to a significant decrease in the number of orbit determinations (for example between 18 and 21 total satellites). This can be explained by looking at the way the initial states of the satellites are determined. Each group of three satellites are divided evenly over the whole orbit, the angle between all groups is the same. This means that when a group is added the initial state of each satellite is changed. As can be seen from the graph the initial states of the satellites can have a significant influence on the number of successful orbit determinations that can be done. Secondly, the effect, barring the fluctuations due to changes in the initial states of the satellites, of adding extra satellites to the constellation design on the number of successful orbit determination gets smaller the higher the number of total satellites. There is a 43% increase between three and six total satellites, but after around 30 satellites this increase lies somewhere between 1 and 4%.

In Figure 8.11, the percentage of space debris objects for which a successful orbit determination has been performed is plotted as a function of their orbit parameters and size for a constellation with a total of 18 satellites, for example 80% of space debris objects with an inclination between 0 and 2 degrees had at least one successful orbit determination. It should be noted that due to the distribution of the space debris objects, see Figure 3.1, some results are effected by randomness, for instance only two space debris objects had a semi-major axis in the highest bin, those two objects also happen to have a small radius and high inclination which decrease the change of observations, thus making the percentage very low. Thus, at some bins with only a few objects (less than 10), there is a lot of randomness in the results and these results should not be given a lot of significance and will be mostly ignored during the analysis. For the semi-major axis, the first and last bin only have very few space debris objects, for the inclination there are very few objects between 0 and 5 degrees. For eccentricity, there are only very few objects with an eccentricity above 0.004. The size of each space debris object is uniformly distributed, so each bin has approximately the same number of objects in them.

Looking first at the distribution for the semi-major axis, there is a slight decrease in percentage as the

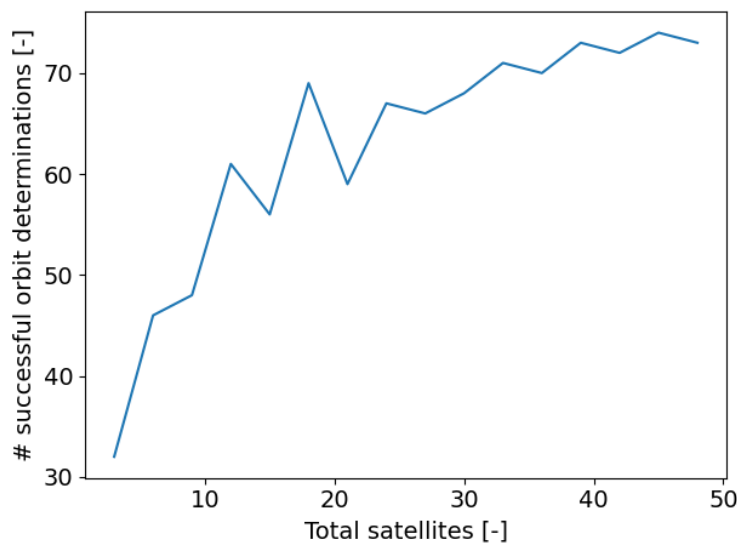


Figure 8.10: The number of successful orbit determinations as a function of total satellites

semi-major axis gets larger, however, this decrease is only around 10%. Two reasons can be identified for this decrease. First, a larger distance between the observer and object decreases the SNR and thus decreases the change of observations. Second, the relative velocity between the observer and object is smaller for larger semi-major axis, which increases the observation time, which increases the change of a successful orbit determination.

For the inclination difference there is a clear negative relation between the inclination difference and percentage of successful orbit determinations. Between 12 and 15 degrees inclination difference, a successful orbit determination can be performed for only around 20% of the objects. Looking back at Figure 3.1, most of the currently tracked space debris objects have an inclination in this interval. This poor performance for objects with a high inclination is thus a large reason for the low total percentage (34% for 18 total satellites) of space debris objects for which an successful orbit determination could be performed. The main reason for this bad performance for the higher inclination is these objects only cross the possibly observed region for a relatively short period of time. It was found that the system could observe these objects, around 85% of all objects with a inclination near 15 degrees were observed at least once, however, due to the short observation time a successful orbit determination could not be performed.

The eccentricity has a small negative effect effect on the number of successful orbit determinations. This could be caused by the larger chances in orbital velocity for the higher eccentricity, which decreases the amount of time an object can be observed and thus decreases the chances on a successful orbit determination.

As already expected, a larger sized-space debris-object leads to more successful orbit determinations, this is caused by the larger object reflecting more light and thus increasing the SNR and thus the chance on observation. One thing that should be noted is the fact that zero objects with a size between 1 and 2 cm has been detected. To detect these objects, a larger focal length or a larger semi-major axis should be used, but as already discussed in this report, this will lead to an overall degradation of the performance of the constellation design.

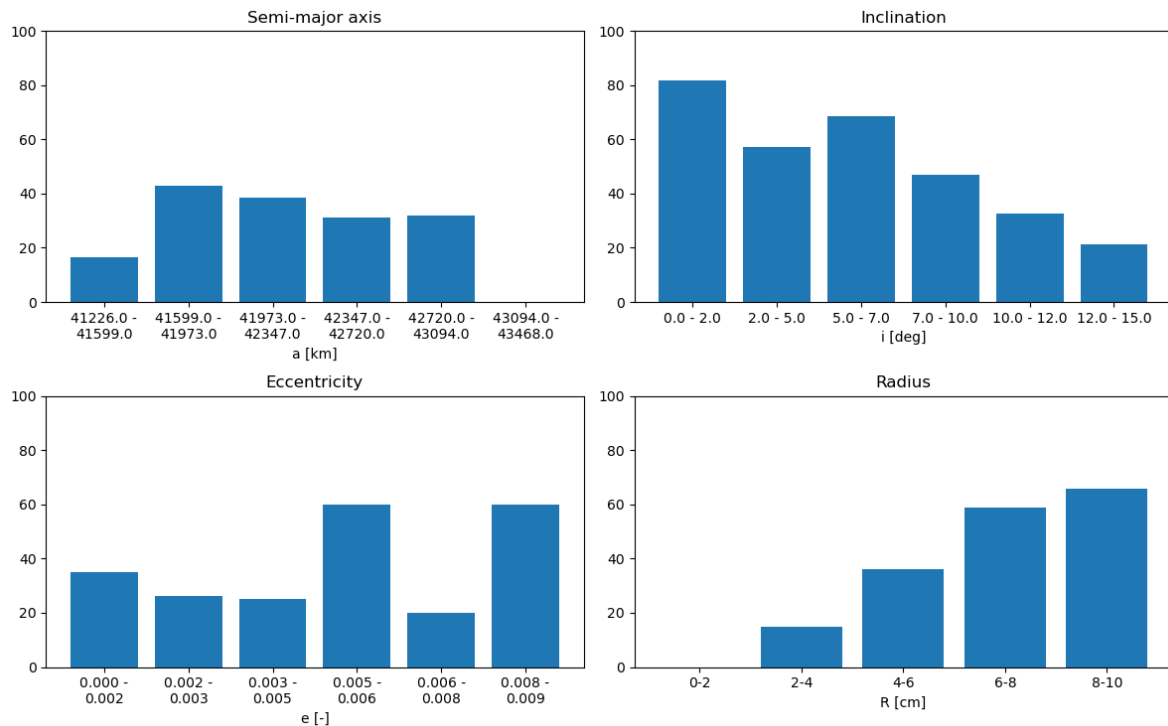


Figure 8.11: Percentage of observed space debris objects as a function of their orbit parameters and size

8.3.2. Maintain custody

Another way to look at the performance of the constellation design is by looking at if the system would be able to reacquire an already observed object, which is called maintaining custody. If the constellation design is not able to do this, each object needs to be reacquired and it would be very difficult to determine if an observed space debris object is new or if it has already been observed. Custody can be maintained if, by using an active search method, pointing the sensors to where it is estimated the object will be, the object flies through the FOV of the sensor. This is achieved if the following criteria are met:

$$\epsilon_{cross-track} < D \cdot \tan \frac{\theta}{2} \quad (8.4)$$

$$\epsilon_{along-track} < D \cdot \tan \frac{\theta}{2} \quad (8.5)$$

where D is the distance between the observing satellites and the space debris object and θ is the FOV-angle. Maintaining custody is a good performance because it is both dependent on the accuracy of the orbit determination and the frequency of observations of a single space debris object, which is influenced by the number of total satellites.

To determine if custody can be maintained, the following method is used: 200 orbits are simulated between the time of the first orbit estimation and the second orbit estimation. The initial states are determined by randomly adding an error to the actual initial state of the space-debris object. The mean of this random error is zero, while the variance comes from covariance matrix from the UKF. The covariance will thus be different for different space-debris objects, it can be anywhere from a couple of meters to upto around 500 m. The cross and along track error at the time of the second orbit determination is then calculated, for each of the 200 orbits. If the $3\text{-}\sigma$ variance of these errors are lower than the maintain custody limit set by the FOV-angle and the distance between observer and object, custody can be maintained.

In Figure 8.12 the results can be seen, here the percentage of objects, with at least one successful orbit determination, for which custody could be maintained is plotted as a function of number of total satellites. As can be seen using additional groups of satellites increases this percentage, this is caused by the fact that each single space debris object is observed more regularly when more satellites are used. However, after around 15 total satellites the percentage does not increase significantly anymore. When comparing the results between a one week versus one month total simulation time, it can be seen that using a longer simulation time leads to the same trend but a higher percentage. This higher percentage is most likely caused by certain space debris objects being observed for the first time in the later stages of the week, which does not allow for a second observations and thus can not be tested for the maintenance of custody.

These percentages are most likely lower than the actual percentages. Since, if an active search is done, the time interval between the first and second measurement will be shorter than it is at the moment, since now a passive search method is used which relies on the space debris crossing the FOV of the sensors again.

For most of the space-debris objects, the reason for the system not being able to maintain custody is that no second orbit determination has taken place. This can be seen in Figure 8.13, only for a small percentage, around 10% of space debris objects, for which a second orbit determination has been done, does not fall in the maintain custody limit. So especially when using a small number of total satellites, the low percentage is caused by the fact that no second orbit determination could be performed and not by the inaccuracy of the orbit determination. It can also be noted from the figure that the along-track error is a lot larger than the cross-track error. The errors for orbit determination for the along- and cross-track were similar, as could be seen in Figure 8.9, however, depending on the accelerations acting on the object the propagation error can vary for the different RSW directions even if the initial error is similar (Mooij and Dirkx, 2021).

Conclusions

The average position error for the optimal design is equal to 198 meters, the radial error is significantly larger than the cross- and along-track errors. This error is good enough to allow the system to maintain custody for approximately 90% of all space debris objects for which at least two different observation sets could be performed. For the 10% of objects for which this was not the case, it was caused by the

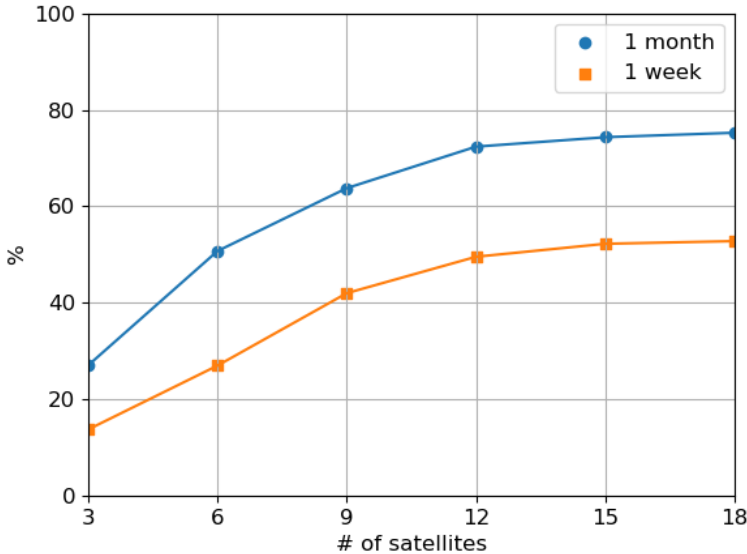


Figure 8.12: Percentage of observed objects for which custody could be maintained as a function of number of satellites and total simulation time

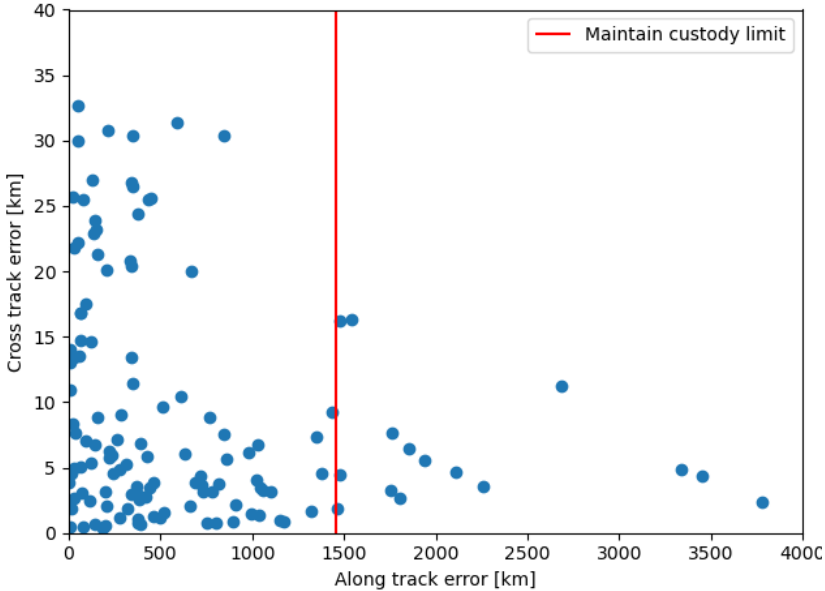


Figure 8.13: Along- and cross-track errors for space debris objects at the time of the second orbit determination

along-track error which was around 10 times larger than the cross-track error. It was also found that the accuracy of the orbit determinations did not depend on the orbit of the space debris objects.

The number of successful orbit determinations for the optimal design is 34, which is only 17% of all space debris objects. This low percentage is mainly caused by the systems poor performance for space debris objects with a high inclination and smaller objects, for objects smaller than 2 cm, no observations can be made. The semi-major axis and eccentricity of the orbits of the space debris objects only have a small effect on the performance of the system. However, this is partly due to the limited GEO region that has been investigated, if broader bounds would have been used the semi-major axis of the space debris objects would have a far greater effect on the number of successful orbit determinations.

The low number of successful orbit determinations is also the reason why the system is only able to maintain custody for around 25% of all objects for which at least one observations could be made. It was also found that the initial state of the satellites have a significant effect on the number of successful orbit determinations that could be performed. However, this effect would have been smaller if a longer simulation time is used.

Increasing the total number of satellites in the constellation will lead to more successful orbit determinations. However, the increase in the number of orbit determinations decreases as more total satellites get used. The same holds for the systems ability to maintain custody of the observed space debris objects, where there is a significant increases for the first couple of added satellites, but after around 15 satellites, the percentage does not increase significantly anymore.

To conclude, the design is able to provide valuable information for space-situational awareness purposes, as long as the system is able to regularly observe the space debris objects. However, due to its poor performance for objects with a high inclination and small size, and the fact that most of the space debris objects in GEO will have a high inclination and small size, the lack of successful orbit determinations severely limits the usefulness of this and similar systems. The performance of the system can be significantly improved by increasing the number of total satellites, however, this will also increase the mission cost. Another way in which this system could prove useful, is by observing and providing orbit determination for relatively new space debris objects. These new space debris objects have an inclination close to zero and gradually move to higher inclinations. The system will thus provide very good performance for these newer space-debris objects.

8.4. Sensitivity

For the simulations done in the previous sections certain values for the two different errors, satellite position and measurement, were used. However, these values could change. Additionally, both the initial state and size of the space debris objects are randomly generated using a certain seed, changing this seed could thus have an effect on the design and performance. In this section the effect of changes of the magnitude of these errors and the different seeds will be investigated. Two different sensitivity analysis will be performed, first the effect of the different errors and seeds values on the design will be looked at. This will investigate how the optimal design changes when different error values and seeds are used. Secondly, the sensitivity of the performance of the optimal design will be investigated.

The lower and upper bounds for the errors were determined by looking at literature. For the position error a nominal value of 1 m is used, it has been shown that for satellites in MEO the position can be known as accurately as 0.5 m (Ansalone and Curti, 2013) (Van den Ijssel et al., 2003) (Guo et al., 2010)(Deng et al., 2014), so this value will be used as the minimal value for the position error. To make a fair comparison between the lowest and highest possible position error, a similar increase in the position error is used as the upper bound, so a maximum position error of 2 meters will be used. For the measurement error a nominal error of 3 arc seconds has been used, however, this error can range between 1 and 5 arc seconds according to literature (Felicetti and Emami, 2016) (Ansalone and Curti, 2013) (Armellin et al., 2016), so these will be used as the minimum and maximum values for the measurement error. The nominal seed that has been used is 1, the other two seeds to be tested have been randomly chosen to be 242 and 2345.

8.4.1. Design sensitivity

To determine how the different error values and seeds effect the optimisation process, the factorial design process has been repeated for all different seeds and error values. For the first run, the same bounds and intervals were used as for the nominal case, see Table 8.3, then, using the same method,

the new bounds and intervals were determined for each individual case and a new simulation was run. Using those results, the average value of each design variable of the 20 closest points to the chosen optimal point were then compared to each other and to the nominal case. This method was chosen instead of comparing the chosen optimal designs to each other, because this method eliminates a larger part of the randomness of choosing the optimal solution and thus provides a better comparison.

In Table 8.8, the results for the different errors and seeds are shown. First looking at the effect of the satellite position error on the design, it can be seen that a larger position error increases the number of satellites per group, semi-major axis and the inclination difference compared to the nominal case, the focal length decreases slightly. These results make sense, since a larger position error will decrease the accuracy of the orbit determination, to account for this the number of satellites per group, semi-major axis and inclination difference increases, which have been shown in previous sections to increase the orbit determination accuracy. The decrease in focal length is not directly related to the a difference in error, however, it changes, because the semi-major axis has changed. Since the semi-major axis increased, the focal length can be decreased slightly, which allows for a larger FOV and thus more observations. As expected, the exact opposite happens when decreasing the position error, which sees a decrease in the number of satellites per group, semi-major axis and inclination difference and a slight increase in focal length. The deviations from the nominal case are similar for both the increased and decreased position error.

The effects of varying the measurement errors are similar to those of the satellite position error. A larger measurement error leads to more satellites, a larger semi-major axis and a larger inclination difference, and vice versa for a smaller measurement error. However, it can be noted that the measurement error has a larger effect on the optimisation process compared to the position error. This makes sense since the measurement error caused by a satellite position error of 2 meters is smaller than the maximum measurement error of 5 arcseconds. The satellite position error thus has less influence on the optimisation process.

Using a different seed and thus different initial states and sizes of the space debris, has only a slight influence of the optimisation process. There are some differences between the average nominal design and the average design for the different seeds. As could be seen in the previous section the initial state of the satellites and the space debris objects have a significant effect on the performance of the system, especially for the number of successful orbit determination, which influences the optimisation process. Additionally, the different seeds were also used for a optimisation run using a minimum measurement error. It can be seen that the difference in seeds has a similar effect on the nominal case as on the case with a minimum measurement error.

In Figure 8.14 the Pareto fronts for the nominal, minimum and maximum values of the different

Table 8.8: Average value of the design variables of the 20 closest points to the chosen optimal point for the different values of errors and seeds

	Number of satellites per group [-]	Semi-major axis [km]	Inclination difference [deg]	Focal length [m]
Nominal	3.6	29,100	9.6	0.40
Max. Position error	3.8	29,700	9.9	0.38
Min. Position error	3.5	28,400	9.2	0.47
Max. Measurement error	3.8	31,100	10.7	0.38
Min. Measurement error	3.4	26,400	8.5	0.53
Seed 242	3.5	29,200	9.8	0.40
Seed 2345	3.6	28,800	9.7	0.42
Min. Measurement error, seed 242	3.4	26,700	8.6	0.51
Min. Measurement error, seed 2345	3.5	26,200	8.5	0.54

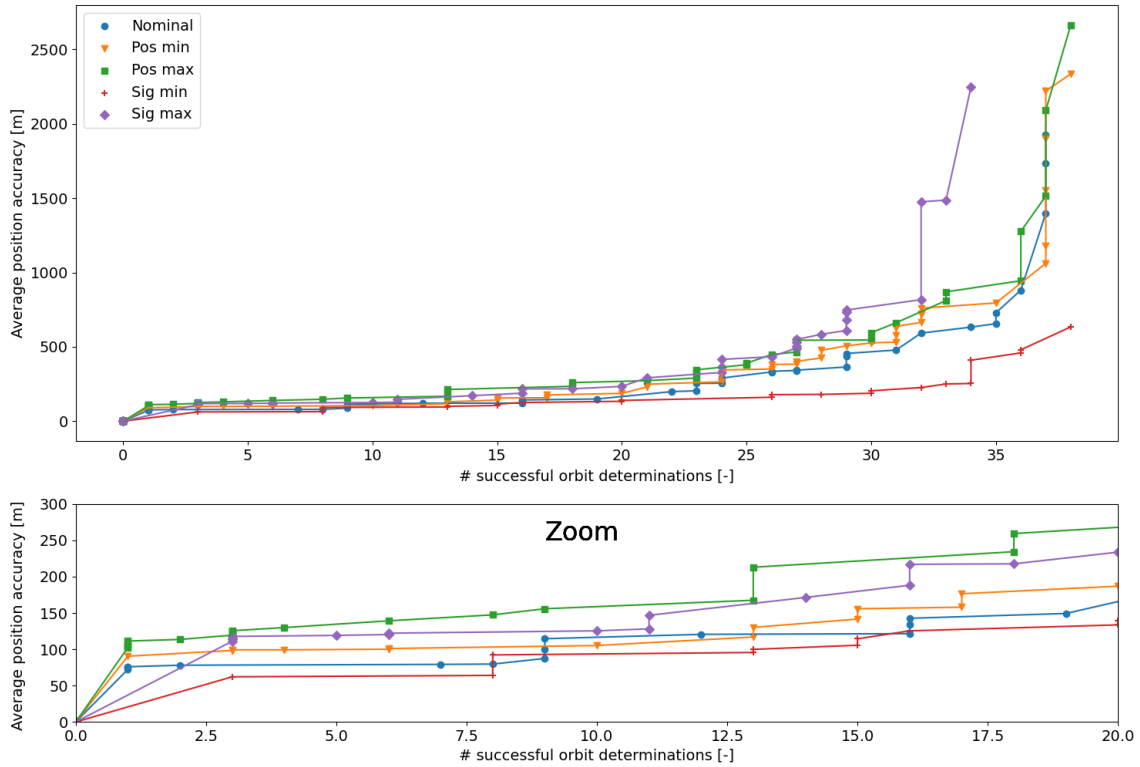


Figure 8.14: Pareto fronts for different error values

errors are shown. In the figure the Pareto fronts for the different seeds have not been shown, since these were very similar to the nominal case and made the graph difficult to read. As already seen from Table 8.8, the effect of changing the measurement error is significantly larger than the effect of changing the position error. This is especially true for the right hand side of the graph, which corresponds to a higher number of successful orbit determinations.

Looking more closely to the Pareto fronts for the minimum and maximum measurement error, it can be seen that for the lower number of successful orbit determinations the Pareto fronts do not differ to much from the nominal case. However, as the number of successful orbit determinations increases, the difference in the accuracy of the orbit determinations starts to grow bigger between the minimum and maximum measurement error. This makes sense, as the lower number of successful orbit determination use a large semi-major axis as could be seen in Figure 8.7, for these cases the measurement error has relatively less effect on the orbit determination accuracy since the distance between the observer and the space debris object is smaller. The effect of increasing or decreasing the measurement error increases as this distance becomes larger. A smaller measurement error both leads to more successful orbit determinations and a higher accuracy.

A changing position error has less effect on the Pareto fronts. The difference in the Pareto fronts for the maximum and minimum position error remains roughly the same for the whole front. Except for the at highest number of successful where the Pareto fronts are very similar. Again this makes sense, as these points correspond to a lower semi-major axis, a small position error has less influence on the measurement the further the distance between the observer and the space debris object gets.

8.4.2. Performance sensitivity

To test the sensitivity of the performance of the chosen optimal design to differing values of the errors, all combinations of error values were simulated and the average accuracy and number of successful orbit determinations was then compared to the nominal performance. For the performance sensitivity analysis the position error was split up into three distinct errors in the RSW-frame, this was done in order to determine if position errors in different directions in the RSW-frame have a different effect on the performance. The error values can be found in Table 8.9.

Table 8.9: Measurement and position error values

Measurement error	[1, 2, 3, 4, 5]	[arcsec]
RSW-position error	[0.5, 1.0, 1.5, 2.0]	[m]

In Table 8.10, the percentage difference in accuracy of the orbit determination for the different measurement and position errors are shown compared to the nominal case. As already seen in the design sensitivity analysis, the measurement error has a significantly larger effect on the accuracy of the orbit determinations compared to the position error. The average accuracy can change as much as 50% when the measurement error differs from the nominal value. It can also be noted that, for both the measurement and position errors, a larger error has a larger negative effect than a comparable smaller error has a positive effect. For example, if the along-track position error decreased by 100% the accuracy improvement is around 18%, but when the error increases by 100% the accuracy decreases by as much as 35%. Additionally, the effects of the radial and cross-track position errors are very similar, however, the along-track position error has a larger effect on the average orbit determination accuracy. This difference in effects is also explained by the fact that a difference in along-track position has a larger effect on the measurement error than the other two directions.

Due to the relatively high sensitivity of the accuracy to the varying error values, it was also investigated how this would effect the systems ability to maintain custody of the regularly observed space debris objects. In Figure 8.15 this percentage is plotted as a function of a decreasing orbit estimation accuracy. If the errors stays between the bounds specified earlier, the percentage only drops by about 10% and the system is still able to provide a good performance. However, if the error in the orbit estimation of the observing satellites becomes very large, the percentage of objects for which custody can be maintained drops rapidly.

In Table 8.11, the percentage difference in number of successful orbit determinations for the different measurement and position errors are shown compared to the nominal case. The same relation between the errors and the performance holds as for the accuracy, the measurement error has the largest effect, followed by the along-track position error and the radial and cross-track error have a similar effect on the performance. The negative effect of increasing the error is again larger than the positive effect of decreasing the errors. The number of successful orbit determinations is not very sensitive to the changing error values, especially compared to the sensitivity of the accuracy. The maximum change is around 5%. The errors did have a noticeable effect on the number of successful orbit determinations in the design sensitivity analysis, however, this is because the lower measurement error allowed for a smaller semi-major axis and thus an increased amount of observations. When using the same constellation design, decreasing the errors does not have a large influence on the amount of observation the system can do. The only way the errors influence the number of successful orbit determinations is by either increasing or decreasing the accuracy of the orbit determinations which increases or decreases the number of orbit determinations that converge, thus making them successful or unsuccessful.

Conclusions

The design is sensitive to the different error values. There are significant differences between the optimal design for the nominal values and the designs, which used different error values. If the errors increase the semi-major axis, number of satellites per group and inclination difference all increase, to negate the errors affect on the orbit determination accuracies. The design process is more sensitive to the measurement error compared to the position error. Additionally, the changes of the design due to an increase in error are larger than the changes due to a decrease in error. Furthermore, the initial

Table 8.10: Percentage change in the orbit estimation accuracy for different error values

Measurement error [arcsec] / position error [m]	1/0.5	2/1.0	3/1.5	4/2.0	5/-
Measurement error	+37.2	+14.6	+2.10	-28.2	-48.7
Radial pos. error	+11.6	-1.38	-16.0	-27.2	-
Along-track pos. error	+18.2	+1.21	-24.1	-35.6	-
Cross-track pos. error	+11.9	-1.92	-14.8	-28.1	-

Table 8.11: Percentage change in the number of successful orbit determination for different error values

Measurement error [arcsec] / position error [m]	1/0.5	2/1.0	3/1.5	4/2.0	5/-
Measurement error	+4.1	+1.2	+0.5	-1.5	-5.1
Radial pos. error	+2.1	-0.2	-1.0	-3.8	-
Along-track pos. error	+3.6	+0.6	-2.1	-4.8	-
Cross-track pos. error	+1.9	+0.1	-0.8	-3.4	-

states of the space debris objects only have a small effect on both the design and performance.

The average position accuracy of the optimal design is also sensitive to the different error values. An increase of the error values can decrease the accuracy by as much as 50%. The measurement error has a larger effect on the average position accuracy compared to the position errors. Additionally, the along-track position error has more effect on the accuracy than the radial and cross-track position error. It was also found that if the error becomes too large the system will not be able to maintain custody for a large part of the space debris objects. The number of successful orbit determinations is not very sensitive to the different error values, changes in the number of successful orbit determinations are also not caused directly by varying error values but due to differences in accuracy of the orbit determinations.

To conclude, both the design process as well as the performance of the optimal design are sensitive to varying values for the errors. Determining the predicted error values accurately before the design process starts is thus very important for finding the optimal design. If the actual values for the error differ from the predicted values, the real-life performance can change significantly. The error values are also not constant, especially the position errors, so the accuracy of the orbit determinations can also vary during its operation. Additionally, the measurement error has the largest effect on both the design process and performance, so if the performance of the system needs to be enhanced the best way to do it would be to decrease the measurement error as much as possible.

8.5. Robustness

In this section the design will be tested for its ability to be used for different mission objectives, i.e., its robustness. It will be investigated how the design performs for space debris objects that do not orbit in the GEO regime, two different regimes will be looked at, space debris objects close to GPS-satellites

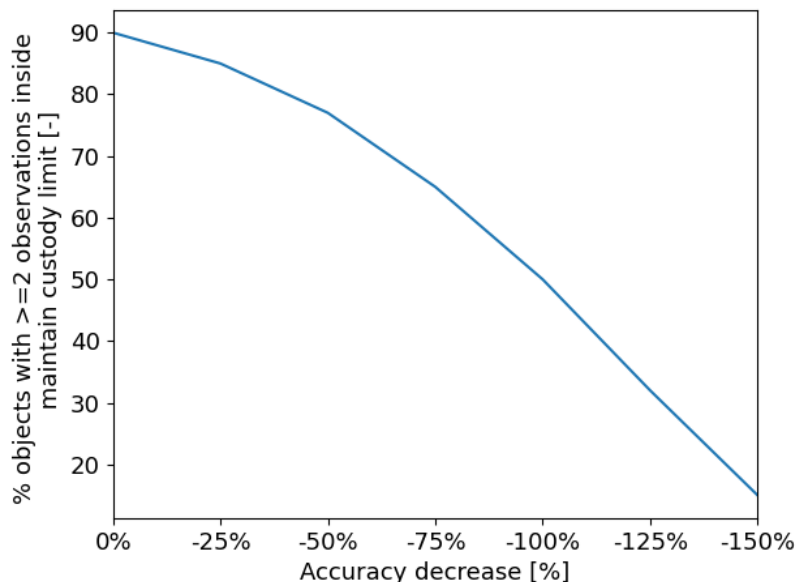


Figure 8.15: Percentage of objects with at least 2 observations which fall inside the maintain custody limit as a function of the average position accuracy

and objects in a geostationary transfer orbit.

8.5.1. Space debris near GPS-satellites

The GPS satellites are arguably the most important satellites for the day-to-day operations on Earth. Therefore, the robustness of the design will be tested by looking at the performance of the design for space debris objects orbiting close to the GPS satellites. The orbital parameters for the GPS-satellites can be seen in Table 8.12.

In earlier parts of the report it was already found that the optimal design does not perform well for space debris objects with high inclinations, so it is expected that the design will not work well for this particular scenario. To test the robustness, 500 space debris objects will be simulated with orbital parameters similar to those of the satellites. The optimal design does need to be changed, since at the moment the satellites will have a larger semi-major axis than the objects, which will make it impossible for the satellites to observe the object. To adjust the design for the GPS region, a quick optimisation for the semi-major axis and the focal length was done, while keeping the inclination difference and number of satellites the same as these should not be influenced by the changing of semi-major axis of the space debris objects. A factorial optimisation was done using the values in Table 8.13, which were based on the ratios between the semi-major axis of the space debris objects and the semi-major axis of the optimal design.

The best performing design has a semi-major axis of 19,000 km and a focal length of 0.2 meters. This has almost the exact same ratio between the semi-major axis of the space debris objects and the semi-major axis of the optima design ($19,000/26,560 = 0.72$, $31,000/42,500 = 0.73$). The best performing design in this case is very relative, since even this design only managed to provide a successful orbit determination of just two space debris objects, a percentage of 0.4%. This was expected since, as could already be seen in Figure 8.11, there is a negative relation between the number of observations of a space debris object and the inclination of that object, even for a inclination of 15 degrees only for 20% of the objects a successful orbit determination could be performed. The accuracy of the orbit determinations was also 200% higher than for the optimal design for the GEO case. This was caused by the very low observation time, which was equal to the lowest possible observation time of 240 seconds. This design is thus clearly not suitable for this mission objective and more broadly, the design is not suitable for any mission where highly inclined objects need to be observed.

8.5.2. Geostationary transfer orbit

GEO based space debris objects are not the only space debris objects that could be observed by the satellites. Space debris objects that have a geostationary transfer orbit (GTO) can also be observed. A GTO is a highly elliptical orbit which is used to transfer from a LEO to a GEO, see Figure 8.16. A GTO for a satellite usually has the same inclination as the initial LEO, a manoeuvre is performed to lower the inclination to 0 degrees at the apogee. Space debris objects in a GTO only spend a small portion of their orbit in the observable region of the satellites, it is thus expected that the number of successful orbit determinations will decrease significantly compared to the nominal case. To test whether the optimal design is able to make accurate orbit determinations for space debris objects in a GTO, 200 objects are simulated using the semi-major axis, inclination and eccentricity seen in Table 8.14, and with a varying argument of periapsis, true anomaly and right ascension of the ascending node.

The performance of the constellation design for the orbit determination of space debris objects in GTO is far worse, especially for the number of successful orbit determination, then for objects in GEO.

Table 8.12: Kepler elements of space-debris objects near GPS-satellites

Semi-major axis	26,560	[km]
Eccentricity	0.0 - 0.02	[-]
Inclination	54.0 - 56.0	[deg]

Table 8.13: Adjusted design variables ranges for near space-debris near GPS-satellites

Semi-major axis	[15,000, 17,000, 19,000, 21,000, 23,000]	[km]
Focal length	[0.10, 0.15, 0.20, 0.25, 0.30]	[m]

Table 8.14: Orbit parameters for space-debris objects in a GTO

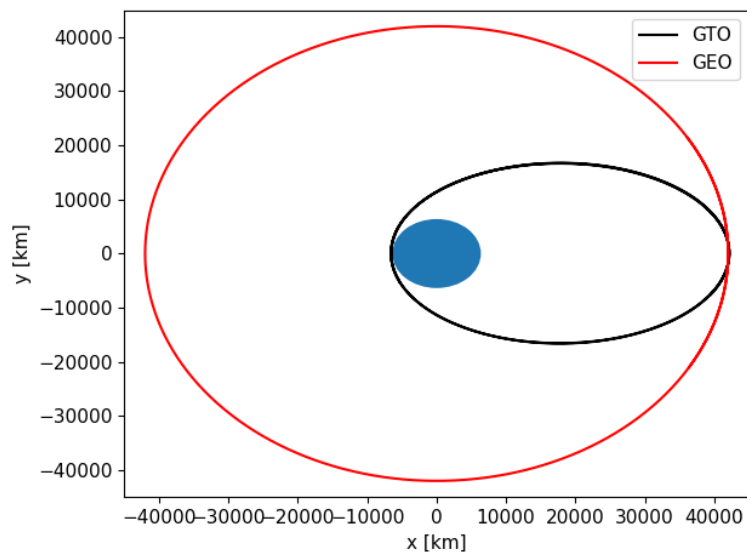
Semi-major axis	24,371	[km]
Eccentricity	0.73	[-]
Inclination	0 - 15	[deg]

The constellation was only able to observe 3% of all space debris objects compared to 17% for the nominal case. This makes sense since the space debris objects spend only a short time in a possibly observable region for each orbit. Similarly to the nominal case, the constellation also performed way better for space debris objects with a inclination close to zero. However, when a satellite reaches apogee, a combined manoeuvre is used to change the perigee and inclination, so if a space debris object has a inclination of 0 degrees it is most likely already in GEO, so 0 degree inclination GTO's are not likely to be found. The accuracy of the orbit determinations is also significantly lower than for the GEO based space debris objects, the average position accuracy is 450 meters compared to the 198 meters for the nominal case. This could be caused by the lower average observation time and the fact that the objects are in a highly elliptical orbit instead of a near-circular orbit.

The design is thus not very capably of providing an orbit determination for a lot of space debris objects in GTO, as the number of successful orbit determinations is very small. However, the design is able to provide a reasonably accuracy orbit determination if a space debris object in GTO happens to be spotted during its nominal operations.

Conclusions

For both scenarios, differing from the nominal case, the (adapted) constellation did not perform well. There was a significant drop in the number of successful orbit determinations both caused by the same reason, the space debris objects spend too little time in the observable GEO. This decreases the chances that the space debris object can be observed. Due to the limited observation time the accuracy of the orbit determinations is also significantly lower than for the nominal case. The optimal constellation design is thus not robust and a serious redesign would be necessary to provide adequate performance for these observation scenarios.

**Figure 8.16:** Geostationary transfer orbit

9

Conclusions & Recommendations

In Section 9.1 of this chapter, the conclusions of this research will be discussed and in Section 9.2 the recommendations will be presented.

9.1. Conclusions

The main goal of this research was to answer the following research question:

To what extent can a constellation of satellites with optical sensors increase the surveillance of 1 to 10 cm sized space debris in GEO?

To answer this question a simulator was created which simulated optical observations of space debris objects made by satellites and used these observations to determine the orbit of those objects. Using this simulator a constellation design was optimised using five different design variables, the semi-major axis, the number of satellites per group, the total number of satellites in the constellation, the focal length and finally the inclination difference between satellites in a group. These design variables were optimised for two different performance metrics, the accuracy of the orbit determination and the number of successful orbit determinations, while also taking into account the mission cost. The performance of the resulting optimal design was evaluated to answer the main research question. To help answer this main research question, first the sub-research questions will be answered:

1.1 *How does the accuracy of the orbit determination compare, when only one satellite observes a satellite versus when multiple satellites observe the same object?*

When only one satellite was able to observe a space debris object both the initial orbit determination method as well as the UKF did not converge and resulted in very high errors. Using only one satellite for the orbit determination of space debris objects in GEO is thus not feasible. However, a single satellite could be used for just the observation of objects in GEO. For two or more satellites, the initial orbit determination method and the UKF did converge for most cases. There is a significant increase between the orbit determination accuracies when two satellites observe an object compared to when three satellites observe an object. The same holds for four satellites compared to three, however, the change in accuracy is smaller. It was also found that using more than four satellites did not significantly improve the accuracies of the orbit determinations. Three or more satellites also provide accuracies good enough to maintain custody of 90% of all space debris objects for which two or more separate observations could be made.

1.2 *How does the constellation design change the performance of the system?*

Lowering the semi-major axis of the constellation increases the number of successful orbit determinations, however, it also lowers the accuracy of those orbit determinations. The semi-major axis also has a lower bound which can be used, if the semi-major axis is smaller than this lower bound the number of observations will not be enough for the initial orbit determination method, so no orbit

determinations can be performed. Another constraint for the semi-major axis comes from the fact that for a constellation design with a lower semi-major axis, the focal length and thus the whole satellite will have to increase in size. Compared to the other design variables, the semi-major axis has the largest effect on the overall performance of the system. However, due to its positive effect on the accuracy but its negative effect on the number of successful orbit determinations, the semi-major axis can not be easily changed to increase a certain performance metric without changing the other metric drastically.

Increasing the difference in inclination of the satellites in a group increases the accuracy of the orbit determinations. However, the increase in accuracy due to the increase in inclination difference becomes smaller as the inclination difference gets larger. After around 12 degrees of inclination difference, there is no significant increase in accuracy. Increasing the inclination difference also has a negative effect on the number of successful orbit determination that can be performed by the system. However, the effect of the difference of inclination of the satellites in a group on both the number of successful orbit determinations and the accuracy is minimal compared to the other design variables. The inclination difference can thus mostly be used to further tune a design.

Decreasing the focal length has a positive effect on both the number of successful orbit determinations and the accuracy of those orbit determinations. The focal length has a far larger effect on the number of successful orbit determinations compared to the accuracy. It is nonetheless not possible to choose the smallest possible focal length, as the focal length still needs to be large enough to allow for the observation of most of the space debris objects in the protected GEO region.

As mentioned earlier, the number of satellites per group increases the accuracy up until three to four satellites, after which the increase in accuracy is not significant. The number of satellites per group also decreases the number of successful orbit determinations. However, the number of satellites per group has a far larger positive effect on the accuracy than a negative effect on the number of successful orbit determinations. If needed, the number of satellites per group can thus be changed to increase the average accuracy without negatively influencing the number of orbit determinations too much.

Increasing the total number of satellites in the constellation increases the number of successful orbit determinations, without influencing the accuracy of the orbit determinations. If the number of successful orbit determinations need to be increased, it can be done by increasing the total number of satellites. However, this also increases the mission cost. Additionally, the increase in orbit determinations becomes smaller as the total number of satellites increases. Increasing the total number of satellites also allows the system to maintain custody for a higher percentage of observed space debris objects, however, after 12 total satellites, the increase in this percentage is minimal.

1.3 How does the orbit and size of the space debris objects effect the performance of the system?

The accuracy of the orbit determinations was not significantly effected by the orbits of the space debris objects. The orbits of the space debris objects did influence the number of successful orbit determinations that the system could perform. A larger semi-major axis and eccentricity of the space debris objects lead to a degradation in overall performance of the system. However, for the GEO region, due to its relatively small difference in maximum and minimum semi-major axis and eccentricity, the effect of these orbit parameters was very limited. If this or a similar system would be used for the orbit determination of space debris in a larger region of space, the semi-major axis and eccentricity would have a much larger effect on the overall performance of the system. The number of successful orbit determinations is very dependent on the inclination of the space debris objects. For objects with an inclination close to zero, the performance of the system was very good, however, there was a near linear decrease in the number of successful orbit determination as the inclination of the space debris objects increased.

A larger size of the objects increased the number of successful orbit determinations. For the optimal design, objects smaller than 2 centimeter could not be observed. It is possible to observe these objects using a similar system, either the focal length or semi-major axis would needs to be increased, however, this would significantly degrade to overall performance of the system.

1 To what extent can a constellation of satellites with optical sensors increase the surveillance of 1 to 10 cm sized space debris in GEO?

The average position accuracy of the orbit determinations for the optimal design was 198 meters. This accuracy is high enough for the system to maintain custody and thus provide regular estimated

orbit updates for objects that can be frequently observed. However, it was also found that the accuracy is sensitive to changing position errors. If the error of the estimated orbit of the observing satellites is much larger than the nominal value, the orbit estimation accuracy can degrade enough to where custody can not be maintained for a large number of space debris objects.

The optimal design, see Table 9.1, is able to provide successful orbit determinations for only 17% of all space debris objects, if only one group of three satellites is used. This percentage can be increased significantly by using more satellite groups, but even when using as much as 30 total satellites, the system is still only able to provide orbit determinations for 35% of all space debris objects. This poor performance is mainly caused by objects smaller than 4 centimeter and objects with high inclinations. For objects with an inclination near 0 degrees, the system is able to provide orbit determinations at a rate of around 75%. New space debris objects in the GEO region usually have an inclination close to zero and gradually increase their inclination to around 15 degrees.

To answer the main research question, the system is capable of providing regular accurate orbit estimations and maintaining custody for newer space debris objects with a size larger than 4 centimetres using only a limited number of satellites and perhaps even slightly older objects if the satellite position and measurement errors can be reduced. The system will also be able to sporadically observe and provide an accurate orbit estimation for older space debris objects with a higher inclination. However, the system will not be capable of doing so regularly, even when using a large number of satellites, thus making maintaining custody very difficult for these objects. At this moment, no orbit determination can be done for objects in the GEO region smaller than 10 cm, they cannot even be observed. A system such as this can thus increase the space situational awareness for the GEO region significantly. Space debris objects smaller than 2 cm are still not detectable by this kind of system, unless the semi-major axis is increased significantly, however, this would be very detrimental to the overall performance of the system.

9.2. Recommendations

For the research done in this report a passive search method was used i.e., the relative viewing direction did not change, however, this lead to a relatively low number of objects for which an orbit determination could be performed. This was mainly caused by the fact that the system could not make enough observations to perform a successful orbit determinations for space debris objects with a high inclination. One method that could be used to increase the number of observations of these objects, is an active search method. With an active search method the relative viewing direction changes depending on the situation. This could improve the systems ability to make successful orbit determinations for objects with a high inclination in the following way.

Once an object has been observed, the observing satellites can adjust their viewing direction to follow the space debris object. This will result in more observations for each object, which can increase the number of successful orbit determinations for objects with a high inclination. The extra observations will also increase the overall accuracy of each orbit determination. Additionally, using an active search method will also allow each satellite in a group to observe a different part of the GEO region and only when a object has been observed by one of the satellites, will all satellites in the group focus on the region where the object was spotted. Furthermore, earlier performed orbit determinations can be used to predict where space debris objects will be at a certain time, an active search method can then be used to aim at the predicted position, allowing the system to maintain custody easier. One drawback of an active search method is the added propulsion and power consumption to accommodate the changing of the viewing direction.

During the research it was found that a higher average orbit estimation accuracy would allow the design to use a smaller semi-major axis and this would increase the number of successful orbit estimations. One possible way to increase the orbit determination accuracy is by using a particle filter instead

Table 9.1: Design variables for optimal constellation design

Number of satellites per group	3	[-]
Semi-major axis	31,000	[km]
Focal length	0.37	[m]
Inclination	-11, 0, 11	[deg]

of a unscented Kalman filter. A particle filter was not used for this research due to its high computational cost, however, it is expected that a particle filter would provide higher accuracy orbit estimations compared to the UKF. It could be interesting to analyse both the difference in performance as well as the differences in the optimal designs that results from the use of a particle filter instead of a UKF.

For this research it was assumed that it was known which observations corresponds to which space debris objects. However, in real life this is not known and for each observation set it needs to be determined whether it corresponds to an already observed space debris object, or if it is the first time this objects has been observed. This can be done using different techniques, such as the admissible region method (Tommei et al., 2007). Such a method could be used to determine if a system such as this would be able to provide regular and accurate enough orbit determinations of space debris object to allow for the correlation of different observation sets.

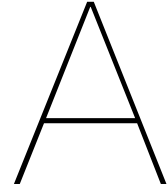
References

- Ansalone, L and F Curti. "A genetic algorithm for initial orbit determination from a too short arc optical observation". In: *Advances in Space Research* 52.3 (2013), pp. 477–489.
- Armellin, R, P Di Lizia, and R Zanetti. "Dealing with uncertainties in angles-only initial orbit determination". In: *Celestial Mechanics and Dynamical Astronomy* 125.4 (2016), pp. 435–450.
- Baskakov, A.I., V.G. Grachyov, V.I. Gusevsky, and A.A. Komarov. "Problem of detecting space debris objects using multi-position radar system". In: *2017 Progress in Electromagnetics Research Symposium-Fall*. IEEE. 2017, pp. 1069–1073.
- Brouwer, D and G.M. Clemence. *Methods of Celestial Mechanics*. Elsevier, 2013.
- Carl, J.R., G.D. Arndt, B.A. Bourgoise, and I Paz. "Space-borne radar detection of orbital debris". In: *Proceedings of GLOBECOM'93. IEEE Global Telecommunications Conference*. IEEE. 1993, pp. 939–943.
- Chen, S. "The space debris problem". In: *Asian Perspective* 35.4 (2011), pp. 537–558.
- Clark, L.G., W.H. Kinard, D.J. Carter, and J.L. Jones. "The long duration exposure facility". In: *NASA SP-473 6861* (1984).
- Cognion, R.L. "Large phase angle observations of GEO satellites". In: *Sensors and Systems for Space Applications VI*. Vol. 8739. SPIE. 2013, pp. 194–205.
- Command, Air Force Space. *GEODSS*. 2019. URL: <https://www.afspc.af.mil/About-Us/Fact-Sheets/Article/249016/ground-based-electro-optical-deep-space-surveillance/>.
- Committee on Space Debris. *Orbital Debris: A technical Assessment*. National academy press, 1995.
- Curtis, H.D. *Orbital mechanics for engineering students*. Butterworth-Heinemann, 2013.
- Czerwinski M.G., Usoff J.M. "Development of the Haystack Ultrawideband Satellite Imaging Radar". In: *Lincoln Laboratory journal* 21.1 (2014), pp. 28–44.
- De Weck, O.L., U Scialom, and A Siddiqi. "Optimal reconfiguration of satellite constellations with the auction algorithm". In: *Acta Astronautica* 62.2-3 (2008), pp. 112–130.
- Deng, Z, M Ge, M Uhlemann, and Q Zhao. "Precise orbit determination of BeiDou satellites at GFZ". In: *Proceedings of IGS*. 2014, pp. 23–27.
- Drolshagen, G, H Svedhem, E Grün, O Grafodatsky, and U Prokopiev. "Microparticles in the geostationary orbit (GORID experiment)". In: *Advances in Space Research* 23.1 (1999), pp. 123–133.
- Du, J, J Chen, B Li, and J Sang. "Tentative design of SBSS constellations for LEO debris catalog maintenance". In: *Acta Astronautica* 155 (2019), pp. 379–388.
- Ebeigbe, D, T Berry, M.M. Norton, A.J. Whalen, D Simon, T Sauer, and S.J. Schiff. "A Generalized Unscented Transformation for Probability Distributions". In: *ArXiv* (2021).
- Endicott, J, A Walker, S Bowring, P Turner, D Allen, O Piersanti, A Short, and D Walton. "Charge-coupled devices for the ESA PLATO M-class Mission". In: *High Energy, Optical, and Infrared Detectors for Astronomy V*. Vol. 8453. SPIE. 2012, pp. 466–472.
- ESA. *ESA space debris office*. 2017. URL: http://www.esa.int/Enabling_Support/Operations/Ground_Systems_Engineering/ESA_Space_Debris_Office.
- *SBSS*. 2017. URL: <https://directory.eoportal.org/web/eoportal/satellite-missions/s/sbss>.
- *GSSAP*. 2019. URL: <https://directory.eoportal.org/web/eoportal/satellite-missions/g/gssap>.
- Fadrique, F.M., A.A. Maté, J.J. Grau, J.F. Sánchez, and L.A. García. "Comparison of angles only initial orbit determination algorithms for space debris cataloguing". In: *Journal of Aerospace Engineering* 4.1 (2012), pp. 39–49.
- Felicetti, L and M.R. Emami. "A multi-spacecraft formation approach to space debris surveillance". In: *Acta Astronautica* 127 (2016), pp. 491–504.
- Fonder, G, M Hughes, M Dickson, M Schoenfeld, and J Gardner. "Space Fence Radar Overview". In: *2019 International Applied Computational Electromagnetics Society Symposium (ACES)*. IEEE. 2019, pp. 56–63.

- Fraunhofer FHR. *Space observation radar TIRA*. 2015. URL: http://www.fhr.fraunhofer.de/en/the_institute/technical-equipment/Space-observation-radar-TIRA.html.
- Gao, F and L Han. "Implementing the Nelder-Mead simplex algorithm with adaptive parameters". In: *Computational Optimization and Applications* 51.1 (2012), pp. 259–277.
- Garcia-Talavera, M.R., J.A. Rodriguez, T Viera, H Moreno-Arce, J.L. Rasilla, F. Gago, L.F. Rodriguez, P Gomez, and E.B. Ramirez. "Design and performance of the ESA Optical Ground Station". In: *Free-Space Laser Communication Technologies XIV*. Vol. 4635. International Society for Optics and Photonics. 2002, pp. 248–261.
- Guo, R, X Hu, B Tang, Y Huang, L Liu, L Cheng, and F He. "Precise orbit determination for geostationary satellites with multiple tracking techniques". In: *Chinese Science Bulletin* 55.8 (2010), pp. 687–692.
- Handley, P.M. and S.P. Hagerty. "Initial Orbit Determination Using Simplex Fusion". In: *2020 IEEE Aerospace Conference*. IEEE. 2020, pp. 46–52.
- Hippelheuser, J. "Inertial orbit estimation using multiple space based observers: A new measurement model". In: *Acta Astronautica* (2021), pp. 717–732.
- Ismail, Z. *Satellite dynamic and control*. 2016. URL: <https://www.slideshare.net/zuliana26/satellite-dynamic-and-control> (visited on 06/03/2021).
- Jiang, P, Y Yang, G Bierner, F.A. Li, R Wang, and A Moghtaderi. "Ranking in Genealogy: Search Results Fusion at Ancestry". In: *Proceedings of the 25th ACM SIGKDD International Conference on Knowledge Discovery & Data Mining*. 2019, pp. 2754–2764.
- Johnson, N.L. "Orbital debris: the growing threat to space operations". In: *33rd Annual Guidance and Control Conference*. 2010.
- Julier, S.J. and J.K. Uhlmann. "Unscented filtering and nonlinear estimation". In: *Proceedings of the IEEE* 92.3 (2004), pp. 401–422.
- Karimi, R.R. and D Mortari. "Initial orbit determination using multiple observations". In: *Celestial Mechanics and Dynamical Astronomy* 109.2 (2011), pp. 167–180.
- Kirchner, G, F Koidl, F Friederich, I Buske, U Völker, and W Riede. "Laser measurements to space debris from Graz SLR station". In: *Advances in Space Research* 51.1 (2013), pp. 21–24.
- Krag, H, M Kahl, J Bendisch, H Klinkrad, and T Schildknecht. "Space based optical observation of small debris objects". In: *ESA 473* (2001), pp. 147–152.
- Krishnamoorthy, A and D Menon. "Matrix inversion using Cholesky decomposition". In: *2013 signal processing: Algorithms, architectures, arrangements, and applications (SPA)*. IEEE. 2013, pp. 70–72.
- Kuitunen, J, G Drolshagen, J.A.M. McDonnell, H Svedhem, M Leese, H Mannermaa, M Kaipainen, and V Sipinen. "DEBIE-first standard in-situ debris monitoring instrument". In: *ESA 473* (2001), pp. 185–190.
- Lambert, J.D. *Numerical methods for ordinary differential systems*. Vol. 146. Wiley New York, 1991.
- Lederer, S.M., E.G. Stansbery, H.M. Cowardin, P Hickson, L.F. Pace, K.J. Abercromby, P.W. Kervin, and R.J. Alliss. *The NASA meter class autonomous telescope: Ascension Island*. Tech. rep. NASA, 2013.
- Lee, B, J Lee, J Yoon, and K Choi. "A new analytical ephemeris solution for the geostationary satellite and its application to Koreasat". In: *Space Technology* 5.17 (1997), pp. 299–309.
- Lejba, P, T Suchodolski, P Michalek, J Bartoszak, S Schillak, and S Zapasnik. "First laser measurements to space debris in Poland". In: *Advances in Space Research* 61.10 (2018), pp. 2609–2616.
- Maskell, P and L Oram. "Sapphire: Canada's answer to space-based surveillance of orbital objects". In: *Advanced Maui Optical and Space Surveillance Conference*. 2008.
- Matsumoto, M and T Nishimura. "Mersenne twister: a 623-dimensionally equidistributed uniform pseudo-random number generator". In: *ACM Transactions on Modeling and Computer Simulation (TOMACS)* 8.1 (1998), pp. 3–30.
- Mooij, E and D Dirx. *Propagation and Optimisation in Astrodynamics*. TU Delft, 2021.
- Mulrooney, M, M.J. Matney, M.D. Hejduk, and E.S. Barker. "An investigation of global albedo values". In: *Proceedings of the Advanced Maui Optical and Space Surveillance Technologies Conference*. Curran Associates, Inc. Redhook, NY. 2008, pp. 16–19.
- Muntoni, G, G Montisci, T Pisanu, P Andronico, and G Valente. "Crowded Space: A Review on Radar Measurements for Space Debris Monitoring and Tracking". In: *Applied Sciences* 11.4 (2021), pp. 1364–1378.

- NASA. *Orbital Debris quarterly news*. 2007. URL: <https://web.archive.org/web/20120215235813/http://orbitaldebris.jsc.nasa.gov/newsletter/pdfs/ODQNv11i2.pdf>.
- Nelder, J.A. and R Mead. "A simplex method for function minimization". In: *The computer journal* 7.4 (1965), pp. 308–313.
- Ott, T, A Benoit, P Van den Braembussche, and W Fichter. "Esa pointing error engineering handbook". In: *8th International ESA Conference on Guidance, Navigation & Control Systems*. 2011, pp. 17–24.
- Pupillo, G, M Bartolini, G Cevolani, M Di Martino, I Falkovich, AA Konovalenko, S Malevinskij, S Montebugnoli, A Nabatov, S Pluchino, et al. "Space debris observational test with the Medicina-Evpatoria bistatic radar." In: *Memorie della Societa Astronomica Italiana Supplementi* 12 (2008), pp. 44–63.
- Reynolds, R.C. and A.E. Potter. *Orbital Debris research at NASA Johnson Space Center*. Tech. rep. Nasa, 1989.
- Roh, K, E Park, and B Choi. "Geostationary orbit surveillance using the unscented kalman filter and the analytical orbit model". In: *Journal of Astronomy and Space Sciences* 28.3 (2011), pp. 193–201.
- Saillant, S. "Bistatic space-debris surveillance radar". In: *2016 IEEE Radar Conference*. IEEE. 2016, pp. 1–4.
- Sato, T, H Kayama, A Furusawa, and I Kimura. "MU radar measurements of orbital debris". In: *Journal of Spacecraft and Rockets* 28.6 (1991), pp. 677–682.
- Schildknecht, T, R Musci, M Ploner, G Beutler, W Flury, J Kuusela, J de Leon Cruz, and L de Fatima Dominguez Palmero. "Optical observations of space debris in GEO and in highly-eccentric orbits". In: *Advances in Space Research* 34.5 (2004), pp. 901–911.
- Schutz, B, B Tapley, and G.H. Born. *Statistical orbit determination*. Elsevier, 2004.
- Seitzer, P, R Smith, J Africano, K Jorgensen, E Stansbery, and D Monet. "MODEST observations of space debris at geosynchronous orbit". In: *Advances in Space Research* 34.5 (2004), pp. 1139–1142.
- Shell, J.R. *Optimizing orbital debris monitoring with optical telescopes*. Tech. rep. Air force space innovation and development center, 2010.
- Silha, J. "Space Debris-Optical Measurements". In: *Reviews in Frontiers of Modern Astrophysics: From Space Debris to Cosmology* (2020), pp. 100–121.
- Slade, M.A., L.A.M. Benner, and A Silva. "Goldstone solar system radar observatory: Earth-based planetary mission support and unique science results". In: *Proceedings of the IEEE* 99.5 (2010), pp. 757–769.
- Stansbery, E and T Settecerci. "A comparison of Haystack and HAX measurements of the orbital debris environment". In: *Second European Conference on Space Debris*. Vol. 393. 1997, pp. 59–67.
- Steindorfer, M.A., G Kirchner, F Koidl, P Wang, B Jilete, and T Flohrer. "Daylight space debris laser ranging". In: *Nature communications* 11.1 (2020), pp. 102–108.
- Taguchi, G. "Quality engineering (Taguchi methods) for the development of electronic circuit technology". In: *IEEE Transactions on Reliability* 44.2 (1995), pp. 225–229.
- Tola, E. "Black-body SNR formulation of astronomical camera systems". In: *IEEE Sensors Journal* 15.9 (2015), pp. 4941–4949.
- Tommei, G, A Milani, and A Rossi. "Orbit determination of space debris: admissible regions". In: *Celestial Mechanics and Dynamical Astronomy* 97.4 (2007), pp. 289–304.
- Vallado, D.A. *Fundamentals of astrodynamics and applications*. Vol. 12. Springer Science & Business Media, 2001.
- Vallado, D.A., B Bastida Virgili, and Tim Flohrer. "Improved SSA through orbit determination of two-line element sets". In: *ESA Space Debris Conference*. 2013.
- Van den Ijssel, J, P.N.A.M. Visser, and E.P. Rodriguez. "CHAMP precise orbit determination using GPS data". In: *Advances in Space Research* 31.8 (2003), pp. 1889–1895.
- Wakker, K.F. *Fundamentals of astrodynamics*. TU Delft, 2015.
- Wan, E.A. and R Van Der Merwe. "The unscented Kalman filter for nonlinear estimation". In: *Proceedings of the IEEE 2000 Adaptive Systems for Signal Processing, Communications, and Control Symposium (Cat. No. 00EX373)*. Ieee. 2000, pp. 153–158.
- Xi, J, D Wen, O.K. Ersoy, H Yi, D Yao, Z Song, and S Xi. "Space debris detection in optical image sequences". In: *Applied optics* 55.28 (2016), pp. 7929–7940.
- Yoon, J, K Lee, B Lee, B Kim, K Choi, Y Chang, Y Chun, and S Ra. "Geostationary orbit determination for time synchronisation using analytical dynamic models". In: *IEEE transactions on aerospace and electronic systems* 40.4 (2004), pp. 1132–1146.

Zhang, Z.P., F.M. Yang, H.F. Zhang, Z.B. Wu, J.P. Chen, P Li, and W.D. Meng. "The use of laser ranging to measure space debris". In: *Research in Astronomy and Astrophysics* 12.2 (2012), pp. 212–218.



Heritage tables

In this Appendix a quick overview of all major systems that have been used for the orbit determination of space debris is given. In Table A.1 the names, operational years, configurations and capabilities of all major systems are listed that make use of an optical telescope to make observations of space debris objects. In Table A.2 the names, configurations and capabilities of the major systems are listed that make use of radar measurements of space debris objects.

Table A.1: Past and present optical OD systems

Name	Operational years	Configuration	Capabilities
Socorro project (Reynolds and Potter, 1989)	1984-1987	78 cm aperture telescope	5 cm @ LEO
GEODSS (Command, 2019)	1985-present	3 telescopes at 3 different sites, 1.02 m aperture, 2° field of view.	20 cm @ GEO
LENZAR (Reynolds and Potter, 1989)	1986-1989	20 cm aperture telescope, 1.9° by 2.1° field of view	35 cm @ 1000 km
NODO (Lederer et al., 2013)	1990-2002	3 m diameter liquid mirror telescope, and a charged coupled device debris telescope	1 cm @ LEO, 10 cm @ MEO
OGS (Garcia-Talavera et al., 2002)	2000-present	1 m aperture telescope	10 cm @ GEO
MODEST (Seitzer et al., 2004)	2002-present	0.9 Schmidt telescope, 1.3° field of view	20 cm @ GEO
Shanghai SLR (Zhang et al., 2012)	2008-present	SLR station, 20 Hz repetition rate, pulse width 10 ns, pulse energy 2J at 532 nm	50 cm @ 900 km
Graz SLR (Lejba et al., 2018)	2011-present	SLR station, 1 kHz repetition rate, pulse width 10 ns, pulse energy 25 mJ at 532 nm	30 cm @ 2500 km
MCAT (Lederer et al., 2013)	2015-present	1.3 m telescope	13.5 cm @ GEO

Table A.2: Past and present radar OD systems

Name	Configuration	Capabilities
AN/FPS-85 (Reynolds and Potter, 1989)	Bi-static phased array, 442 MHz	4 cm @ LEO
AN/FSY-3 (Fonder et al., 2019)	Bi-static phased array	No data yet
TIRA- Effelsberg (Fraunhofer FHR, 2015)	Bi-static 34 m parabolic dish antenna, 1.33 GHz	2 cm @ 1000 km
EISCAT(ESA, 2017a)	3 incoherent scatter radars, antennas 32-42 m, 929 MHz	~3 cm @ LEO
GSSR (Slade et al., 2010)	Bi-static radar, 70 m dish antenna, 8.56 GHz	0.01 cm @ LEO, 0.1 cm @ 2500 km
MU radar(Sato et al., 1991)	Mono-static phase array, 46.5 MHz	2 cm @ 500 km
RT-70(Pupillo et al., 2008)	Bi-static 70 m dish antenna, 5 GHz	~1 cm @ 1000 km
HUSIR(Czerwinski M.G., 2014)	Mono-static 37 m dish antenna, 8-10 GHz	0.003 cm @ 400 km, 5 cm @ 2000 km
HAX (Stansbery and Settecerri, 1997)	Mono-static 12 m dish antenna, 16.7 GHz	1 cm @ LEO

B

Taguchi table

In Table B.1 the Taguchi table that has been used for the optimisation method is shown. These types of tables are used to gather as much information while minimising the amount of experiments that need to be performed. These tables are orthogonal arrays which means that it is a matrix whose columns have the property that in every pair of columns each of the possible ordered pairs of elements appears the same number of times. Each column represents a design variable and each row represents a single experiment. The values in each cell represents the level of the design variable for each experiment. This particular Taguchi table allows for six different design variable, with five levels, to be tested, using 25 experiments.

Table B.1: L25: Taghuci Table

1	1	1	1	1	1
1	2	2	2	2	2
1	3	3	3	3	3
1	4	4	4	4	4
1	5	5	5	5	5
2	1	2	3	4	5
2	2	3	4	5	1
2	3	4	5	1	2
2	4	5	1	2	3
2	5	1	2	3	4
3	1	3	5	2	4
3	2	4	1	3	5
3	3	5	2	4	1
3	4	1	3	5	2
3	5	2	4	1	3
4	1	4	2	5	3
4	2	5	3	1	4
4	3	1	4	2	5
4	4	2	5	3	1
4	5	3	1	4	2
5	1	5	4	3	2
5	2	1	5	4	3
5	3	2	1	5	4
5	4	3	2	1	5
5	5	4	3	2	1